Tests of Birch's law

A thesis submitted for the degree of

Doctor of Philosophy

by

Umesh Chandra Roy

School of Physical Sciences

Jawaharlal Nehru University

New Delhi - 110067, INDIA.

July 2019

Declaration

I hereby declare that the work reported in this thesis is entirely original and has been carried out by me independently in the School of Physical Sciences, Jawaharlal Nehru University, New Delhi under the supervision of Prof. Subir K. Sarkar. I also declare that this work has not formed the basis of award of any Degree, Diploma, Fellowship, Associateship or similar title of any University or Institution.

July 2019

Umesh Chandra Roy

Subir K. Sarkar (Supervisor)
School of Physical Sciences
Jawaharlal Nehru University
New Delhi - 110067, INDIA

(Dean)
School of Physical Sciences
Jawaharlal Nehru University
New Delhi - 110067, INDIA

Publications

---

1. *Large dataset test of Birch's law for sound propagation at high pressure*; Umesh C. Roy and Subir K. Sarkar, Journal of Applied Physics **121**, 225901 (2017).

2. *Birch's law at elevated temperatures*; Umesh C. Roy and Subir K. Sarkar (preprint).

Abstract

The chemical composition of the inner core of the Earth is not understood with clarity – except for the fact that it is largely iron. Strong constraints are placed on the possible answers by the Preliminary Reference Earth Model (PREM) . This spherically symmetric model is constructed by inverting a large amount of data including those on the mass, the moment of inertia, the normal modes of elastic vibration of the Earth and the travel time records of a very large number of seismic events . It provides the values of density, pressure and compressional (P-wave) and shear (S-wave) wave speeds at various distances from the centre of the Earth. In particular it provides the relationship between the two elastic wave speeds and the density in the inner core region. Any proposal regarding the inner core composition must satisfy this constraint. It is presently not possible to reproduce the thermodynamic conditions of the inner core region in a laboratory experiment and hence there is no way of directly checking if the aforementioned elastic wave speed versus density relationship is satisfied by any particular proposal regarding the inner core composition. What is done in practice is to perform the measurements at the relatively low densities presently achievable in the laboratory and then to extrapolate the data to the range of densities in the inner core region predicated by the PREM. The formula used for this extrapolation is known as the Birch's law that postulates that the relationship between the elastic wave speed and the density is linear. However, this law has never been tested precisely since the data on elastic wave speeds from experiments usually have too much scatter around the best linear fit. In this thesis we propose a modified form of the Birch's law by making use of some scaling properties of crystalline vibrational spectra at

high pressure. According to this modified version it is the product of the elastic wave speed and the density raised to the power one-third that should be a linear function of density. We compare the relative accuracies of the original and the modified versions of the Birch's law by designing a suitable metric for this purpose and by making use of some existing data, both experimental and computational, and a large volume of new high precision computational data generated by us via the application of the density functional theory of electronic structure calculation. Our calculations are done for a large number of systems at zero temperature and for a somewhat smaller number of systems at finite temperatures. The conclusion of our analysis is that while the original Birch's law is satisfied fairly well our modified version does consistently better and provides a more accurate description of the speed-density relationship. This should make possible a more reliable extrapolation of the low density elastic wave speed data into the domain of the much higher densities relevant to the inner core region.

Contents

Chapter 1

Introduction

1.1 Introduction

What is the chemical composition of the inner core of the Earth? This issue is far from being resolved despite decades of research in this field [1-3]. Apart from the fact that it is largely iron there is no clear convergence of opinion on what the remaining elements might be or in what form and structure do the various elements coexist. Since direct access is not possible one necessarily has to depend on all the pieces of reasonably precise quantitative information that are available and are relevant to the problem. To this category belongs the Preliminary Reference Earth Model (PREM) [4]. This is a spherically symmetric model of various physical parameters such as density, elastic properties, pressure etc. of the Earth. It has been constructed by inverting a vast amount of information such as the mass, the moment of inertia and the normal modes of the Earth as well as the travel time records of a very large number of seismic events propagating through the Earth. Of particular interest in the present context are the aspects of pressure, density and the speeds of the compressional (P-wave) and shear (S-wave) waves as prescribed by this model. Figures 1.1 through 1.3 provide a summary of this data over the inner core and the molten outer core region of the Earth (in these three figures the vertical dashed lines represent the boundary between the inner core region and the outer core region). Figures 1.1 and 1.2 show the variation of the pressure and the density with radial distance from the centre of the Earth. Figure 1.3 shows the variation of the P-wave and S-wave speeds. The

discontinuity in density and the P-wave speed at the boundary of the inner and outer cores may be noted. S-waves do not propagate through the molten outer core. However, a P-wave incident at an angle upon the boundary between the inner and outer cores will give rise to a S-wave component that travels through the inner core. Thus the speed of S-waves in the inner core is also a physical quantity of interest and is shown in figure 1.3.

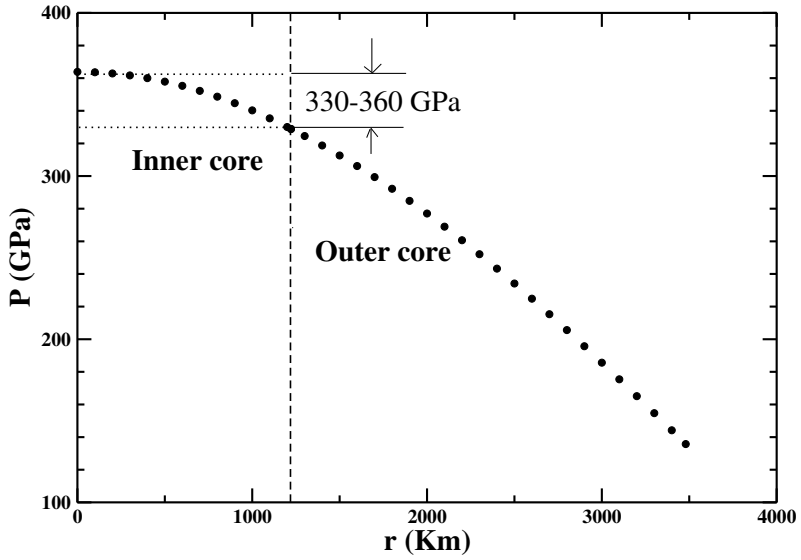

Figure 1.1: Pressure (P) is shown as a function of the distance (r) from the centre of the Earth.

We can combine the information available in the figures 1.2 and 1.3 regarding the density and the P-wave speed in the inner core region. Figure 1.4 summarizes this information by way of plotting the P-wave speed as a function of the density. Although the information regarding the radial distance is lost it retains the key elastic and thermodynamic components and this figure plays a focal role in finding the answers to the central question posed at the very beginning. And the reason is this: *any proposal regarding the structure and chemical composition of the inner core must be such that, under the prevalent thermodynamic conditions, it should lead to this density versus P-wave speed plot.* A similar statement would be true for a plot of the S-wave speed against density using the PREM data.

Please note that the range of pressure in the inner core is from 330 to 360 GPa. The temperature is also extreme and although it is not known with complete

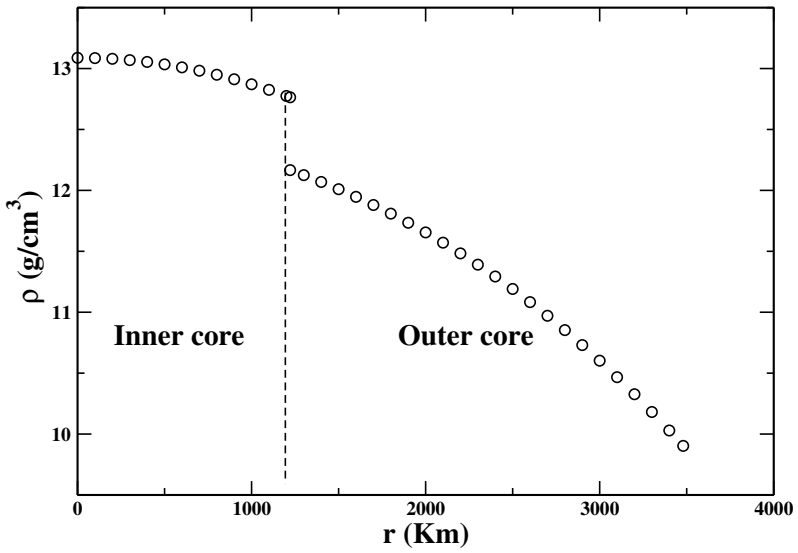

Figure 1.2: Density (ρ) is shown as a function of the distance (r) from the centre of the Earth.

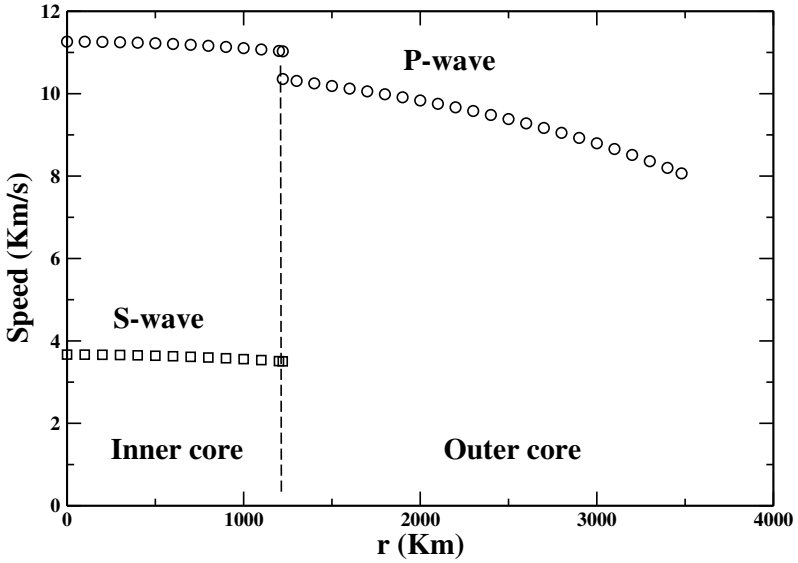

Figure 1.3: P-wave and S-wave speeds are shown as function of the distance (r) from the centre of the Earth.

certainty, a value of 5000K (let's call it T_0) may be taken to be acceptable enough [5-7]. Thus if a proposition is made that the composition is X and the structural state is Y then the following has to be true: For the temperature T_0 if the pressure

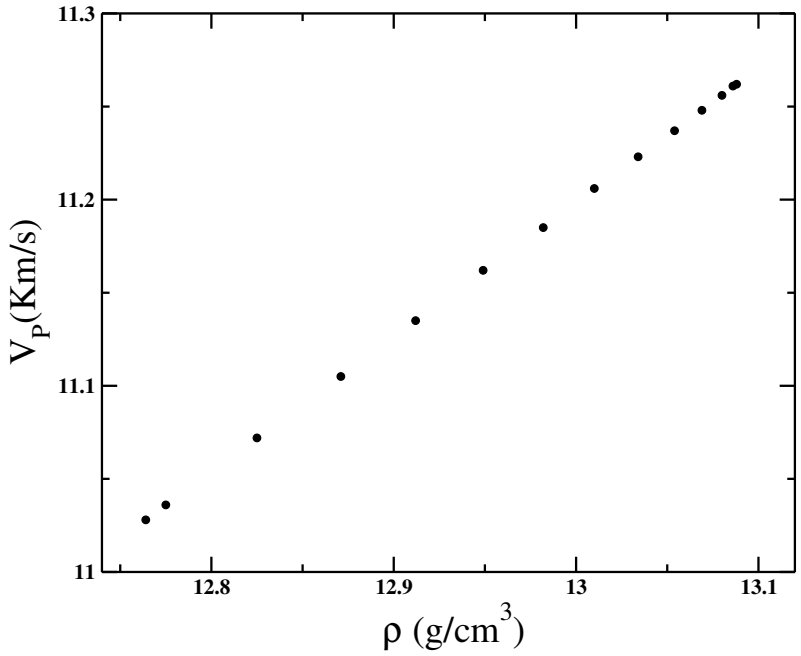

Figure 1.4: P-wave speed (V_P) is shown as a function of density (ρ) in the inner core region.

varies in the range of 330 GPa to 360 GPa then (i) the lowest free energy structural state for the composition X should always be that described by Y and the density should vary in the range prescribed by the PREM and (ii) if the P-wave speed (V_P) is plotted as a function of density (ρ) [both V_P and ρ being functions of the pressure variable] the figure 1.4 should be reproduced. The first part is a question in thermodynamics [8]. Our interest in this thesis is more in the second part i.e. does the P-wave speed have the correct dependence on density? Of course this is in the context of a particular temperature (or a range of temperatures) that is extremely high. It is presently not possible to reproduce the thermodynamic conditions of the inner core in the laboratory. So, given a composition (let's say pure iron or some compound or alloy in which iron is the dominant component) how can one know the P-wave speed at the ultra-high densities appearing in figure 1.4 – when direct experimental data regarding the elastic wave speed is available only for pressures up to about half the inner core pressure (and the densities are also correspondingly low)?

The answer to the question appearing at the end of the previous paragraph

lies in what is known as the Birch's law [9-11]. For our purposes it may be stated as follows: (i) ***Elastic wave speed depends on the thermodynamic conditions only through density*** and (ii) ***the dependence of elastic wave speed on density is linear***. If we assume the validity of the second part of the law it becomes obvious that the speed at high densities can be found, through extrapolation, from a knowledge of its values at lower densities. Note that the essential point is not that the dependence of speed on density is linear but that it is described by a known function. Birch's law is used frequently enough by experimentalists and has been tested extensively (mostly for iron or its compounds or alloys). Empirical evidence suggests that the law is satisfied fairly well [12-31]. However, there is a high level of inherent uncertainty in these extremely difficult experiments and the data always displays a high level of scatter around the best fit straight line when the elastic wave speed is plotted against the density. Thus it is certainly possible that a non-linear function would provide a more accurate description of the relationship between density and speed. Such non-linearity was proposed quite early [32-33] and also has been revived more recently [20]. In fact this is also the central theme of the present thesis: ***performing tests for the conventional form of the Birch's law and striving to construct modifications to the law so that better agreement may be found with observations***.

The need for a modified version of the Birch's law with improved predictive ability can be fully appreciated on the basis of the following example: Suppose the inner core is assumed to be made up of hexagonal-close-packed iron. Then an extrapolation of the speed-density data, obtained at lower densities, to the core densities by using the Birch's law as stated above leads to a mismatch of elastic wave speed with what is prescribed by the PREM. However, this mismatch is only a few percent and the possible presence of one or more of a large variety of lighter compounds of iron (oxides, hydrides, sulfides, alloys with silicon etc.) have been suggested on the basis of this. Obviously it is not possible to discriminate between these various proposals unless (i) the law on the basis of which the extrapolation was made to the core densities itself is sufficiently accurate and (ii) the data on the basis of which the extrapolation is made is also accurate enough. In this thesis we are concerned primarily with the first aspect.

In pursuing our goal as stated above it must be borne in mind that the first part of the Birch's law, as stated above, cannot possibly be strictly correct. While it is true that the elastic wave speed does depend primarily on density it does depend somewhat on the temperature also. This has also been recognized in recent works [2,20,34-35] that take this effect of temperature explicitly into account. While trying to improve on the second part of the Birch's law as stated above (i.e. linear dependence of elastic wave speed on density), our goal would be to construct a version that can be true at all temperatures – without committing ourselves to any particular form of the dependence on temperature. What we do expect intuitively on physical grounds is that the effect of temperature should be weaker at higher densities due to the increasing suppression of lattice vibration at higher pressures.

The main results of this thesis can be summarized as follows: Based on a scaling description of the vibrational spectra of several elemental solids, computed by using the density functional theory of electronic structure calculation, we put forward a proposal for a modification of the standard Birch's law of linear dependence of elastic wave speed on density. The rest of the thesis is dedicated to comparing the performance of this modified version *vis-a-vis* the standard version as far as the accuracy of describing experimental or computational data is concerned. Our primary observation is that while the standard Birch's law is satisfied fairly well the modified version is consistently more accurate – although the extent of improvement is variable. These tests require high precision data for the elastic wave speed as a function of the density and the density should also vary over a wide enough range. Much of it is generated by us for a large number of elemental solids by employing techniques based on the density functional theory (DFT). These DFT-based calculations have been performed both at zero temperature and at elevated temperatures – although, due to its high demand on computational resources, the latter category includes fewer systems.

The organization of the thesis is as follows: In chapter 2 we present a summary of the essential tools of our investigation. These are mostly standard but our calculations at finite temperatures incorporate some procedural elements which are different from their counterparts in the published literature. This chapter includes a brief review of the relevant concepts of the theory of elasticity. The key

element in calculating the elastic wave speeds of various kinds is to calculate the elastic constants *ab initio* for a single crystal. We explain the methodology used by us for these calculations. The way to calculate the elastic constants of a bulk isotropic and homogenous poly-crystalline material from those of a single crystal is explained next. We also describe how the elastic wave speeds of various kinds, in a single crystal as well as in a bulk poly-crystalline sample, are computed. Chapter 3 explains the scaling description of vibrational spectra at high pressures and also how we combine this with the empirical observation of linear dependence of average vibrational frequency on density to construct our proposal for a modified Birch's law which is stated as follows: ***The product of elastic wave speed and density raised to the power one-third should be a linear function of density***. In chapter 4 we use data from the existing literature to compare the performances of the two versions of the Birch's law (i.e. the standard one and our modified version). This comparison is continued in chapter 5 where we use high precision data generated by us for the elastic wave speed as a function of density at zero temperature. Chapter 6 examines data generated by us at elevated temperatures. Both the chapters 5 and 6 make extensive use of the density functional theory to achieve the computational objectives. Chapter 7 summarizes our findings.

Chapter 2

Methodology

2.1 Introduction and preliminaries

In this thesis our primary objective, as far as computational aspects are concerned, will be to calculate the speed of propagation of various types of elastic waves in either a single crystal or a poly-crystalline medium [36-44]. Description of the propagation of elastic waves in a solid involves a continuum model in which there is no direct reference to individual atoms or molecules. They are of course there in the background generating all the material and thermodynamic attributes of the medium around any point. One basic assumption in this description is that the range of inter-molecular forces is very short – of the order of a few times the typical inter-molecular separation. The elementary small volume that we usually speak of in the description of the dynamics of such a medium is understood to be much larger than this range of interaction but much smaller than the length scale of variation of any physical attribute that is described in the continuum model in terms of a field.

For our description we will label a small volume (containing a fixed set of atoms or molecules) in the medium by its position coordinates ($\mathbf{R}$) when no waves are present. In the presence of a wave each such small volume will shift to a time-dependent position $\mathbf{r} = \mathbf{r}(\mathbf{R}, t)$. Thus the instantaneous displacement is given by the vector $\mathbf{u} \equiv \mathbf{r} - \mathbf{R}$. Consider now two infinitesimally separated points labelled by $\mathbf{R}$ and $\mathbf{R} + d\mathbf{R}$. The square of the distance between these two points in the absence of any wave is $d\mathbf{R}.d\mathbf{R}$. When the elastic wave is present this becomes

$d\mathbf{r}.d\mathbf{r}$. It is trivial to show that [Note: Summation over repeated indices is always implied – unless specifically stated otherwise.]

$$d\mathbf{r}.d\mathbf{r} = d\mathbf{R}.d\mathbf{R} + 2\eta_{ij}dR_i dR_j \tag{2.1}$$

where

$$\eta_{ij} \equiv \frac{1}{2}(\frac{\partial u_i}{\partial R_j} + \frac{\partial u_j}{\partial R_i} + \frac{\partial u_k}{\partial R_i}\frac{\partial u_k}{\partial R_j}) \tag{2.2}$$

η_{ij} is a component of a symmetric entity called the Lagrangian strain parameter. For small values of strain η_{ij} reduces to $\epsilon_{ij} \equiv \frac{1}{2}(\frac{\partial u_i}{\partial R_j} + \frac{\partial u_j}{\partial R_i})$. If one considers a small domain around $\mathbf{R}$, with volume $d\Omega$ in the absence of distortion, its volume after distortion ($d\Omega'$) is given by $d\Omega$ multiplied by the Jacobian of the transformation from $\mathbf{R}$ to $\mathbf{r}$. Thus, $d\Omega' = d\Omega\ det[\boldsymbol{\alpha}]$ where $\boldsymbol{\alpha}$ is a matrix whose i-th row and j-th column $= \alpha_{ij} = \frac{\partial r_i}{\partial R_j}$. Thus, the initial density ρ_0 and the density ρ after distortion are related as $\rho_0 = \rho\ det[\boldsymbol{\alpha}]$.

The strain parameter $\boldsymbol{\eta}$ defined above is a natural and convenient measure of distortion in a thermodynamic description. To see this consider a small domain such as mentioned above. This may or may not be crystalline. The distances separating all the pairs of particles after distortion is determined by the corresponding values in the absence of distortion and the value of $\boldsymbol{\eta}$. Now, for a solid at a given temperature, all thermodynamic properties are uniquely determined once the mean relative positions of all the atoms/molecules are known. Thus, the thermodynamic state of the volume element of the solid under consideration is determined by the arrangement of atoms/molecules in the absence of distortion, the value of the Lagrangian strain parameter and the temperature (or energy or entropy etc.). This means, for example, that we can consider the mean energy or the Helmhotz free energy or the entropy per unit mass, at some point inside the solid, to be a function of X, $\boldsymbol{\eta}$ and T – where X stands for the description of the undistorted arrangement of atoms/molecules (also called a 'reference state'). [Note: For a solid at a finite temperature, by position of an atom we mean the average position around which the thermal motion takes place.] A crucial point in this context is the following: In general the strain parameter will have spatial and temporal variation. We will assume that the spatial and temporal variation is always sufficiently slow so that the thermodynamics of any small volume is

determined completely by the local, instantaneous values of the strain parameter and the temperature/energy.

As we have mentioned above, inter-particle forces in a solid are very short-ranged. This permits the existence of the concept of a stress tensor – as can be seen from the following argument: Suppose that the solid has been distorted under the influence of a system of forces and torques. Let the force per unit volume at a point $\mathbf{r}$ be $\mathbf{h}(\mathbf{r})$. Then the i-th component of the total force (call it Q_i) on a domain D is $\int_D h_i(\mathbf{r})d^3\mathbf{r}$. However, since the cause of the force on D lies outside it these forces can only be transmitted via the surface S of D through inter-particle forces. Since the inter-particle forces are short-ranged it must be possible to write Q_i as an integral of a local field over the surface of D. In order for this to be identical to the volume integral mentioned above for an arbitrary domain D, the surface integral has to be of the form $\int_S \mathbf{W}.d\mathbf{S}$ where, using Gauss's theorem, div $\mathbf{W}$ equals h_i. Thus, each of the three components of the force per unit volume is the divergence of a vector field. These three vector fields can be combined into a tensor field $\boldsymbol{T}$, called the physical stress tensor, so that the i-th component of the force per unit volume is given by $\frac{\partial T_{ij}}{\partial x_j}$ [Here, of course, we assumed that there are no body forces (such as gravity) present]. Note that the i-th component of force transmitted through a surface element $d\mathbf{S}$ is $T_{ij}d\mathbf{S}_j$. Thus T_{ij} equals the i-th component of the force per unit area transmitted through a surface whose outward normal is along the positive j-th axis. It can be shown [42] that the stress tensor is symmetric.

2.2 Thermodynamics and dynamics in a pre-stressed medium

Since our primary interest is the computation of elastic wave speed propagating in a pre-stressed medium (which corresponds to our reference state X; the strain is zero, by definition, in the state X) it is essential to understand the factors that control the thermoelastic dynamics of a small mass element in the solid. We consider two distinct circumstances in which this motion takes place: (i) isothermal, meaning that the temperature is always fixed at the same value, and

(ii) adiabatic, meaning that entropy of a small but fixed mass element does not change. Our primary dependent variable in the first case is the free energy per unit mass (F) whereas in the second case it is the energy per unit mass (U). These primary dependent variables are functions of the strain parameter. In fact the basic physical input to the study of how elastic waves propagate is the knowledge of how F (for constant temperature) or U (for constant entropy) depends on strain. The relevant equations are:

(A) Applying Newton's second law to a small mass element we get:

$$\rho \ddot{r}_i = \frac{\partial T_{ij}}{\partial r_j} \tag{2.3}$$

Note: Multiply both sides of this equation by the volume of the mass element at the time t to see that this corresponds to: Force = Mass times acceleration. It has been noted above that the force per unit volume is given by the space derivative of the stress tensor. This appears on the right hand side of the equation above.

(B) By tracking the motion of a small mass element which contains a fixed set of particles, we can relate its density ρ_0 in the reference state to that (ρ) at any arbitrary time. In fact we have already noted this above. The relation is:

$$\rho_0 = \rho \; det[\boldsymbol{\alpha}] \tag{2.4}$$

(C) Finally, we need a way to calculate the stress tensor appearing in equation (2.3) from the instantaneous value of the strain parameter. This is done in two steps. First, it is necessary to find how F or U (for constant temperature or for constant entropy situation, respectively) depends on the strain parameter $\boldsymbol{\eta}$. The second step is to calculate the stress from one of the two following equations:

[Isothermal]

$$T_{ij} = \rho \alpha_{ik} \alpha_{jl} \frac{\partial F}{\partial \eta_{kl}} \tag{2.5}$$

[Adiabatic]

$$T_{ij} = \rho \alpha_{ik} \alpha_{jl} \frac{\partial U}{\partial \eta_{kl}} \tag{2.6}$$

By using the expression for F or U in terms of $\boldsymbol{\eta}$ in the last equation we get the expression for stress in terms of strain. This expression for stress is then used in equation (2.3). In the resulting equation the definition of strain is then used to convert the equation into one containing only the current position coordinate $\mathbf{r}(t)$. Finally, this equation is linearized around the reference state to get the final equation describing the propagation of a small amplitude elastic wave in a pre-stressed medium. Before this equation can be written down it is necessary to specify how F (or U) is expressed as a function of the strain parameter $\boldsymbol{\eta}$. Since we assume that the strain measured with respect to the reference state X is small a straightforward Taylor expansion with respect to the components of the strain parameter, terminating with the second power, is done. This gives [41]:

$$\rho_0 U(X, \boldsymbol{\eta}, S) = \rho_0 U(X, \mathbf{0}, S) + C^S_{ij}\eta_{ij} + \frac{1}{2}C^S_{ijkl}\eta_{ij}\eta_{kl} \tag{2.7}$$

and

$$\rho_0 F(X, \boldsymbol{\eta}, T) = \rho_0 F(X, \mathbf{0}, T) + C^T_{ij}\eta_{ij} + \frac{1}{2}C^T_{ijkl}\eta_{ij}\eta_{kl} \tag{2.8}$$

In equations (2.7) and (2.8) C_{ij}'s and C_{ijkl}'s are the first and second derivatives of $\rho_0 U$ or $\rho_0 F$, evaluated at $\boldsymbol{\eta} = \mathbf{0}$ i.e, for the reference state (or the quiescent state) X. Using these expressions for U or F we can calculate the stress tensor $\mathbf{T}$ after computing the derivatives in equations (2.5) or (2.6). In particular if we calculate the stress at $\boldsymbol{\eta} = \mathbf{0}$, we find that C_{ij}=$T_{ij}(X)$ i.e, the coefficients of the first order terms in equations (2.7) or (2.8) are nothing but the components of the stress tensor for the reference state X itself. So we modify equations (2.7) and (2.8) as

$$\rho_0 U(X, \boldsymbol{\eta}, S) = \rho_0 U(X, \mathbf{0}, S) + T_{ij}(X)\eta_{ij} + \frac{1}{2}C^S_{ijkl}\eta_{ij}\eta_{kl} \tag{2.9}$$

and

$$\rho_0 F(X, \boldsymbol{\eta}, T) = \rho_0 F(X, \mathbf{0}, T) + T_{ij}(X)\eta_{ij} + \frac{1}{2}C^T_{ijkl}\eta_{ij}\eta_{kl} \tag{2.10}$$

When we say that the medium in which the elastic wave is propagating is, in general, pre-stressed we mean that the components of $T_{ij}(X)$ are non-zero in general. C^S_{ijkl} and C^T_{ijkl} are called the adiabatic and isothermal elastic constants, respectively.

2.2.1 Equations for small amplitude elastic waves in a pre-stressed medium

Using equations (2.9) or (2.10) and (2.5) or (2.6) to calculate the stress tensor in a general strained state and using that in equation (2.3) we can get the equation of motion for *small amplitude* elastic waves. The equation is

$$\rho_0 \ddot{r}_i = A_{ijkl} \frac{\partial^2 r_k}{R_j R_l} \tag{2.11}$$

where

$$A_{ijkl} = T_{jl}(X)\delta_{ik} + C_{ijkl} \tag{2.12}$$

For a plane propagating wave with wave vector $\mathbf{k}$ and circular frequency ω,

$$\mathbf{r}(R,t) - \mathbf{R} = \mathbf{a}\sin(\mathbf{k}.\mathbf{R} - \omega t) \tag{2.13}$$

Using this in equation (2.11) and then taking the limit $|\mathbf{k}| \to 0$, we find the following eigenvalue-eigenvector equation for $c(\hat{\mathbf{n}})$, the speed of propagation in the direction $\hat{\mathbf{n}}(= \frac{\mathbf{k}}{|\mathbf{k}|})$:

$$M_{ik}a_k = \rho_0 c^2(\hat{\mathbf{n}})a_i \tag{2.14}$$

Here M_{ik} is the i-th row and k-th column of a real, symmetric matrix and is equal to $A_{ijkl}\hat{n}_j\hat{n}_l$. Here $\hat{n}_1, \hat{n}_2$ and $\hat{n}_3$ are the three components of the unit vector $\hat{\mathbf{n}}$. Solutions of equation (2.14) are direction-independent for isotropic materials. For a crystalline medium the solutions will, in general, be direction-dependent. The three solutions for a given direction are referred to as longitudinal acoustic (LA), transverse acoustic 2 (TA2) and transverse acoustic 1 (TA1) – with decreasing order of speed. It should be remembered that, despite what may be suggested by the nomenclature, the longitudinal wave will have some transverse component of displacement in general. Similarly, in the same sense, the transverse waves are not strictly transverse.

In equation (2.12), the elastic coefficient C_{ijkl} is of the isothermal or adiabatic type. Which one should be used in the context of a particular application depends on whether the process can be adequately described as isothermal or adiabatic. Since we are largely interested in seismic waves we will assume that the frequencies

are not low enough to permit an isothermal process. Hence , in all our calculations of elastic wave speed we will invariably use the adiabatic elastic constants in equation (2.12). However, our calculations for elastic constants will always be, to begin with, of the isothermal type. The scheme for the conversion of one type of elastic constant to the other will be explained later. In passing we may note that the elastic moduli measured in a static experiment in a high pressure cell will be of the isothermal type since there is enough time for thermal equilibration. A Brillouin scattering experiment or a typical elastic wave experiment will, on the other hand, measure the adiabatic elastic constants.

2.2.2 Symmetries of the elastic constants

Equations (2.9) and (2.10) define the elastic constants. It should be noted that $\boldsymbol{\eta}$ is a symmetric object with $\eta_{ij} = \eta_{ji}$. Thus there are only six independent real numbers that characterize the strain parameter. As a result C_{ijkl} can also be defined so that it is symmetric under the exchange of i with j and k with l. These symmetries lead to the introduction of the Voigt notation where pairs of Latin indices are replaced by a single Greek index. This notation is:

Pair	ij	11	22	33	32/23	31/13	21/12
Voigt notation	α	1	2	3	4	5	6

Thus the elastic constants can be denoted as $C_{\alpha\beta}$ and the components of the strain parameter as η_α. Since both α and β in $C_{\alpha\beta}$ can have 6 possible values, it would appear that there are 36 independent elastic constants. However, $C_{\alpha\beta}$ is also symmetric under the exchange of α and β. Thus, there are only 21 independent values at the most. Out these 21 independent elastic constants, many will often vanish due to the requirements of crystalline symmetry. For example, all cubic systems (simple cubic, face-centered-cubic and body-centered-cubic) have only three non-vanishing independent elastic constants (usually taken to be C_{11}, C_{12} and C_{44}). Similarly, for a hexagonal-close-packed system there are only five independent non-vanishing elastic constants (often taken to be $C_{11}, C_{12}, C_{13}, C_{33}$ and

C_{44}). For an isotropic elastic medium (as in the case of a poly-crystalline material with truly randomly oriented grains) there are only two independent elastic constants: the bulk modulus and the shear modulus.

2.2.3 Generalized Birch coefficients

We have already defined the symmetric strain ϵ_{kl} as $\frac{1}{2}(u_{kl}+u_{lk})$ where $u_{lk} \equiv \frac{\partial u_l}{\partial R_k}$. Equivalently, $\epsilon_{kl} = \frac{1}{2}(\alpha_{kl} + \alpha_{lk} - 2\delta_{lk})$. Let us also define $\omega_{kl} \equiv \frac{1}{2}(u_{kl} - u_{lk}) = \frac{1}{2}(\alpha_{kl} - \alpha_{lk})$, which is an anti-symmetric object and measures pure rotation. It is clear that

$$\alpha_{ij} = \frac{1}{2}(\epsilon_{ij} + \epsilon_{ji} + \omega_{ij} - \omega_{ji} + 2\delta_{ij}) \tag{2.15}$$

Thus (the six numbers in) $\boldsymbol{\epsilon}$ and (the three numbers in) $\boldsymbol{\omega}$ can be considered to be independent variables. With this understanding we can define the quantity $B_{ijkl} \equiv \frac{\partial T_{ij}}{\partial \epsilon_{kl}}$. Here the partial derivative means that only one of the nine real numbers in $\boldsymbol{\epsilon}$ and $\boldsymbol{\omega}$ is varying and that number is ϵ_{kl}. The B_{ijkl} is called the generalized Birch coefficient. Depending on whether the process is isothermal or adiabatic it will carry a superscript T or S, respectively. It is possible to show that [41]

$$B^{S/T}_{ijkl} = \frac{1}{2}(T_{ik}\delta_{jl} + T_{il}\delta_{jk} + T_{jk}\delta_{il} + T_{jl}\delta_{ik} - 2T_{ij}\delta_{kl}) + C^{S/T}_{ijkl} \tag{2.16}$$

The concept of generalized Birch coefficient will be used to calculate the two effective elastic constants of a poly-crystalline material from the elastic constants of a single crystal. It may be noted that the generalized Birch coefficient B_{ijkl} is symmetric under exchange of i and j or of k and l. Hence the Voigt notation can be used for the generalized Birch coefficient also. However, unlike for the elastic constants where $C_{\alpha\beta} = C_{\beta\alpha}$, $B_{\alpha\beta} \neq B_{\beta\alpha}$ in general.

Our calculations will be only for cubic and hexagonal-close-packed (hcp) systems. For these systems an elastic constant C_{ijkl} will vanish whenever, in the list $\{i,\ j,\ k,\ l\}$ one symbol (out of the set $\{1,\ 2,\ 3\}$) appears only once. We will now show that B_{ijkl} also vanishes in this situation. To see this, note that the expression for B_{ijkl} in equation (2.16) is a sum of two terms. The first of these two is itself a sum of five terms. Each of these five terms is a product of one Kronecker delta function and one element of the stress tensor. In equilibrium the

stress tensor for cubic and hcp systems will be diagonal. Thus each of the five terms will involve the product of two delta functions. In these two delta functions each of the four indices i, j, k and l appear once. Obviously, if one of these four indices is different from the other three the product of the two delta functions will always be zero. Thus, for the cubic and the hcp systems $B_{\alpha\beta}$ is non-zero only when $C_{\alpha\beta}$ is non-vanishing.

2.2.4 Calculation of isothermal elastic constants at zero temperature and for a given pressure

The basic equation to be used for the calculation of isothermal elastic constants is equation (2.10) where $T_{ij}(X)$ represents the stress in the pre-stressed medium. We will now specialize to the calculation of elastic constants of a single-crystal. And, although much of the procedure is completely general, we will limit our description to the cases of cubic and hcp crystals.

First one needs to know the reference state X. For this one minimizes the sum of the energy (e_0) per unit cell and the pressure (P) times the volume (v_0) of the unit cell with respect to the basis vectors and the positions of the atoms within the unit cell (while satisfying the requirements of symmetry). For example, for an fcc lattice with one atom per unit cell, this means minimizing $(e_0 + Pv_0)$ with respect to the lattice parameter of the fcc primitive unit cell. For the hcp case with two atoms per unit cell, it means extremization with respect to the two lattice parameters a and c and also the relative position vector of the two atoms. This minimization of enthalpy is done with the help of the software package Quantum Espresso (QE) [45]. It may be noted that the tensor representing hydrostatic stress is $T_{ij} = -P\delta_{ij}$. So we already know the coefficients of the term linear in the strain parameter $\boldsymbol{\eta}$ in the equation (2.10).

The next step is to apply various kinds of strain parameter $\boldsymbol{\eta}$ and compute the corresponding values of energy per unit cell (Note: At $T = 0$, the Helmholtz free energy is simply the energy (e_0)). For this we use the software package ElaStic [46] to calculate the distorted unit cell geometry corresponding to a given $\boldsymbol{\eta}$.

Calculating the basis vectors of the lattice for a given strain when the reference state basis vectors are given

Consider two Bravais lattice points with the value of (n_1, n_2, n_3) separated by Δn_1, Δn_2 and Δn_3. Before distortion (i.e. in the reference state X), their locations are separated by

$\Delta\mathbf{R} = \Delta n_1\mathbf{V}_1 + \Delta n_2\mathbf{V}_2 + \Delta n_3\mathbf{V}_3$ (i)

where $\mathbf{V}_1$, $\mathbf{V}_2$ and $\mathbf{V}_3$ are the reference state basis vectors. After distortion they are separated by

$\Delta\mathbf{r} = \Delta n_1\mathbf{v}_1 + \Delta n_2\mathbf{v}_2 + \Delta n_3\mathbf{v}_3$ (ii)

We have to calculate $\mathbf{v}_1$, $\mathbf{v}_2$ and $\mathbf{v}_3$ – given $\mathbf{V}_1$, $\mathbf{V}_2$ and $\mathbf{V}_3$ and the symmetric strain parameter $\eta_{ij} = \frac{1}{2}(u_{ij} + u_{ji} + \sum_k u_{ki}u_{kj})$ where $u_{ij} = \frac{\partial r_i}{\partial R_j} - \delta_{ij} = \alpha_{ij} - \delta_{ij}$.

Now, since $\frac{\partial r_i}{\partial R_j} = \alpha_{ij}$

$\Delta r_i = \sum_j \frac{\partial r_i}{\partial R_j}\Delta R_j = \sum_{j,l} \alpha_{ij}\Delta n_l V_{lj}$ from (i)

and $\Delta r_i = \sum_m \Delta n_m v_{mi}$ from (ii)

Thus $\sum_m \Delta n_m v_{mi} = \sum_{j,l} \alpha_{ij}\Delta n_l V_{lj}$ (iii)

(whenever Δn_1, Δn_2 and Δn_3 are small but otherwise arbitrary integers)

Now suppose $\Delta n_l = \delta_{lk}$ for some $k = 1$, 2 or 3. Then using equation (iii)

$\sum_m \delta_{mk} v_{mi} = v_{ki} = \sum_{l,j} \alpha_{ij}\delta_{lk}V_{lj} = \sum_j \alpha_{ij}V_{kj}$

$\Rightarrow v_{ki} = \sum_j \alpha_{ij}V_{kj}$

Thus if we know $\boldsymbol{\alpha}$ we can calculate the new basis vectors. To calculate $\boldsymbol{\alpha}$ from $\boldsymbol{\eta}$ the following procedure may be used:

$\eta_{ij} = \frac{1}{2}(u_{ij} + u_{ji} + \sum_k u_{ki}u_{kj})$

For a pure strain (no rotation) $u_{ij} = u_{ji}$. Then $\eta_{ij} = u_{ij} + \frac{[\mathbf{U}^2]_{ij}}{2} = [\mathbf{U}]_{ij} + \frac{[\mathbf{U}^2]_{ij}}{2}$.

$\Rightarrow \boldsymbol{\eta} = \mathbf{U} + \frac{\mathbf{U}^2}{2}$.

To solve for $\mathbf{U}$ for a given $\boldsymbol{\eta}$, use $\boldsymbol{\eta}$ as the first guess for $\mathbf{U}$. Then use the following recursive algorithm: $\mathbf{U}^{n+1} = \boldsymbol{\eta} - \frac{[\mathbf{U}^n]^2}{2}$

Since $\boldsymbol{\eta}$ is quite small, as is $\mathbf{U}$, this algorithm will converge quite rapidly and solve for $\mathbf{U}$. Once $\mathbf{U}$ is found the identity matrix has to be added to it to get $\boldsymbol{\alpha}$.

For this distorted unit cell, e_0 is calculated by using the QE package. In the tables 2.1 and 2.2 we describe the three types of distortion $\boldsymbol{\eta}$ used and the expression for energy in each case for the cubic geometry.

Table 2.1: Distortions used for the cubic case

Voigt notation	η_1	η_2	η_3	η_4	η_5	η_6
Lagrangian strain	η_{11}	η_{22}	η_{33}	$2\eta_{23} = 2\eta_{32}$	$2\eta_{13} = 2\eta_{31}$	$2\eta_{12} = 2\eta_{21}$
$\eta^{(1)*}$	η	η	η	0	0	0
$\eta^{(8)*}$	η	η	0	0	0	0
$\eta^{(23)*}$	0	0	0	2η	2η	2η

* Notation for the strain follows that of the ElaStic software package.

Table 2.2: Expression for the change in energy per unit cell divided by the volume of the undistorted cubic unit cell

$\eta^{(1)*}$	$-3P\eta + \frac{3}{2}(C_{11} + 2C_{12})\eta^2$
$\eta^{(8)*}$	$-2P\eta + (C_{11} + C_{12})\eta^2$
$\eta^{(23)*}$	$6C_{44}\eta^2$

* Notation for the strain follows that of the ElaStic software package.

For each of the distortion types we choose a set of N values of η between $-\eta_{max}$ and $+\eta_{max}$. For each such η calculation is done for the energy per unit cell. Finally from the analysis of energy vs. η we extract the values of C_{11}, C_{12} and C_{44}. Examples of the free energy versus amplitude of distortion, for each of the three types of distortion, will be shown in chapter 6.

Table 2.3: Distortions used for the hcp case

Voigt notation	η_1	η_2	η_3	η_4	η_5	η_6
Lagrangian strain	η_{11}	η_{22}	η_{33}	$2\eta_{23} = 2\eta_{32}$	$2\eta_{13} = 2\eta_{31}$	$2\eta_{12} = 2\eta_{21}$
$\eta^{(1)*}$	η	η	η	0	0	0
$\eta^{(3)*}$	0	η	0	0	0	0
$\eta^{(4)*}$	0	0	η	0	0	0
$\eta^{(17)*}$	0	0	η	2η	0	0
$\eta^{(26)*}$	$\frac{\eta}{2}$	$\frac{\eta}{2}$	$-\eta$	0	0	0

* Notation for the strain follows that of the ElaStic software package.

Table 2.4: Expression for the change in energy per unit cell divided by the volume of the undistorted hcp unit cell. Here $T^{xy} = T_{11} = T_{22}$ and $T^z = T_{33}$

$\eta^{(1)*}$	$(2T^{xy} + T^z)\eta + \frac{1}{2}(2C_{11} + 2C_{12} + 4C_{13} + C_{33})\eta^2$
$\eta^{(3)*}$	$T^{xy}\eta + \frac{1}{2}C_{11}\eta^2$
$\eta^{(4)*}$	$T^z\eta + \frac{1}{2}C_{33}\eta^2$
$\eta^{(17)*}$	$T^z\eta + \frac{1}{2}(C_{33} + 4C_{44})\eta^2$
$\eta^{(26)*}$	$(T^{xy} - T^z)\eta + \frac{1}{2}(\frac{C_{11}}{2} + \frac{C_{12}}{2} + C_{33} - 2C_{13})\eta^2$

* Notation for the strain follows that of the ElaStic software package.

Next we describe the five types of distortion for the hcp case in table 2.3. It may be noted that the positions of the atoms are optimized in the distorted cell before calculating the energy. In table 2.4 the expression for the change of energy due to the distortion has been given – taking into account the fact that the stress tensor is diagonal and $T_{11} = T_{22}$ due to the hexagonal symmetry. In the special case of hydrostatic pressure $T_{11} = T_{22} = T_{33} = T^{xy} = T^z \equiv -P$. Again for each distortion type we choose a set of N values of η between $-\eta_{max}$ and $+\eta_{max}$. For

each value of η calculation is done for the energy per unit cell (after optimizing the atomic positions). Finally, from an analysis of the plot of the energy vs. η, we extract the values of the five elastic constants. Examples of the free energy versus amplitude of distortion, for each of the five types of distortion, will be shown in chapter 6.

2.2.5 Calculation of isothermal elastic constants at finite temperature and for a given density

For the calculation of isothermal elastic constants at finite temperature one has to use the defining equation (2.10). Now it is the Helmholtz free energy that has to be calculated for various distortions. Since the temperature is finite now, electronic and phononic excitations will also have to be included while calculating the Helmholtz free energy $F \equiv E - TS$. But first of all the reference state X has to be specified. When the density is fixed the specification of the reference state X can be a non-trivial matter at finite temperatures. For the cubic geometry with one atom per unit cell it poses no problem since there is only one lattice parameter whose value is fixed uniquely by the density – and this is independent of temperature. On the other hand, for a case like hcp-Fe with two atoms per unit cell it is a lot more complicated. If a and c denote the lattice parameters perpendicular to and parallel to the axis of hexagonal symmetry, respectively, then only the product a^2c is fixed by the density. So, in this case we minimize the free energy with respect to a (or c) to get the reference state X which is a hcp-crystal lattice. The calculation of the free energy for given values of a and c is done by using the methods described next.

We will need to calculate the Helmholtz free energy per unit cell for the reference state as well as for crystal lattices obtained by putting in known distortions. In all cases the free energy per unit cell is given by the expression

$$f = e_0 + e_{el}(T) - Ts_{el} + f_{ph} \tag{2.17}$$

where e_0 is the electronic ground state energy per unit cell (when more than one atom is present in the unit cell, the electronic ground state energy is minimized

with respect to the co-ordinates of these atomic positions within the unit cell). e_0 is calculated by using the QE package. $e_{el}(T)$ is the additional electronic energy due to the finite temperature excitations from the ground state and is equal to $\chi(T) - \chi(0)$ where

$$\chi(T) = \int \phi n(\phi) H(\phi, T) d\phi \tag{2.18}$$

Here $n(\phi)$ is the electronic density of states per unit cell at the energy ϕ (obtained by using the QE package). $H(\phi, T)$ is the Fermi occupation function $((\exp(\frac{\phi-\mu}{k_B T})+1)^{-1})$ where the chemical potential μ is obtained numerically by making use of the requirement that $\int n(\phi)H(\phi, T)d\phi$ must be equal to the total number of valence electrons per unit cell (as used in the *ab initio* electronic structure calculation). It is numerically difficult to calculate $\chi(T)$ at very low temperatures. So we calculate χ at temperatures not so low and then graphically extrapolate the values to $T = 0$ to calculate $\chi(0)$.

The electronic entropy s_{el} in equation (2.17) is obtained from the expression

$$s_{el} = -k_B \int n(\phi)[H \ln(H) + (1 - H) \ln(1 - H)]d\phi \tag{2.19}$$

where H is the Fermi occupation factor defined above. The phononic free energy per unit cell is calculated from the formula

$$f_{ph} = k_B T \int g(\omega) \ln[2 \sinh(\frac{h\omega}{4\pi k_B T})]d\omega \tag{2.20}$$

where $g(\omega)$ is the phonon density of states at the circular frequency ω. The normalization of $g(\omega)$ is done such that $\int g(\omega)d\omega$ equals three times the number of atoms per unit cell. The phonon density of states is obtained via the implementation of density functional perturbation theory within the QE package. It is extremely important to understand that the above calculation of Helmholtz free energy is based on the quasi-harmonic approximation which treats the vibrational quantum state as a non-interacting gas of phonons. Temperatures upto which this approximation holds is a matter some of debate. It has been asserted by some [35] that this holds good almost all the way upto melting. While that may or may not be true, it follows from physical intuition that the validity of this approximation should extend to higher and higher temperatures as the applied

pressure (or stress, in general) keeps increasing. The reason is simply that higher applied pressure will suppress atomic vibration to a greater degree and thus reduce the amplitude of atomic vibration – leading to a higher level of validity of the quasi-harmonic approximation. In our calculations we have been conservative and have normally not allowed the temperature to exceed 1500K.

2.2.6 From isothermal to adiabatic elastic constants

In many applications, including the propagation of seismic waves, the process is described more appropriately as adiabatic rather than isothermal. Hence the elastic constants relevant to these applications are the adiabatic ones. The general relationship between these two types of elastic constants is given by the following equation [41]:

$$C^S_{ijkl} = C^T_{ijkl} + \frac{T v_0}{C_v} \tau_{ij} \tau_{kl} \tag{2.21}$$

where $\tau_{ij} = (\frac{\partial T_{ij}}{\partial T})_{\{\boldsymbol{\eta}=\mathbf{0}\}}$ and C_v is the specific heat at constant volume per unit cell (of volume v_0). It may be noted that there is no distinction between the two types of elastic constants at $T = 0$. To calculate a derivative such as $\frac{\partial T_{ij}}{\partial T}$ we calculate the stress tensor T_{ij} at an equally spaced set of temperatures – located symmetrically around the target temperature. The derivative is calculated numerically from a polynomial fit to the data for T_{ij} as function of T.

The specific heat per unit cell C_v is a sum of two terms C_{el} and C_{ph} – which are the contributions of the electronic excitations and the phononic excitations, respectively. The expression for C_{ph} is:

$$C_{ph} = k_B \int (\frac{h\omega}{2\pi k_B T})^2 g(\omega) I(1+I) d\omega \tag{2.22}$$

where I is the phonon occupancy factor given by the expression $(\exp(\frac{h\omega}{2\pi k_B T}) - 1)^{-1}$. The expression for C_{el} is:

$$C_{el} = \int [\frac{1}{k_B T} \frac{d\mu}{dT} + \frac{1}{k_B T^2} (\phi - \mu)] \phi n(\phi) H(1-H) d\phi \tag{2.23}$$

where, as before, H is the Fermi occupancy factor. The derivative $\frac{d\mu}{dT}$, appearing in the expression of C_{el}, is calculated by numerically evaluating its expression $-(\frac{1}{T}) \frac{\int (\phi-\mu) n(\phi) H(1-H) d\phi}{\int n(\phi) H(1-H) d\phi}$.

2.2.7 Useful formulas

Generalized Birch coefficients

For the cubic case : $B_{11} = C_{11} - P;\ B_{12} = C_{12} + P;\ B_{44} = C_{44} - P.$

P is the parameter appearing in the stress tensor $T_{ij} = -P\delta_{ij}$.

For the hcp case : $B_{11} = B_{22} = C_{11} + T^{xy};\ B_{12} = B_{21} = C_{12} - T^{xy};$

$B_{13} = B_{23} = C_{13} - T^{xy};\ B_{31} = B_{32} = C_{13} - T^{z};$

$B_{33} = C_{33} + T^{z};\ B_{44} = B_{55} = C_{44} + \frac{1}{2}(T^{xy} + T^{z});$

$B_{66} = C_{66} + T^{xy}.$

$T^{xy} = T_{11} = T_{22}$ and $T^{z} = T_{33}$; the stress tensor is diagonal.

Relationship between adiabatic and isothermal elastic constants and Birch coefficients

In general $B^S_{ijkl} - B^T_{ijkl} = C^S_{ijkl} - C^T_{ijkl}$

For the cubic case: $B^S_{11} - B^T_{11} = B^S_{12} - B^T_{12} = \frac{Tv_0}{C_v}(\frac{\partial P}{\partial T})^2;\ B^S_{44} - B^T_{44} = 0.$

For the hcp case: $B^S_{11} - B^T_{11} = B^S_{12} - B^T_{12} = \frac{Tv_0}{C_v}(\frac{\partial T^{xy}}{\partial T})^2;$

$B^S_{13} - B^T_{13} = B^S_{31} - B^T_{31} = \frac{Tv_0}{C_v}(\frac{\partial T^{xy}}{\partial T})(\frac{\partial T^{z}}{\partial T});$

$B^S_{33} - B^T_{33} = \frac{Tv_0}{C_v}(\frac{\partial T^{z}}{\partial T})^2;\ B^S_{44} - B^T_{44} = 0.$

Wave propagation matrix M in equation (2.14)

$\hat{n}_1$, $\hat{n}_2$, $\hat{n}_3$ are the three components of the unit vector in the direction of propagation.

For the cubic case : Stress tensor $T_{ij} = -P\delta_{ij}$

$$M_{11} = \hat{n}_1^2(C_{11} - P) + \hat{n}_2^2(C_{44} - P) + \hat{n}_3^2(C_{44} - P)$$

$$M_{12} = M_{21} = \hat{n}_1\hat{n}_2(C_{12} + C_{44})$$

$$M_{13} = M_{31} = \hat{n}_1\hat{n}_3(C_{12} + C_{44})$$

$$M_{22} = \hat{n}_1^2(C_{44} - P) + \hat{n}_2^2(C_{11} - P) + \hat{n}_3^2(C_{44} - P)$$

$$M_{23} = M_{32} = \hat{n}_2\hat{n}_3(C_{12} + C_{44})$$

$$M_{33} = \hat{n}_1^2(C_{44} - P) + \hat{n}_2^2(C_{44} - P) + \hat{n}_3^2(C_{11} - P)$$

For the hcp case: Stress tensor $T_{ij} = \beta_i\delta_{ij}$; $\beta_1 = \beta_2 = T^{xy}$ and $\beta_3 = T^z$

$$M_{11} = \hat{n}_1^2(C_{11} + T^{xy}) + \hat{n}_2^2(C_{66} + T^{xy}) + \hat{n}_3^2(C_{44} + T^z)$$

$$M_{12} = M_{21} = \hat{n}_1\hat{n}_2(C_{12} + C_{66})$$

$$M_{13} = M_{31} = \hat{n}_1\hat{n}_3(C_{13} + C_{44})$$

$$M_{22} = \hat{n}_1^2(C_{66} + T^{xy}) + \hat{n}_2^2(C_{11} + T^{xy}) + \hat{n}_3^2(C_{44} + T^z)$$

$$M_{23} = M_{32} = \hat{n}_2\hat{n}_3(C_{13} + C_{44})$$

$$M_{33} = \hat{n}_1^2(C_{44} + T^{xy}) + \hat{n}_2^2(C_{44} + T^{xy}) + \hat{n}_3^2(C_{33} + T^z)$$

When the stress is hydrostatic, $T_{ij} = -P\delta_{ij}$ i.e., $T^{xy} = T^z = -P$.

2.3 Elastic waves in an isotropic and homogeneous medium

A polycrystalline material with a truly random alignment of the individual grains will be an isotropic and homogeneous elastic medium. It will support two kinds of elastic waves in the bulk: P-waves and S-waves. P-waves (sometimes also called primary wave) are compressional waves with vibration parallel to the direction of propagation of the wave and it moves with the speed given by

$$V_P = \Big(\frac{D + \frac{4}{3}G}{\rho_0}\Big)^{\frac{1}{2}} \tag{2.24}$$

S-waves (sometimes also called secondary wave) are shear waves with vibration perpendicular to direction of propagation of the wave and it moves with the speed given by

$$V_S = \Big(\frac{G}{\rho_0}\Big)^{\frac{1}{2}} \tag{2.25}$$

In equations (2.24) and (2.25), D and G denote the bulk modulus and the shear modulus, respectively, of the isotropic and homogeneous elastic medium.

To derive the equations (2.24) and (2.25) we proceed as follows:
Let us consider the propagation of small amplitude waves. As noted in section (2.1), the strain parameter $\boldsymbol{\eta}$ reduces, for small distortions, to $\boldsymbol{\epsilon}$ where $\epsilon_{ij} = \frac{1}{2}(\frac{\partial u_i}{\partial R_j} + \frac{\partial u_j}{\partial R_i})$. Due to the isotropic nature of the medium, the expression given by the equation (2.10) for free energy now looks like

$$\rho_0 F(X, \boldsymbol{\epsilon}, T) = \rho_0 F(X, \mathbf{0}, T) + T_{ij}(X)\epsilon_{ij} + \frac{1}{2}\lambda(Tr(\boldsymbol{\epsilon}))^2 + \mu\epsilon_{ik}\epsilon_{ik} \tag{2.26}$$

where $Tr(\boldsymbol{\epsilon}) = \epsilon_{ii}$. λ and μ are called the Lamé parameters. Now the stress component

$$\begin{aligned} T_{ij} &= \frac{\partial F}{\partial \epsilon_{ij}} \\ &= T_{ij}(X) + \lambda\delta_{ij}Tr(\boldsymbol{\epsilon}) + 2\mu\epsilon_{ij} \\ &= T_{ij}(X) + \lambda\delta_{ij}\sum_{k=1}^{3}\frac{\partial u_k}{\partial R_k} + \mu(\frac{\partial u_i}{\partial R_j} + \frac{\partial u_j}{\partial R_i}) \end{aligned} \tag{2.27}$$

Applying Newton's second law to a small mass element we get the equation of motion:
$\rho_0 \frac{\partial^2 u_i}{\partial t^2}$ = i-th component of force per unit volume = $\partial_j T_{ij}$. Thus

$$\rho_0 \frac{\partial^2 u_i}{\partial t^2} = \lambda \sum_k \frac{\partial^2 u_k}{\partial R_i \partial R_k} + \mu \sum_j \frac{\partial^2 u_j}{\partial R_j \partial R_i} + \mu \sum_j \frac{\partial^2 u_i}{\partial R_j^2} \tag{2.28}$$

To see what the solutions of this equation are like we consider the propagation of a plane wave in the direction of the positive x-axis (Since the medium is isotropic, the results cannot depend on the direction selected). Here, we assume that the directions 1, 2 and 3 are synonymous with x, y and z, respectively. Because of our choice of the direction of propagation $\frac{\partial}{\partial R_2}$ or $\frac{\partial}{\partial R_3}$ acting on u_i (for any i) or its spatial derivatives vanish identically. Thus we get the following three equations:

$$\rho_0 \ddot{u}_x = (\lambda + 2\mu) \frac{\partial^2 u_x}{\partial X^2} \tag{2.29}$$

$$\rho_0 \ddot{u}_y = \mu \frac{\partial^2 u_y}{\partial X^2} \tag{2.30}$$

and

$$\rho_0 \ddot{u}_z = \mu \frac{\partial^2 u_z}{\partial X^2} \tag{2.31}$$

It is obvious that equation (2.29) supports a longitudinal wave that propagates with speed $(\frac{\lambda+2\mu}{\rho_0})^{\frac{1}{2}}$. Similarly, equations (2.30) and (2.31) support transverse waves with u_y and/or $u_z \neq 0$ and these waves have speed $(\frac{\mu}{\rho_0})^{\frac{1}{2}}$.

Physical meaning of λ and μ:

We can write ϵ_{ij} in the form $(\epsilon_{ij} - \frac{1}{3}\delta_{ij}\epsilon_{kk}) + \frac{1}{3}\delta_{ij}\epsilon_{kk}$. The purpose behind this decomposition is that the tensor with components $(\epsilon_{ij} - \frac{1}{3}\delta_{ij}\epsilon_{kk})$ is traceless and hence such a strain causes no change in volume [Note: Trace($\boldsymbol{\epsilon}$) is the fractional change in volume due to the strain]. On the other hand $\frac{1}{3}\delta_{ij}\epsilon_{kk}$ represents the part of $\boldsymbol{\epsilon}$ that causes change of volume. Using this decomposition, the last two terms on the right hand side of equation (2.26) look like $\frac{1}{2}K(Tr(\boldsymbol{\epsilon}))^2 + \mu \sum_{i,k}(\epsilon_{ik} - \frac{1}{3}\delta_{ik}Tr(\boldsymbol{\epsilon}))^2$ where $K \equiv \lambda + \frac{2}{3}\mu$. K quantifies the increase of free energy due to the change of volume and hence is called the bulk modulus. Similarly, since μ appears as a coefficient of the part that represents the pure shear, it is called the shear

modulus. Using these, the speed of longitudinal wave is $V_P = (\frac{\lambda+2\mu}{\rho_0})^{\frac{1}{2}} = (\frac{K+\frac{4}{3}\mu}{\rho_0})^{\frac{1}{2}}$ and the speed of shear wave is $V_s = (\frac{\mu}{\rho_0})^{\frac{1}{2}}$. In our notation $K = D$ and $\mu = G$.

How are the values of D and G determined from a knowledge of the elastic constants of the individual single crystals that the material is composed of ? Answer to this question is not always unique. Often only a range can be found. Below we summarize the main results that are used in our calculations [43-44].

For cubic systems:
D is uniquely defined and is equal to $\frac{1}{3}(B_{11} + 2B_{12})$. The shear modulus is bounded by G_1^* and G_2^* where

$$G_1^* = G_1 + \frac{3}{\frac{5}{G_2 - G_1} - 4\beta_1} \tag{2.32}$$

and

$$G_2^* = G_2 + \frac{2}{\frac{5}{G_1 - G_2} - 6\beta_2} \tag{2.33}$$

with $G_1 = \frac{1}{2}(B_{11} - B_{12})$, $G_2 = B_{44}$, $\beta_1 = \frac{-3(D+2G_1)}{5G_1(3D+4G_1)}$ and $\beta_2 = \frac{-3(D+2G_2)}{5G_2(3D+4G_2)}$. In the expression of the P-wave velocity $G = \frac{1}{2}(G_1^* + G_2^*)$.

For hcp systems:
The bounds for D and G are given by those corresponding to the Voigt-averaging and the Reuss-averaging and are denoted by the subscripts V and R, respectively. The expressions for D_V, D_R, G_V and G_R are given by (with $B^* = \frac{1}{2}(B_{13} + B_{31})$):

$D_V = \frac{1}{9}(2B_{11} + B_{33} + 2B_{12} + 4B^*)$
$D_R = \frac{(B_{11}+B_{12})B_{33} - 2B^{*2}}{B_{11}+B_{12}+2B_{33}-4B^*}$
$G_V = \frac{1}{30}(12B_{44} + 12B_{66} + B_{11} + B_{12} + 2B_{33} - 4B^*)$
$G_R = \frac{\frac{5}{2}B_{44}B_{66}[(B_{11}+B_{12})B_{33} - 2B^{*2}]}{3D_V B_{44}B_{66} + (B_{44}+B_{66})[(B_{11}+B_{12})B_{33} - 2B^{*2}]}$
Finally, $D = \frac{1}{2}(D_V + D_R)$ and $G = \frac{1}{2}(G_V + G_R)$. The P-wave velocities that are reported here are calculated using these values of D and G.

The range of definitional uncertainty of V_P is calculated in each case as follows:
For cubic systems:
The limiting values of V_P are calculated using the combinations $\{D, G_1^*\}$ and $\{D, G_2^*\}$. Half of the difference between these two values is quoted as the definitional uncertainty of V_P.

For hcp systems:
The limiting values of V_P are calculated using the combinations $\{D_V, G_V\}$ and $\{D_R, G_R\}$. Half of the difference between these two values is quoted as the definitional uncertainty of V_P.

2.4 Density Functional Theory and Density Functional Perturbation Theory

2.4.1 Density Functional Theory (DFT)

Wave function of a system of N electrons can be specified in the form $\psi(\mathbf{r}_1 s_1; \mathbf{r}_2 s_2; .....; \mathbf{r}_N s_N)$ where $\mathbf{r}_i$ and s_i are the position vector and the z-component of the spin, respectively, of the i-th electron. The number density of electrons at the point $\mathbf{r}$ is then given by

$$n(\mathbf{r}) = N \sum_{s_1, s_2, ..., s_N} \int_{\mathbf{r}_2} ... \int_{\mathbf{r}_N} \left| \psi(\mathbf{r} s_1; \mathbf{r}_2 s_2; .....; \mathbf{r}_N s_N) \right|^2 \prod_{i=2}^{N} d^3\mathbf{r}_i \qquad (2.34)$$

Density functional theory is a formulation of the quantum mechanics of a system of many electrons in which the problem of obtaining the energy and the number density function of electrons for the ground state of a system of electrons interacting among themselves and also with a given external potential (created by the nuclei etc.) is reduced to one of minimizing a suitable functional of the positive definite number density function (let's say) f [47-48]. This functional depends parametrically on the locations of the nuclei. Suppose that the i-th nucleus of mass M_i and charge $Z_i e$ is located at the point $R_i (i = 1, 2, ..., K)$. Then for a

given set $\{\mathbf{R}_1, \mathbf{R}_2, ..., \mathbf{R}_K\} \equiv \{\mathbf{R}\}$, the external potential is

$$V_{\{\mathbf{R}\}}(\mathbf{r}) = -\sum_{i=1}^{K} \frac{Z_i e^2}{|\mathbf{R}_i - \mathbf{r}|} \tag{2.35}$$

Then if f denotes the electron number density function, the ground state energy is obtained by minimizing the following functional with respect to f:

$$\begin{aligned} E_{\{\mathbf{R}\}}(f) &= T_0(f) + \frac{e^2}{2} \int_{\mathbf{s}'} \int_{\mathbf{s}''} \frac{f(\mathbf{s}')f(\mathbf{s}'')}{|\mathbf{s}' - \mathbf{s}''|} d^3\mathbf{s}' d^3\mathbf{s}'' + E_{xc}(f) \\ &+ \int V_{\{\mathbf{R}\}}(\mathbf{s}) f(\mathbf{s}) d^3\mathbf{s} + E_n(\{\mathbf{R}\}) \end{aligned} \tag{2.36}$$

where $T_0(f)$ is the minimum possible expectation value of the operator T representing the total kinetic energy of all the electrons with respect to all the wave functions that generate the number density function f (through the definition given in equation (2.34)). The functional $E_{xc}(f)$, called the exchange-correlation functional, is defined so that the sum of the first three terms on the right hand side of equation (2.36) is the minimum possible expectation value of the operator $T + \frac{1}{2}\sum_{i \neq j} \frac{e^2}{|\mathbf{r}_i - \mathbf{r}_j|}$ with respect to all the wave functions consistent with the number density function f. Note that T_0 and E_{xc} are completely independent of the external potential $V_{\{\mathbf{R}\}}$.

In practice the minimization of $E_{\{\mathbf{R}\}}(f)$ is done by recasting the problem into the following steps which need to be undertaken iteratively to achieve self-consistency [47,49-50]:

⓪ Make an initial guess f for the electron number density function.

① Obtain the Kohn-Sham (KS) orbitals $\chi_\alpha(\mathbf{s})$ and energies e_α which are solutions of the following eigenvalue-eigenfunction problem:

$$H_{KS}\chi_\alpha(\mathbf{s}) = e_\alpha \chi_\alpha(\mathbf{s}) \tag{2.37}$$

where H_{KS} is the Kohn-Sham Hamiltonian operator given by

$$H_{KS} = -\frac{\hbar^2}{2m}\nabla_{\mathbf{s}}^2 + \Phi(\mathbf{s}) \tag{2.38}$$

Here m is the mass of the electron and $\Phi(\mathbf{s})$ is the (self-consistent) potential function defined as

$$\Phi(\mathbf{s}) = V_{\{\mathbf{R}\}}(\mathbf{s}) + e^2 \int \frac{f(\mathbf{s}')}{|\mathbf{s} - \mathbf{s}'|} d^3\mathbf{s}' + v_{xc}(\mathbf{s}) \tag{2.39}$$

where $v_{xc}(\mathbf{s}) = \frac{\delta E_{xc}}{\delta f}(\mathbf{s})$ i.e., the functional derivative of the exchange-correlation functional with respect to the number density function f and is to be evaluated at $\mathbf{s}$.

② Occupy the N energetically lowest KS orbitals so that every electron is assigned one. Then construct the revised number density function

$$g(\mathbf{s}) = \sum_{i=1}^{N} |\chi_{\beta(i)}(\mathbf{s})|^2 \tag{2.40}$$

where $\beta(i)$ is the index of the KS orbital occupied by the i-th electron.

③ Self-consistency is said to have been achieved when

$$g(\mathbf{s}) = f(\mathbf{s}) \quad \forall \ \mathbf{s} \tag{2.41}$$

(If it has not been achieved set $f = g$ and go back to step 1.) Once these three equations have been solved and self-consistency is achieved, the ground state electron number density is given by g. The ground state energy is given by

$$\begin{aligned} E_0(\{\mathbf{R}\}) &= \sum_{i=1}^{N} e_{\beta(i)} + E_{xc}(g) - \int v_{xc}(\mathbf{s}) g(\mathbf{s}) d^3\mathbf{s} \\ &- \frac{e^2}{2} \int_{\mathbf{s}'} \int_{\mathbf{s}''} \frac{g(\mathbf{s}') g(\mathbf{s}'')}{|\mathbf{s}' - \mathbf{s}''|} d^3\mathbf{s}' d^3\mathbf{s}'' \end{aligned} \tag{2.42}$$

The exact prescription for evaluating the functional E_{xc} is not known and it is in practice approximated by expressions such as the local density approximation (LDA), the generalized gradient approximation (GGA) etc.

2.4.2 Density Functional Perturbation Theory (DFPT)

As far as lattice vibration is concerned, within the Born-Oppenheimer approximation, the function $E_0(\{\mathbf{R}\})$ (considered for all values of $\{\mathbf{R}\}$ around the equilibrium configuration) serves as the potential energy function for the collective dynamics of the nuclei once the inter-nuclear Coulomb interaction $E_n(\{\mathbf{R}\})$, given by $\frac{1}{2}\sum_{i\neq j}\frac{Z_i Z_j e^2}{|\mathbf{R}_i-\mathbf{R}_j|}$, is added.
Define

$$E(\{\mathbf{R}\}) = E_0(\{\mathbf{R}\}) + E_n(\{\mathbf{R}\}) \tag{2.43}$$

Normal modes are those collective patterns of classical motion of the nuclei in which every nucleus vibrates sinusoidally with a common (circular) frequency ω. They are obtained by solving the equation

$$\sum_{j,b}(D_{ij}^{ab} - \omega^2 M_i \delta_{ij}\delta_{ab})u_j^b = 0 \quad \forall \quad i,\ a \tag{2.44}$$

where u_j^b is the displacement amplitude of the b-th component ($b = x, y, z$) of motion of the nucleus j.
Here

$$D_{ij}^{ab} \equiv \frac{\partial^2 E(\{\mathbf{R}\})}{\partial R_i^a \partial R_j^b} \tag{2.45}$$

with the derivative being evaluated at $\{\mathbf{R}\} = \{\mathbf{R}_0\}$ where $\{\mathbf{R}_0\}$ is the equilibrium configuration of the nuclei i.e. it is the configuration at which the function $E(\{\mathbf{R}\})$ has a local minimum (often it is the global minimum also). D_{ij}^{ab} are the components of what is referred to as the interatomic force constant (IFC) matrix.

Using Hellmann-Feynman theorem it can be shown that

$$\begin{aligned}\frac{\partial^2 E(\{\mathbf{R}\})}{\partial R_i^a \partial R_j^b} &= \int \frac{\partial g(\mathbf{s})}{\partial R_i^a}\frac{\partial V_{\{\mathbf{R}\}}(\mathbf{s})}{\partial R_j^b}d^3\mathbf{s} + \delta_{ij}\int g(\mathbf{s})\frac{\partial^2 V_{\{\mathbf{R}\}}(\mathbf{s})}{\partial R_i^a \partial R_j^b}d^3\mathbf{s} \\ &+ \frac{\partial^2 E_n(\{\mathbf{R}\})}{\partial R_i^a \partial R_j^b}\end{aligned} \tag{2.46}$$

Calculation of the IFC matrix thus requires the knowledge of both the electron number density function at equilibrium (second term on the right hand side of the above equation) and how this density function changes if any of the nuclei

moves (the first term). Basically, the density functional perturbation theory is about how to calculate $\frac{\partial g}{\partial R_i^a}$ i.e., if a small change is made in any of the nuclear coordinates how will the ground state electron number density change in response. Remember that δR_i^a is small. So it creates a small change in $V(\{\mathbf{R}\})$ which is a part of the potential Φ (see eqn. (2.39)) that appears in the KS equation (Eqn.(2.37)). So the KS orbitals and the energies will also change a little due to this small change in the Kohn-Sham Hamiltonian (H_{KS}). The density functional perturbation theory formulates this process of calculating the changes in the KS orbitals and energies (and thus $E_0(\{\mathbf{R}\})$ eventually) in terms of a perturbation theory [51]. Finally, it leads to a coupled set of linear equations.

For an infinite periodic solid the IFC matrix elements depend only on $(\mathbf{R}_i^0 - \mathbf{R}_j^0)$ (the superscript '0' denoting the values at equilibrium) which, in turn, depends on the identities of the two atoms and on the Bravais lattice vector separating the two unit cells in which the two atoms are located. Every normal mode can be taken to be a travelling wave characterized by some wave vector $\mathbf{q}$. For each such normal mode the displacement vector of an atom in the unit cell with coordinates $(n_1\mathbf{A_1} + n_2\mathbf{A_2} + n_3\mathbf{A_3})$ will be proportional to $\exp(i\mathbf{q}.(n_1\mathbf{A_1} + n_2\mathbf{A_2} + n_3\mathbf{A_3}))$. Here $\mathbf{A_1}$, $\mathbf{A_2}$ and $\mathbf{A_3}$ are the basis vectors of the Bravais lattice and $\mathbf{q}$ belongs to the first Brillouin zone. For a given $\mathbf{q}$ the number of normal modes is equal to thrice the number of atoms in the unit cell. Of these three will be of the acoustic type for which $\omega \to 0$ when $|\mathbf{q}| \to 0$.

In practice in DFPT based calculations a uniformly spaced grid of $\mathbf{q}$ points is selected in the first Brillouin zone and the normal mode frequencies are calculated for each of these wave vectors by the DFPT. Then the vibrational frequencies for any arbitrary $\mathbf{q}$ in the first Brillouin zone can be calculated via Fourier interpolation (for example, while calculating the phonon density of states which requires the knowledge of the vibrational frequencies at every point of a very dense $\mathbf{q}$-grid).

Chapter 3

Modifying Birch's law : A scaling approach

3.1 Introduction

In this chapter we explain the genesis of our conjecture, referred to in the Introduction, that when the product of density raised to the power one-third and the speed of elastic wave is plotted against density it is expected to give a better linear fit than when the speed alone is plotted against density. It is based on two ingredients: (i) The observation [52-53] that the phonon dispersion relation for many elemental solids satisfies a scaling relation at high enough pressures – this relation being that the vibrational frequency for a particular wave vector, when measured in suitable units that depend only on the applied pressure, is a function only of the product of the wave vector and a length scale defined by the number of particles per unit volume. The functional dependence of the rescaled frequency on the rescaled wave vector depends on the particular branch of the dispersion relation. Of course, we are interested primarily in the acoustic branches. (ii) The empirical observation [54] that the phonon frequency, averaged over the entire vibrational spectrum, is often, to a very good approximation, a linear function of density. In the following two sections we elaborate on these two observations before explaining, in the final section, how a combination of these two ingredients leads to our conjecture.

3.2 Scaling form of the phonon dispersion relation

It has been pointed out in two recent works[52-53] that the high pressure phonon dispersion relation in many elemental solids has the following structure:

$$\omega_i(\mathbf{k}) = W(P)F_i(n^{-1/3}\mathbf{k}) \tag{3.1}$$

Here n is the number density of particles, $\omega_i(\mathbf{k})$ is the frequency of the phonon of the i-th branch with wave vector $\mathbf{k}$. F_i is a function that becomes independent of the pressure P in the limit of large enough pressure i.e. this statement is *asymptotically* exact. $W(P)$ is the scale of frequency at pressure P and its exact value is determined by the normalization condition

$$\sum_i \int F_i(\mathbf{s})d^3\mathbf{s} = 1 \tag{3.2}$$

The physically interesting significance of equation (3.1) is that the dependence of the rescaled frequency $\omega(\mathbf{k})/W(P)$ on the rescaled wave vector $n^{-1/3}\mathbf{k}$ becomes eventually independent of pressure as pressure keeps increasing i.e. if suitable units are used for the frequency and the wave vector, the dispersion relation is *asymptotically* independent of pressure.

We will first show that the equation (3.1) is exact for a class of model isotropic solids consisting of identical particles for which the inter-atomic interaction is described by positive homogenous potentials (PHP) [53]. A positive homogenous potential V satisfies the requirement that

$$V(\alpha\mathbf{r_1}, \alpha\mathbf{r_2}, ..., \alpha\mathbf{r_i}, ...) = \alpha^Q V(\mathbf{r_1}, \mathbf{r_2}, ..., \mathbf{r_i}, ...) \tag{3.3}$$

where $\mathbf{r}_i$ is the position vector of the i-th particle, α is a positive real number. Q is called the degree of homogeneity and is usually a negative integer $-m$. The most common instance of such a potential is when the total potential energy of a solid, made up of identical particles, is a sum over all the pair potential energies. The pair potential will typically have the structure $\phi_1(r) - \phi_2(r)$ where ϕ_1, the repulsive part, varies with r as r^{-m} at shorter distances. $\phi_2(r)$ describes the attractive part of the interaction [Please note that a solid cannot exist at zero

pressure without the attractive part]. If the ratio $\phi_2(r)/\phi_1(r)$ also goes to zero in the limit of r going to zero it follows that the potential energy will behave increasingly accurately like a positive homogenous potential in the high pressure limit when all the inter-particle distances have shrunk enough.

If there are N particles in the unit cell, the vibrational frequencies $\omega_i(\mathbf{k})$ $[i = 1, 2, ..., 3N]$ are proportional to the square-roots of the $3N$ eigenvalues of the dynamical matrix $\mathcal{D}(\mathbf{k})$ – which is the Fourier transform of the force-derivative matrix $D(\mathbf{R})$. To be precise

$$\mathcal{D}(\mathbf{k}) \equiv \sum_{\mathbf{R}} D(\mathbf{R}) e^{-i\mathbf{k}.\mathbf{R}} \tag{3.4}$$

where $D(\mathbf{R})$ is the matrix of second derivatives of the potential energy with respect to the coordinates of two particles located in two unit cells separated by the Bravais lattice vector $\mathbf{R}$. If we denote the basis vectors by $\mathbf{a}_1$, $\mathbf{a}_2$ and $\mathbf{a}_3$, an arbitrary Bravais lattice vector $\mathbf{R}$ can be written as $n_1\mathbf{a}_1 + n_2\mathbf{a}_2 + n_3\mathbf{a}_3$, where n_1, n_2 and n_3 are integer-valued, and equation (3.4) can be rewritten as

$$\mathcal{D}(\mathbf{k}) = \sum_{n_1,n_2,n_3} T(n_1, n_2, n_3) e^{-i\mathbf{k}.(n_1\mathbf{a}_1+n_2\mathbf{a}_2+n_3\mathbf{a}_3)} \tag{3.5}$$

Suppose now we vary the applied pressure P. Since the interactions in the solid are isotropic it will not change the shape of the unit cell (and hence, that of the first Brillouin zone) but will alter the scale l of the linear dimension of the unit cell. If v and ϵ denote the volume of the unit cell and energy per unit cell, respectively, $v \propto l^3$ while $\epsilon \propto l^{-m}$. Thus the pressure $P = -\frac{\partial \epsilon}{\partial v} \propto l^{-(m+3)}$. The number density $n \propto \frac{1}{v} \propto l^{-3}$. In equation (3.5) $T(n_1, n_2, n_3)$ is the second spatial derivative of the potential energy. Thus, for a given set of values of $\{n_1, n_2, n_3\}$, $T = f_1(n_1, n_2, n_3) l^{-(m+2)}$ while $\mathbf{k}.(n_1\mathbf{a}_1 + n_2\mathbf{a}_2 + n_3\mathbf{a}_3)$ is the scalar product of $l\mathbf{k}$, which is proportional to $n^{-1/3}\mathbf{k}$, and a vector that depends only on $\{n_1, n_2, n_3\}$ and the shape of the unit cell (neither of which depends on pressure) = A function of $n^{-1/3}\mathbf{k}$ that depends parametrically on $\{n_1, n_2, n_3\} = f_2(n^{-1/3}\mathbf{k}; n_1, n_2, n_3)$.

Thus

$$\begin{aligned} \mathcal{D}(\mathbf{k}) &= l^{-(m+2)} \sum_{n_1,n_2,n_3} f_1(n_1,n_2,n_3) e^{-if_2(n^{-\frac{1}{3}}\mathbf{k};\ n_1,n_2,n_3)} \\ &= l^{-(m+2)} f_3(n^{-\frac{1}{3}}\mathbf{k}) \end{aligned} \tag{3.6}$$

Note that $l \propto P^{-\frac{1}{m+3}}$. Thus $\mathcal{D}(\mathbf{k})$ is proportional to $P^{\frac{m+2}{m+3}} f_3(n^{-\frac{1}{3}}\mathbf{k})$. Since $\omega_i(\mathbf{k})$ is proportional to the square-root of some eigenvalue of $\mathcal{D}(\mathbf{k})$ we finally get the result that $\omega_i(\mathbf{k}) = P^{\frac{m+2}{2m+6}}$ multiplied by a function of $n^{-1/3}\mathbf{k}$ that depends on the particular branch of the vibrational spectrum. This is what we set out to prove. But we also have the additional result that $W(P) \propto P^{\frac{m+2}{2m+6}}$.

In a real material, with the possible exception of inert gas solids, the potential energy function is not expected to be of the PHP type. Yet, it has been demonstrated recently [52] that the vibrational spectra of many elemental solids do satisfy equation (3.1) to a very good approximation. To check this we first note that, due to the normalization condition given by equation (3.2), the average phonon frequency $< \omega > (P) \propto W(P)$. If we choose the wave vector $\mathbf{k}$ to be any of the special symmetry points in the first Brillouin zone the value of $n^{-1/3}\mathbf{k}$ is independent of the pressure. Thus, for any such special symmetry point, the ratio $\omega_i(\mathbf{k})/ < \omega > (P)$, when plotted as a function of P, should saturate when the pressure becomes high enough. This is what was found in the DFT-based studies of the vibrational spectra [52]. Figure 3.1 shows an example of such behaviour for magnetic nickel.

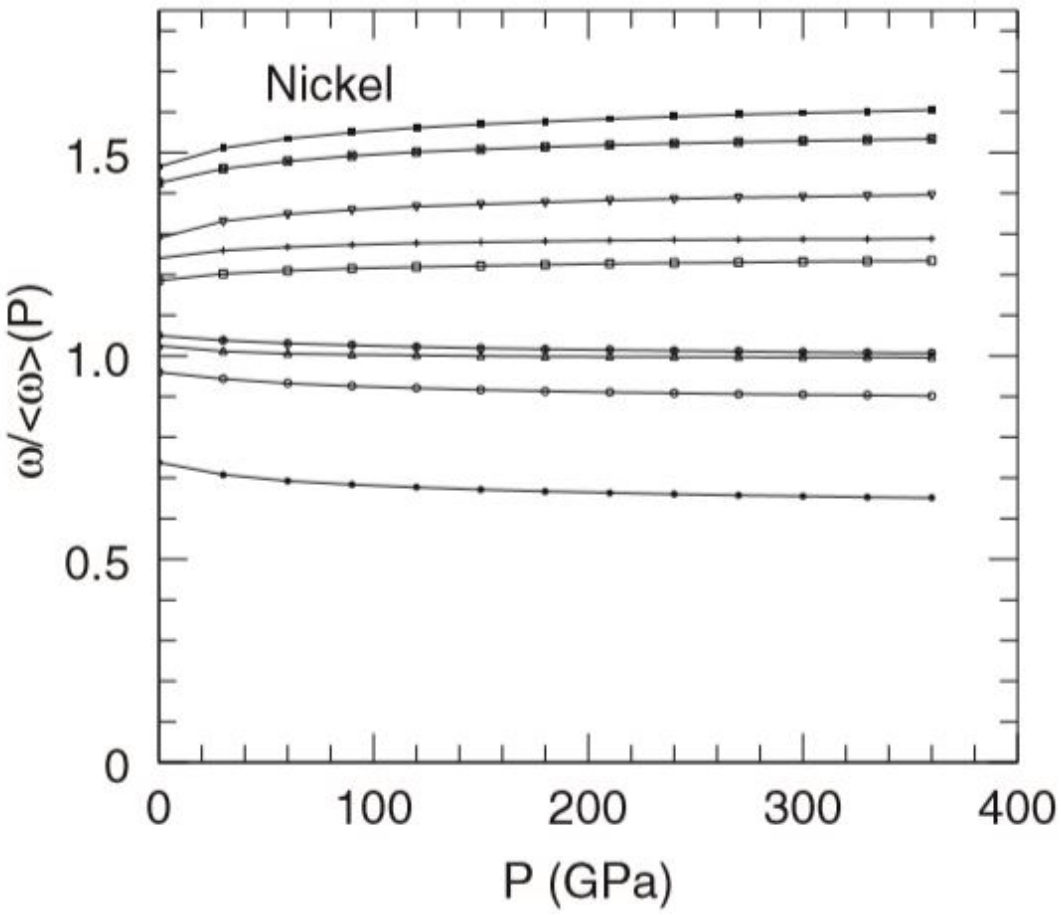

Figure 3.1: Evolution of the ratio $\omega/ < \omega > (P)$ with pressure (P) [52] is shown for the modes LA, TA1, TA2 at the symmetry points X, K, L, and W for magnetic nickel. From top to bottom: L(LA), X(LA), K(LA), W(LA and TA2: degenerate), K(TA2),X(TA2 and TA1: degenerate),W(TA1),K(TA1), and L(TA2 and TA1: degenerate).

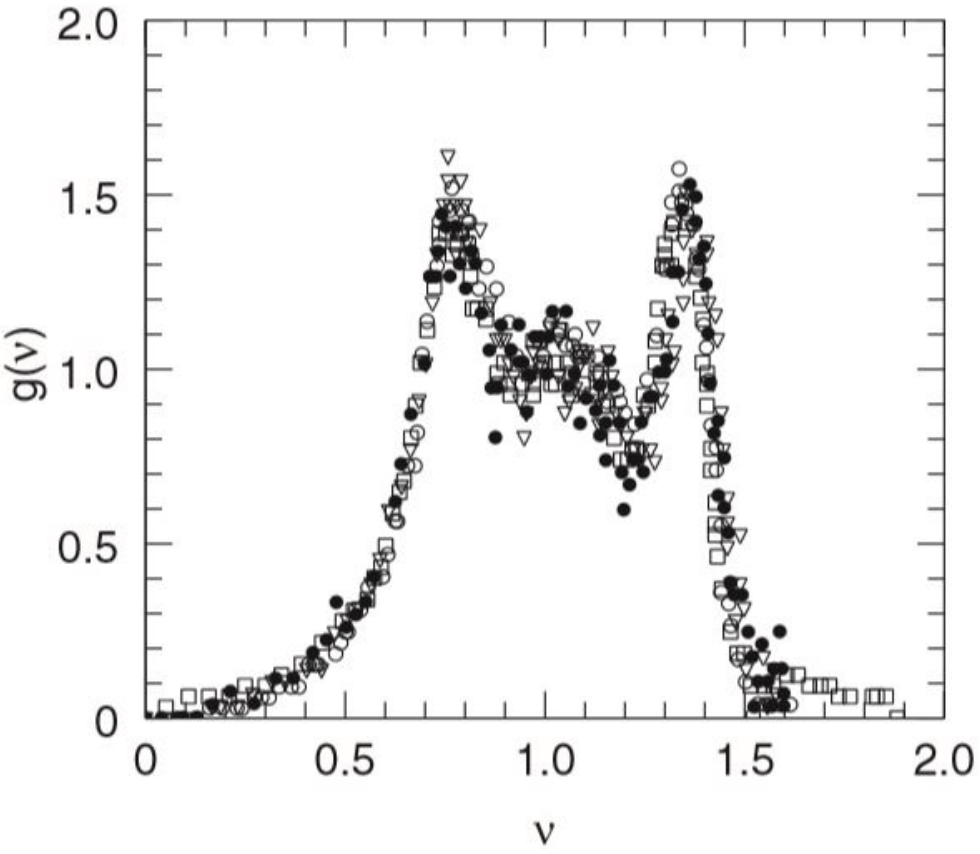

Figure 3.2: Superposition of experimentally measured [55] normalized phonon density of states for hcp-iron at 77 (filled circle), 106 (open inverted triangle), 133 (open square) and 171 (open circle) GPa.

Another implication of the scaling hypothesis is the following: Suppose the phonon density of states is expressed as a function of the normalized frequency ν ($\equiv \frac{\omega}{<\omega>(P)}$). Call it $g(\nu)$ and normalize it so that $\int g(\nu)d\nu = 1$ (or any other constant). Then the plot of $g(\nu)$ vs. ν will saturate when the pressure becomes high enough. This is indeed what is seen (figure 3.2) in the experimentally measured vibrational spectra of hcp-iron. In fact, this scaling form of the vibrational spectrum was proposed [55] before the more detailed form contained in equation (3.1) was introduced in [52]. Hints of such behaviour are available elsewhere also [56-60].

3.3 Linear relation between average phonon frequency and density

For several materials we have found [54], through density functional perturbation theory calculations of vibrational spectra at zero temperature, that the average vibrational frequency is an excellent linear function of density. We show some examples in the following figures:

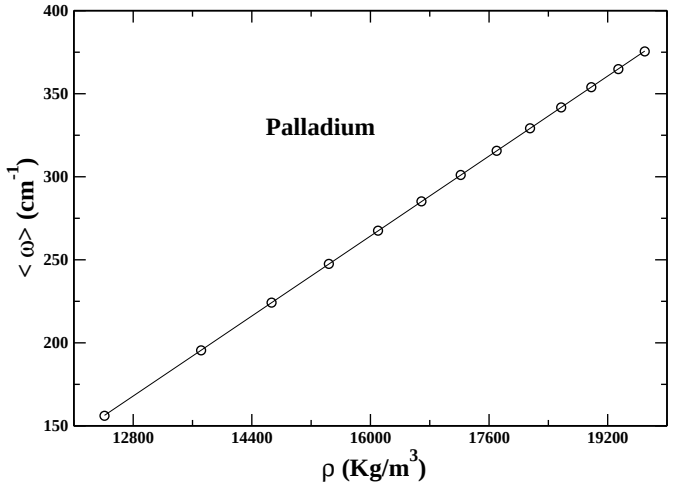

Figure 3.3: Plot of the average phonon frequency ($< \omega >$) against density (ρ) for palladium. The average frequency is computed via a pseudo-potential based electronic structure calculation.

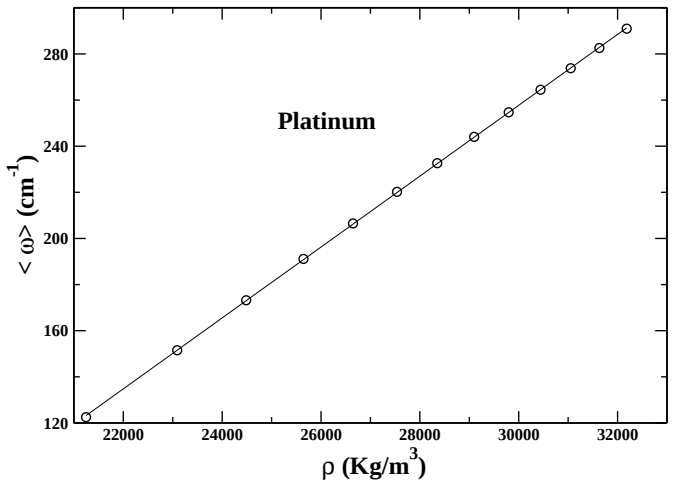

Figure 3.4: Plot of the average phonon frequency ($< \omega >$) against density (ρ) for platinum. The average frequency is computed via a Projector-Augmented-Wave (PAW) based electronic structure calculation.

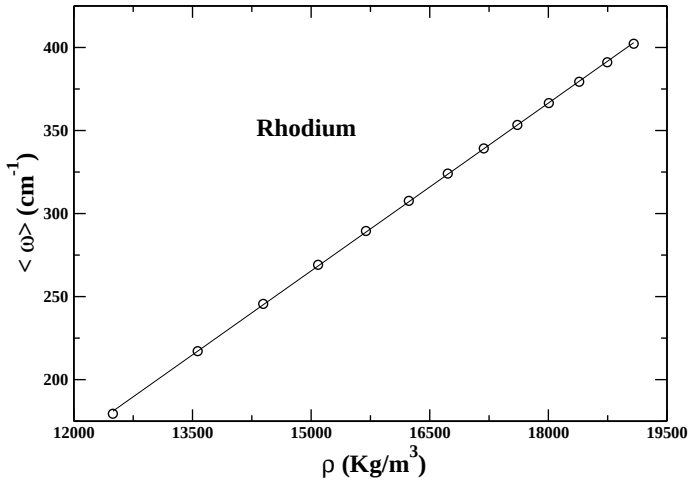

Figure 3.5: Plot of the average phonon frequency ($< \omega >$) against density (ρ) for rhodium. The average frequency is computed via a PAW based electronic structure calculation.

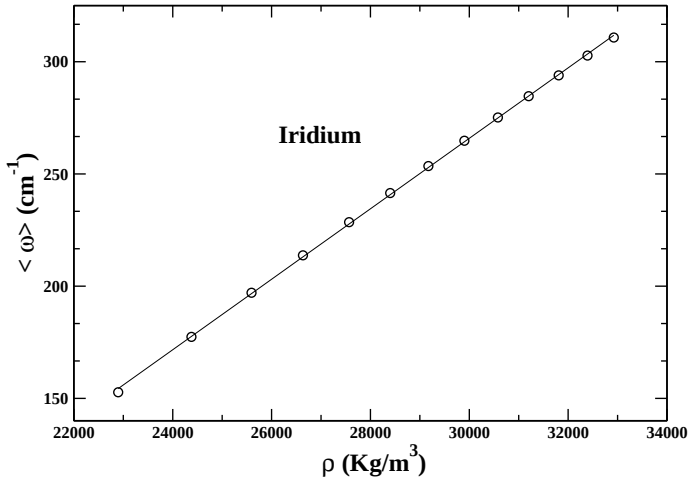

Figure 3.6: Plot of the average phonon frequency ($< \omega >$) against density (ρ) for iridium. The average frequency is computed via a pseudo-potential based electronic structure calculation.

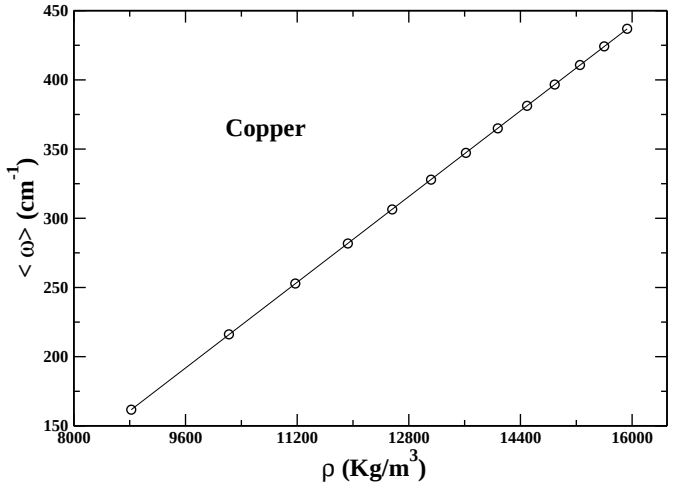

Figure 3.7: Plot of the average phonon frequency ($< \omega >$) against density (ρ) for copper. The average frequency is computed via a pseudo-potential based electronic structure calculation.

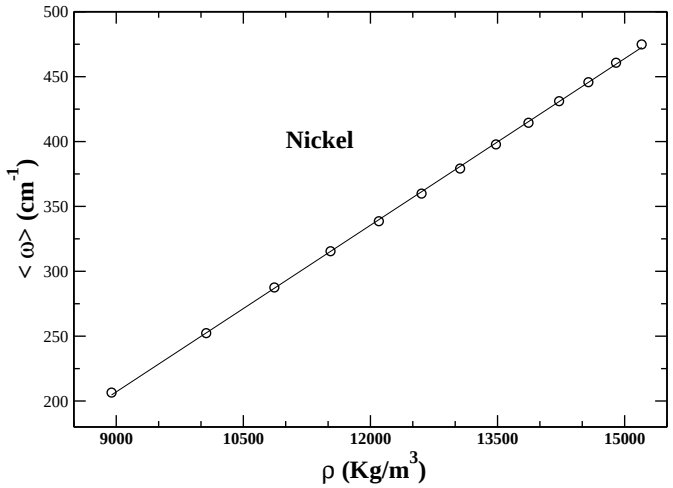

Figure 3.8: Plot of the average phonon frequency ($< \omega >$) against density (ρ) for nickel (magnetic). The average frequency is computed via a pseudo-potential based electronic structure calculation.

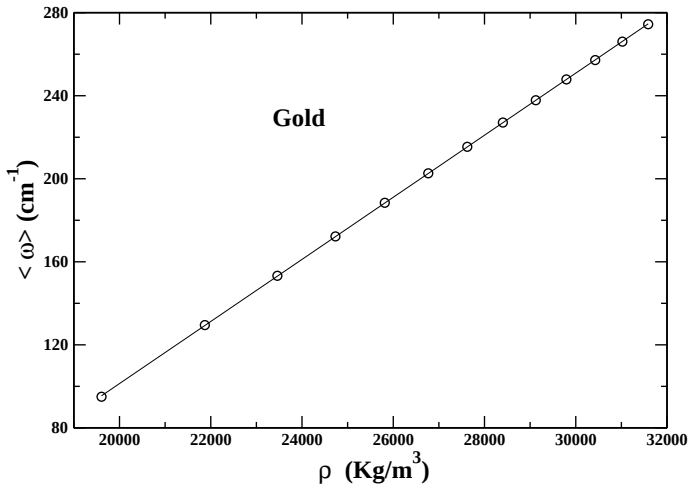

Figure 3.9: Plot of the average phonon frequency ($< \omega >$) against density (ρ) for gold. The average frequency is computed via a pseudo-potential based electronic structure calculation.

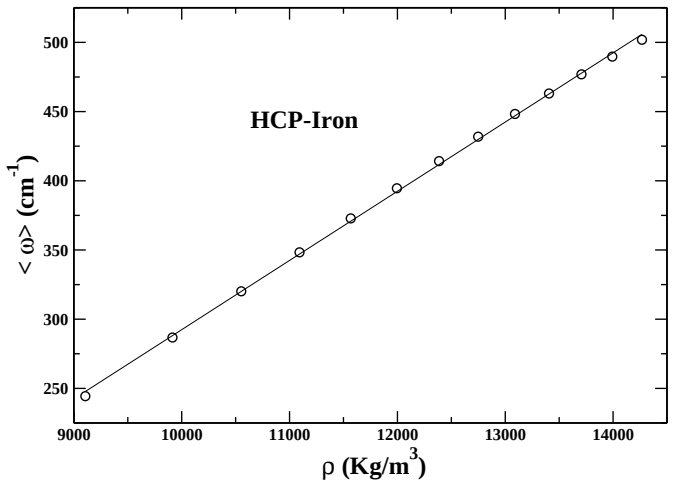

Figure 3.10: Plot of the average phonon frequency ($< \omega >$) against density (ρ) for hcp-iron (non-magnetic). The average frequency is computed via a pseudo-potential based electronic structure calculation.

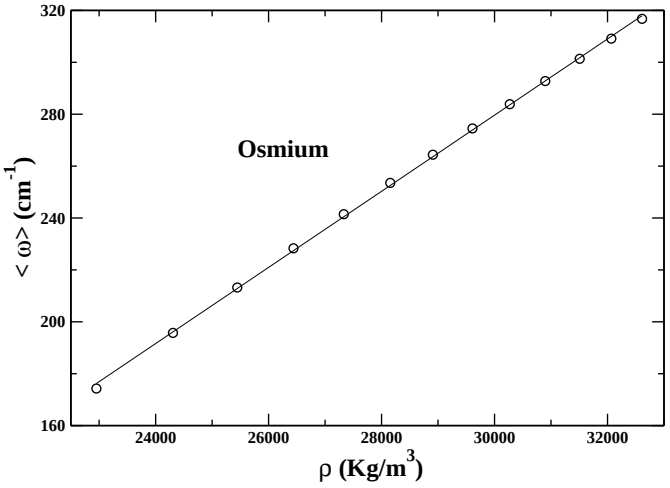

Figure 3.11: Plot of the average phonon frequency ($< \omega >$) against density (ρ) for osmium. The average frequency is computed via a pseudo-potential based electronic structure calculation.

3.4 Genesis of our conjecture

Finally, we show in this section how a combination of equation (3.1) with the observation of linear dependence of average phonon frequency on density leads to our proposal for a modification of the conventional form of the Birch's law. Equation (3.1) is applicable to all the branches of the phonon dispersion relation. However, we are going to focus only on the three acoustic branches for which $\omega \to 0$ as $|\mathbf{k}| \to 0$ and $\lim_{k\to 0^+} \omega_i(k\hat{\mathbf{t}})/k$ = Speed of propagation of the i-th type of acoustic wave in the direction of $\hat{\mathbf{t}}$ (which is a unit vector) = $c_i(\hat{\mathbf{t}})$. From equation (3.1),

$$\lim_{k\to 0^+} \frac{\partial \omega_i(k\hat{\mathbf{t}})}{\partial k} = W(P) \lim_{k\to 0^+} \frac{\partial}{\partial k} F_i(n^{-\frac{1}{3}} k\hat{\mathbf{t}}) \tag{3.7}$$

[Please note that F_i is not an analytic function of its argument $\mathbf{s}$ around $\mathbf{s} = \mathbf{0}$ for the acoustic branches.]

Define $G_i(n^{-\frac{1}{3}}k; \hat{\mathbf{t}}) = F_i(n^{-\frac{1}{3}} k\hat{\mathbf{t}})$ for $k > 0$ (for a particular value of $\hat{\mathbf{t}}$). Denote $n^{-\frac{1}{3}}k = x$. Then $\lim_{x\to 0^+} \frac{\partial G_i}{\partial x}$ is well defined and is finite. Let us call this limit

$\theta_i(\hat{\mathbf{t}})$. Then

$$c_i(\hat{\mathbf{t}}) = W(P)n^{-\frac{1}{3}}\theta_i(\hat{\mathbf{t}}) \tag{3.8}$$

and consequently

$$c_i(\hat{\mathbf{t}})n^{\frac{1}{3}} = W(P)\theta_i(\hat{\mathbf{t}}) \tag{3.9}$$

We have already recorded the empirical observation that the average phonon frequency $< \omega > (P)$ is a linear function of density. Since $W(P)$ is proportional to $< \omega > (P)$ the same statement is true of $W(P)$ also. It follows immediately from equation (3.9) that: ***the product of elastic wave speed and density raised to the power one-third can be expected to be a linear function of density*** [This is the modified version (sometimes referred to as hypothesis H1) of the Birch's law that we will compare with the conventional form (sometimes referred to as hypothesis H2) of the Birch's law through much of the present thesis]. However, this expectation must be tempered with the following points of caution: (i) The scaling law expressed by equation (3.1) is *asymptotic* in nature i.e. it is supposed to hold good only in the limit of high pressure – whereas, in practice, the lower limit of the range of pressures that we will be interested in will usually go down to about 15 GPa; (ii) We do not have a fundamental justification of the validity of the scaling law even in those cases where it is found to work; and (iii) The observation of the linear dependence of the average phonon frequency on density is an empirical one. Thus it is necessary to test the extent of validity of this modified version of the Birch's law on a case by case basis.

This is what the remaining chapters are largely devoted to. In chapter 4 we examine data that already exists in the literature. These include laboratory experiments and/or computational data on elastic constants and/or elastic wave speed. When the data is available only for the elastic constants we convert them to elastic wave speed by using the methods explained in chapter 2. In chapter 5 we examine data generated by us (by using the density functional theory of electronic structure calculation) for elastic wave speed in various elemental solids, over a large range of densities in each case, at zero temperature. The relatively high precision of this data enables us to meaningfully discriminate between the two versions of the Birch's law. In chapter 6 we progress to the far more challenging calculations at finite temperature.

Chapter 4

Analysis of data in the existing literature

4.1 Introduction

We now begin the examination of various pieces of evidence to compare the two alternative formulations of the Birch's law. In this chapter we take up the data that already exists in the published literature. These are from laboratory experiments and various computational studies. During our search of the literature we accepted only those data for analysis which appeared to be reasonably precise and also covered a sufficiently wide range of densities. This second criterion is quite essential. Over a range of densities not sufficiently wide the two versions of the Birch's law cannot be discriminated since the factor of density raised to the power of one-third (that multiplies the elastic wave speed in the modified Birch's law) will not vary enough. In some cases only the data for elastic constants was available. These have been converted by us, using the relevant techniques described in chapter 2, to elastic wave speeds. As we shall see these data are of varying levels of precision and hence not all of them will permit conclusive analysis. In this chapter, in all cases the data that we analyze is read via the application of a highly precise data extraction software on the electronic version of the published work.

4.2 Methodology of analysis

In all cases the basic data is a set of values of some kind of elastic wave speed $(y_1, y_2, ..., y_N)$ measured or computed for a set of densities $(x_1, x_2, ..., x_N)$. And the question to be addressed is this: Which of the plots, y versus x or $yx^{1/3}$ versus x, is described more accurately by a straight line ? In some cases even a visual examination of the two graphs will make the answer evident. But, in general, one cannot rely on visual examination and a more quantitative parameter has to be constructed. Since the question is one of deviation from the best fit straight line given by, let's say $y = ax + b$, obviously larger absolute values of the difference $y_i - ax_i - b$ will mean poorer compliance with a linear dependence. To make the metric of non-compliance dimensionless this can be scaled by something with the dimension of y. We can choose y_i itself for this purpose. However, this will increase the weight of the data with smaller value of y. To avoid this we can choose the range of variation of y across all values of x (i.e. $y_{max} - y_{min}$) as the scale so that the absolute deviation will get equal weightage at all values of x. Thus, for a given data point, the absolute value (f_i) of the fractional deviation $(y_i - ax_i - b)/(y_{max} - y_{min})$ will be taken as the dimensionless measure of non-compliance. Now the maximum value of this ratio across all values of x (f_{max}) is a candidate for a measure of the deviation from the best linear fit. However, this measure is too sensitive to the presence of any outlier in the data. Hence a somewhat safer measure would appear to be the average $f_{mean} \equiv \sum_i f_i/N$. In our calculations we will always compute both the maximum fractional deviation f_{max} and the mean fractional deviation f_{mean}.

Having defined the measure of the deviation from linear fit, the comparison of the two hypotheses H1 and H2 is completely straightforward. Whichever gives the smaller value of f_{max} and f_{mean} has to be taken as giving the more accurate description. The ratio of the values of f_{max} or f_{mean} for the two hypotheses will sometimes be referred to as the factor of superiority of one version of the Birch's law over the other. In case f_{max} and f_{mean} give conflicting conclusions it may indicate the presence of serious outliers in the data or it may mean that our procedure is indeterminate. This happens only with extreme rarity in all the cases we have dealt with.

4.3 Results

Due to its importance in terrestrial geophysics iron is the material most extensively studied experimentally at extreme pressures and sometimes, simultaneously, at moderately high temperatures also. Most previous experimental verifications of the Birch's law, involving data over a wide range of densities, have been carried out for iron only. In these ranges of thermodynamic parameters iron has the hexagonal-close-packed (hcp) structure. Several different experimental techniques have been employed in these experiments to measure the speed of elastic waves. The data that we analyse have been generated via one of the following three techniques: (a) Inelastic x-ray scattering (IXS), (b) Nuclear Resonant Inelastic x-ray scattering and (c) Impulsive Stimulated Light Scattering (ISLS). The first two methods probe phonons. The IXS is the standard inelastic scattering of x-rays by phonons – the measurements being made possible by the advent of high intensity synchrotron radiation. On the other hand the NRIXS measures partial phonon density of states of materials containing isotopes susceptible to Mössbauer resonance. However, in the case of pure Fe-57, it is the total phonon density of states that is measured. ISLS experiments create sound waves by the superposition of two laser beams at some angle of convergence. This superposition creates an interference pattern and the spatially alternating heating that the absorption of this interference pattern causes, ultimately creates counter-propagating sound waves. Finally, this acoustic wave is probed by another light beam.

In our analysis of experimental data on iron we focus, to a large extent, on the data summarized recently in a review article [26]. Figure 4.1 shows a combined plot of the data for the P-wave velocity (V_P) against density (ρ) from several experiments – along with a best linear fit to this combined data. The first important point to notice is the presence of a large amount of scatter in the data – both within individual experiments and amongst the different experiments. This is partially due to the inherent uncertainties in these extremely difficult experiments. The other important reason is that the thermodynamic conditions are not always the same in these experiments. This level of irregularity in the data means that the metrics that we defined in the previous section are substantially meaningless as a tool of comparison between the two hypotheses of interest to

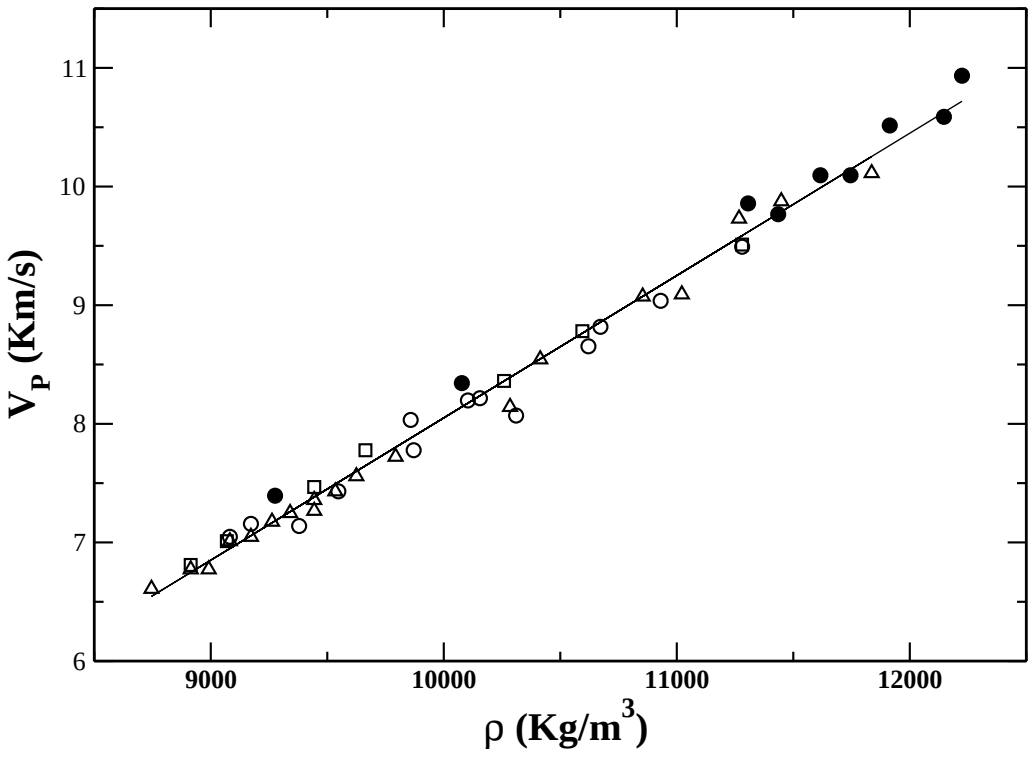

Figure 4.1: The P-wave speed in hcp-iron (V_P), as measured in various experiments, is plotted against density. The data are extracted from figure 6 of [26]. Original source of data: Open circle [15,19]; Open square [17]; Open triangle [25]; and filled circle [23].

us. The experimental error bars overwhelm the metrics designed for data that is assumed to be of a high-precision and smoothly-varying type. However, we present, in figure 4.2 a replot of the data in figure 4.1 in the $V_P\rho^{1/3}$ versus ρ format – along with a best linear fit. A visual comparison between figures 4.1 and 4.2 shows that this set of data is certainly not incompatible with our proposed modification to the Birch's law. In fact the data cannot differentiate between H1 and H2 on the basis of the visually apparent quality of linear fit in these two figures. This is also supported by the data in table 4.1 where we present the values of our metrics for the data from the individual experiments (the results of which are combined in figure 4.1) and also for the combined data set. Not surprisingly we find, in the first six rows of table 4.1, that the values of both f_{max} and f_{mean} are rather large in absolute value. And, even though the values of both f_{max} and f_{min} are nominally always less for the modified Birch's law, the differences are not all that significant. This implies that our test is not particularly meaningful for these data sets.

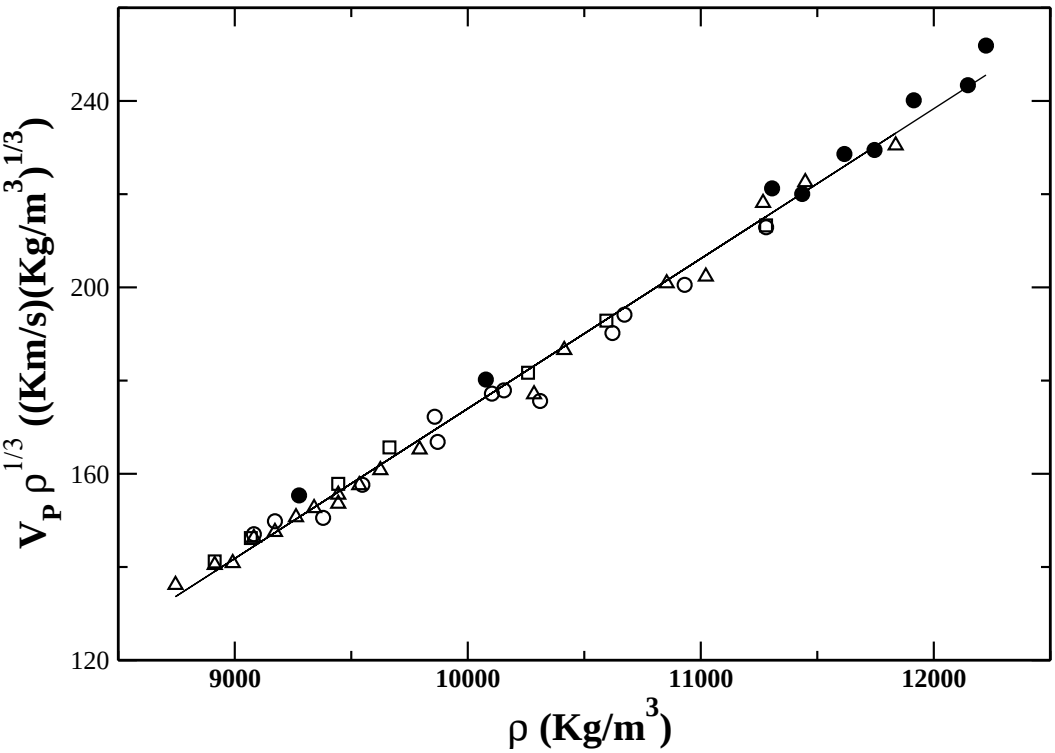

Figure 4.2: The experimental data shown in figure 4.1 are now presented in the format $V_P\rho^{1/3}$ against density (ρ).

Table 4.1: Data for maximum and mean fractional deviation

System	Velocity	Maximum fractional deviation		Mean fractional deviation	
		$v-\rho$	$v\rho^{1/3}-\rho$	$v-\rho$	$v\rho^{1/3}-\rho$
hcp-fe[a]	P-wave	4.1×10^{-2}	4.0×10^{-2}	2.4×10^{-2}	2.0×10^{-2}
hcp-fe[b]		1.1×10^{-1}	9.5×10^{-2}	3.9×10^{-2}	3.2×10^{-2}
hcp-fe[c]		2.7×10^{-2}	1.7×10^{-2}	1.1×10^{-2}	6.1×10^{-3}
hcp-fe[d]		6.1×10^{-2}	5.6×10^{-2}	2.0×10^{-2}	1.8×10^{-2}
hcp-fe[e]		6.2×10^{-2}	4.4×10^{-2}	3.7×10^{-2}	2.6×10^{-2}
hcp-fe[f]		9.1×10^{-2}	8.0×10^{-2}	2.5×10^{-2}	2.2×10^{-2}
CaO	P-wave	2.3×10^{-2}	1.2×10^{-2}	9.7×10^{-3}	4.7×10^{-3}
$CaSiO_3$		3.1×10^{-2}	1.6×10^{-2}	1.6×10^{-2}	8.0×10^{-3}
MgO		2.8×10^{-2}	9.5×10^{-3}	1.1×10^{-2}	3.9×10^{-3}
$MgSiO_3$		3.4×10^{-2}	1.8×10^{-2}	1.4×10^{-2}	7.3×10^{-3}
$Fe_{0.85}Si_{0.15}$	Bulk	2.6×10^{-2}	6.4×10^{-3}	1.0×10^{-2}	2.2×10^{-3}
Fe_3C		2.0×10^{-2}	5.8×10^{-3}	7.8×10^{-3}	1.4×10^{-3}
Fe_3S		2.2×10^{-2}	2.6×10^{-3}	8.8×10^{-3}	1.1×10^{-3}
FeO		2.4×10^{-2}	2.3×10^{-3}	1.0×10^{-2}	1.1×10^{-3}
FeS_2		1.8×10^{-2}	4.6×10^{-3}	9.6×10^{-3}	2.7×10^{-3}
FeSi		2.0×10^{-2}	4.8×10^{-3}	8.3×10^{-3}	1.5×10^{-3}
FeS		1.8×10^{-2}	4.5×10^{-3}	8.4×10^{-3}	1.7×10^{-3}
Fe		2.3×10^{-2}	5.5×10^{-3}	1.0×10^{-2}	2.4×10^{-3}

a: [23]; b: [15,19]; c: [17]; d: [25]; e: [20]; f: [23,15,19,17 and 25 combined].

The next four rows in table 4.1 relate to data generated [61] for P-wave velocity with density-functional-theory-based calculations at zero temperature (as we will do in the chapter 5) for some oxides and silicates of interest in the studies of the mantle of the Earth. The data actually used in our analysis was extracted from figure 8 of [61]. The remaining entries in this table are for bulk speed in iron and several of its compounds. To get the bulk speed the bulk modulus and the density are measured at the relevant thermodynamic conditions via x-ray diffraction measurements in a diamond anvil cell. Then the bulk speed is defined as the square root of the bulk modulus divided by the density. The data that we use are extracted from figure 3 of [20]. Inspection of the values of f_{max} and f_{mean} in the relevant rows of table 4.1 makes it evident that the values of either f_{max} or f_{mean} are consistently several times smaller for the $V\rho^{1/3} - \rho$ plot. The reduction factor for the metric is however variable – going all the way up to almost 10 in two instances.

Table 4.2: Data for maximum and mean fractional deviation

System	Data type*	Maximum fractional deviation		Mean fractional deviation	
		$v - \rho$	$v\rho^{1/3} - \rho$	$v - \rho$	$v\rho^{1/3} - \rho$
Ar	C	2.8×10^{-2}	8.7×10^{-3}	1.3×10^{-2}	4.2×10^{-3}
	C	2.9×10^{-2}	9.5×10^{-3}	1.4×10^{-2}	4.2×10^{-3}
Ar	E	1.9×10^{-2}	8.5×10^{-3}	6.7×10^{-3}	3.3×10^{-3}
	E	3.3×10^{-2}	3.1×10^{-3}	1.1×10^{-2}	1.2×10^{-3}
Co	E	5.3×10^{-2}	3.6×10^{-2}	2.7×10^{-2}	1.8×10^{-2}
	E	4.1×10^{-2}	3.1×10^{-2}	2.0×10^{-2}	1.5×10^{-2}
	C	1.9×10^{-2}	9.9×10^{-3}	1.2×10^{-2}	6.6×10^{-3}
Ru	C	2.0×10^{-2}	6.4×10^{-3}	1.4×10^{-2}	4.6×10^{-3}
He	E	5.5×10^{-2}	3.6×10^{-2}	4.8×10^{-2}	3.1×10^{-2}
Fe	C	1.7×10^{-2}	1.3×10^{-2}	1.1×10^{-2}	4.6×10^{-3}
Kr	E	2.1×10^{-2}	8.4×10^{-3}	4.6×10^{-3}	2.8×10^{-3}
	E	1.0×10^{-2}	1.1×10^{-2}	3.5×10^{-3}	4.6×10^{-3}
Fe	C	2.3×10^{-2}	1.0×10^{-2}	9.8×10^{-3}	5.9×10^{-3}
$Fe_{0.875}Si_{0.125}$	C	1.3×10^{-2}	3.6×10^{-3}	8.9×10^{-3}	2.2×10^{-3}

* E: Experimental work; C: Computational work.

Now we proceed to the entries of table 4.2. These data sets represent outcomes of either laboratory experiments or computation. First of all, we identify all the rows. Row 1: Computational work on argon based on density functional theory [62]; the velocity data used is the minimum longitudinal acoustic velocity in a single crystal. Row 2: Same as row 1 but the velocity data used is the maximum longitudinal acoustic velocity in a single crystal. Row 3: Experimental work on argon [63]; the velocity data used is the minimum longitudinal acoustic velocity in a single crystal. Row 4: Same as row 3 but the velocity data used is the maximum longitudinal acoustic velocity in a single crystal. Row 5: Measurement [64] of P-wave velocity in hcp-cobalt in an impulsive stimulated light scattering experiment; data analysed is taken from table I of [64]. Row 6: Inelastic x-ray scattering measurement of P-wave velocity in hcp-cobalt [64]; data analysed is taken from table I of this reference. Row 7: Density-functional-theory-based calculation on hcp-cobalt [65]. Data analysed is the value of P-wave velocity taken from table I of [64]. Row 8: Density-functional-theory-based calculation on hcp-ruthenium [66]; elastic constants and unit cell volumes available in table V of this reference are used by us to calculate P-wave velocity as a function of density. Row 9: Brillouin scattering measurements on hcp-helium-4 in a diamond anvil cell [67]; values of elastic constant and density available in tables I and II were used by us to calculate P-wave velocity. Row 10: Density-functional-theory-based calculation on hcp-iron [68]; data analysed is taken directly from table 1 of this work. Row 11: Experimental work on cubic-krypton using the technique of Brillouin scattering [69]; figures 2 and 5 of this reference were used to get the maximum longitudinal acoustic velocity as a function of density. Row 12: Same as row 11 but the velocity data is the minimum longitudinal acoustic velocity. Row 13: Density-functional-theory-based calculation on hcp-iron [70]; data from figures 1 and 3(a) have been used to calculate P-wave velocity as a function of density. Row 14: Same as row 13 but for $Fe_{0.875}Si_{0.125}$. It may be noted that all the density-functional-theory-based calculations referred to above are at zero temperature.

Inspection of the tables 4.1 and 4.2 and comparison of the values of f_{max} and/or f_{mean} for the two alternative laws leads us to conclude that the modified version of the Birch's law works essentially consistently more accurately than the

standard version – although the factor of superiority is not uniform. Unfortunately, the available experimental data often contains a level of uncertainty that is much larger than the small systematic differences between the predictions of the two alternative versions. It is interesting to recognize that the conventional Birch's law would seem to work fairly well in an absolute sense if one judges merely by the values of f_{max} and f_{mean}. Often it is only a few percent. However, if the primary objective is to be able to extrapolate speed data from the low density domain to the high density domain with an acceptable level of precision this may not be good enough. The modified version that we are testing will show its superiority when the data is sufficiently precise. The improved accuracy of the modified version becomes crucial in the context of extrapolation of relatively low density data to extreme densities. It thus becomes necessary to generate many more instances of high precision data for speed of elastic waves in extreme conditions so that the modified version of the Birch's law may be subjected to more extensive testing. Presently this type of high precision data can be generated only with density-functional-theory-based calculations. It is to such calculations that we devote the next two chapters. Chapter 5 deals only with zero temperature calculations done by us whereas chapter 6 is about finite temperature calculations.

Chapter 5

Ab initio calculations at zero temperature

5.1 Introduction

In this chapter we present the results of our analysis of elastic wave speed at zero temperature in some elemental solids. We generated the data analysed here by using the density functional theory (DFT) of electronic structure calculation. We have done these calculations for a large number of elemental solids so that the validity of the modified version of the Birch's law can be tested on a large data set. The choice of materials has been dictated primarily by the following two considerations: (i) The stability of a particular crystalline form over a large range of pressures (typically from 15 to 360 GPa). This is essential since the scaling law of the phonon dispersion relation will not hold good in the entire pressure range if there is a structural phase transition in this region. The modified version of the Birch's law is based on the assumption of validity of this scaling law. If this breaks down we certainly cannot expect the modified version to work. And we need to work in a large range of pressures because unless the elastic wave speed can be computed over a large enough range of densities it is not possible to discriminate between the two versions of the Birch's law (Note: Over a narrow enough range of densities the modified form will effectively be indistinguishable from the original one). (ii) Our previous experience [52] of working with some of these materials for the study of the scaling law.

5.2 Methodology

Section 2.2.4 provides a complete description of the computational objectives and the procedure. For the purposes of this chapter it can be summarized as follows: (i) Calculate the equilibrium unit cell structure at the pressure of interest. (ii) Calculate the ground state electronic energy for various applied distortions [Note: In principle, free energy at zero temperature also has a contribution from the zero-point quantum fluctuation of the lattice. However, we checked in some cases that this is small enough to be ignored. Due to this reason, for zero temperature calculations, we ignored phonons altogether.]

In the first step we minimize, using the QE software, the enthalpy per unit cell. This minimization is done with respect to the lattice parameters and also (when more than one atom is present within the unit cell) the relative position vectors of the atoms within the unit cell. In the second step the electronic ground state energy is calculated for various types of distortions of the unit cell (after optimizing the positions of the atoms within the unit cell in case more than one atom is present). Each of these distortions create a crystalline solid with a new unit cell geometry. As a result all calculations actually are for a periodic lattice with a small unit cell. This makes calculations for a large number of materials feasible even with modest computational resources.

The elastic constant were calculated with the help of the ElaStic software [46]. However, all the calculations by the software involving the fitting of energy against the amplitude of distortion were cross-checked by us manually for consistency. After the elastic constants are calculated (Note: At zero temperature isothermal and adiabatic elastic constants are identical), we calculate the direction-averaged value of the speed of longitudinal acoustic waves. This is ideally what we might measure for the longitudinal wave speed through an inelastic scattering experiment for a poly-crystalline sample if the grains are truly randomly oriented (see [71] for a more careful analysis). We also calculate the aggregate P-wave speed for a polycrystalline material. It should be remembered that the direction-averaged value of the longitudinal acoustic waves is not quite the same as the P-wave speed – although they are very close.

We have used the Projector-Augmented-Wave (PAW) method for doing our DFT-based calculations. However, in many cases we have repeated the calculation with pseudo-potential based calculations to see if there is any qualitative difference. In all cases first of all convergence with respect to the cut-off energy and the **k**-grid in the first Brillouin zone was checked for the energy per unit cell at a selected set of pressures through the full range upto 360 GPa. The targeted level of convergence was around 1 meV. As a result the energy cut-offs and the **k**-grid resolutions used by us are quite high. We first of all find out the values of the energy cut-off and the **k**-grid resolution that are required, at each of the selected pressures, to achieve the desired convergence. Then, for the production runs, the maximum values (across all pressures) of these parameters are used for calculations at *all* the pressures. Due to these high energy cut-offs the Pulay stress is quite low [72] and is estimated to be of the order of 0.05 GPa. In tables 5.1 and 5.2 we present the values of the most important parameters for all the DFT-based calculations (Note: In these two tables the unit of energy is Rydberg – abbreviated as Ry).

All DFT-based calculations make certain choices and/or approximations whose effect on the final outcome are rarely analyzable on a first principles basis. As a result it is a standard practice to compare, whenever possible, computational outcomes with laboratory experiments. We have also done such comparisons, both for lattice constants and elastic constants, with experimental data or previous computational results – whenever we could find such data [73-102]. We found that disagreement between our calculated values of lattice parameters and experimental values was always less than two percent – usually much less.

Table 5.1: DFT-parameters for the calculation of the elastic constants with pseudopotentials.

System	Energy cut-off (Ry)	**k**-mesh	E_{xc} type	Pseudo potential file	Library
Cu	70	$24\times24\times24$	GGA	Cu.pbe-n-van_ak.UPF	Quantum
Ir	180	$20\times20\times20$	LDA	Ir.pz-sp-hgh.UPF	Espresso
Ni	120	$24\times24\times24$	GGA	Ni.pbe-nd-rrkjus.UPF	
Pd	80	$28\times28\times28$	LDA	Pd.pz-n-rrkjus_psl.0.2.2.UPF	
Hcp-Fe	50	$21\times21\times21$	GGA	Fe.pw91-sp-van_ak.UPF	
Os	70	$24\times24\times20$	LDA	Os.pw-mt_fhi.UPF	
Re	80	$16\times16\times12$	GGA	Re.pw91-n-van.UPF	

Table 5.2: DFT-parameters for the calculation of the elastic constants using the PAW method.

System	Energy cut-off (Ry)	**k**-mesh	E_{xc} type	PAW dataset	Library
Cu	180	$24\times24\times24$	GGA	Cu.pbe-kjpaw.UPF	Quantum
Ir	140	$24\times24\times24$	GGA	Ir.pbesol-n-kjpaw_psl.0.2.3.UPF	Espresso
Ni	80	$24\times24\times24$	GGA	Ni.pbesol-n-kjpaw_psl.0.1.UPF	
Pd	80	$24\times24\times24$	GGA	Pd.pbesol-n-kjpaw_psl.0.2.2.UPF	
Pt	70	$28\times28\times28$	GGA	Pt.pbesol-n-kjpaw_psl.0.1.UPF	
Rh	130	$24\times24\times24$	GGA	Rh.pbesol-spn-kjpaw_psl.0.2.3.UPF	
Mo	80	$24\times24\times24$	GGA	Mo.pbesol-spn-kjpaw_psl.0.2.UPF	
Hcp-Fe	140	$18\times18\times12$	GGA	Fe.pbesol-spn-kjpaw_psl.0.2.1.UPF	
Os	70	$24\times24\times18$	GGA	Os.pbesol-n-kjpaw_psl.0.2.3.UPF	Standard Solid-State
Re	80	$16\times16\times12$	GGA	Re.pbesol-spn-kjpaw_psl.0.3.1.UPF	Pseudo-Potential

5.3 Results

We have studied ten elemental solids. Of these nickel, iridium, palladium, platinum, rhodium and copper have face-centered-cubic (fcc) lattice, molybdenum has a body-centered-cubic (bcc) lattice and iron, rhenium and osmium have hexagonal-close-packed lattice in the range of pressure of interest (roughly from 15 GPa to 360 GPa – partly to avoid the region of bcc to hcp transition of iron, the most important element from the point of view of actual application in terrestrial geophysics). Also while nickel is magnetic, hcp-iron is non-magnetic in this range of pressures [103-106].

After calculating the equilibrium geometry of the unit cell for the applied pressure different kinds of distortions, as explained in section 2.2.4, are applied. Through an analysis of the energies for these distorted states, the single crystal elastic constants are computed. Since these are zero temperature calculations isothermal and adiabatic elastic constants are identical. In tables 5.3 through 5.15 we tabulate the single crystal Birch coefficients (see section 2.2.7 for the relationship between the Birch coefficients and the elastic constants). In every case data is collected in the range of 0 to 360 GPa with a uniform spacing of 30 GPa.

Table 5.3: Birch coefficients of non-magnetic hcp-iron at various densities: PAW method.

ρ (Kg/m^3)	B_{11} (GPa)	B_{12} (GPa)	B_{13} (GPa)	B_{33} (GPa)	B_{44} (GPa)
9409.5	598.5	195.9	164.5	675.8	188.4
10167.4	799.4	300.0	252.1	897.2	235.2
10776.9	983.2	398.0	334.9	1106.2	275.4
11298.1	1155.6	488.0	418.4	1296.3	314.2
11759.2	1320.4	587.4	494.5	1476.7	349.8
12176.2	1479.3	670.7	575.7	1653.8	382.8
12558.5	1633.4	765.5	650.6	1816.6	416.8
12912.5	1783.8	854.6	725.8	1980.1	448.5
13246.3	1932.1	940.8	801.9	2141.8	479.1
13559.6	2076.9	1027.9	875.8	2299.6	509.9
13856.8	2221.6	1109.6	950.9	2453.4	538.6
14139.8	2361.9	1199.1	1022.9	2602.5	567.4
14410.0	2503.4	1277.7	1097.1	2753.1	595.5

Table 5.4: Birch coefficients of non-magnetic hcp-iron at various densities: Pseudo-potential method.

ρ (Kg/m^3)	B_{11} (GPa)	B_{12} (GPa)	B_{13} (GPa)	B_{33} (GPa)	B_{44} (GPa)
9105.9	534.8	173.7	149.1	599.7	168.3
9913.9	737.4	277.3	236.4	821.4	215.7
10552.1	921.4	375.8	319.8	1022.5	256.8
11092.4	1093.4	470.9	400.9	1212.7	295.0
11567.5	1257.6	563.2	480.2	1393.5	330.3
11995.2	1416.4	654.2	557.9	1567.7	364.9
12386.4	1571.1	740.7	635.4	1736.0	397.1
12748.7	1722.5	828.5	711.3	1898.5	429.1
13090.6	1872.7	913.1	788.6	2065.8	460.7
13405.8	2017.9	995.8	863.6	2220.2	491.0
13706.7	2160.8	1080.1	938.6	2375.1	520.8
13993.1	2303.0	1161.3	1014.2	2528.3	549.9
14268.0	2443.8	1249.1	1086.9	2680.9	578.9

Table 5.5: Birch coefficients of osmium at various densities: PAW method.

ρ (Kg/m^3)	B_{11} (GPa)	B_{12} (GPa)	B_{13} (GPa)	B_{33} (GPa)	B_{44} (GPa)
22649.5	796.0	245.6	246.1	883.1	277.5
24033.0	1013.6	346.6	340.6	1117.2	331.2
25186.8	1212.6	447.2	429.2	1333.8	379.1
26191.1	1400.3	539.6	516.7	1540.5	422.2
27088.8	1578.1	633.2	600.4	1734.4	462.4
27907.9	1749.8	725.3	681.5	1922.8	500.3
28664.9	1913.6	810.3	764.0	2107.3	534.1
29371.1	2074.8	900.7	841.7	2286.0	569.0
30035.4	2231.7	985.6	917.9	2462.8	599.9
30664.4	2385.0	1074.6	992.1	2635.3	629.3
31262.7	2534.6	1173.4	1063.0	2790.1	661.4
31833.9	2683.6	1248.3	1141.0	2952.1	690.4
32375.0	2826.6	1331.3	1216.5	3108.8	718.0

Table 5.6: Birch coefficients of osmium at various densities: Pseudo-potential method.

ρ (Kg/m^3)	B_{11} (GPa)	B_{12} (GPa)	B_{13} (GPa)	B_{33} (GPa)	B_{44} (GPa)
22951.6	841.9	249.4	249.0	934.4	299.7
24306.9	1061.5	349.7	338.8	1169.9	355.8
25444.9	1263.5	446.1	424.5	1387.7	405.8
26440.4	1453.3	540.0	507.5	1593.3	451.6
27331.1	1633.4	631.8	588.5	1788.9	493.9
28153.8	1808.6	722.7	668.9	1979.7	534.6
28907.8	1975.7	812.6	747.7	2162.7	572.7
29609.4	2136.9	901.7	825.5	2339.8	608.4
30269.6	2293.5	990.4	902.6	2512.7	642.8
30898.3	2447.3	1078.6	979.5	2683.4	676.4
31507.5	2602.0	1166.7	1056.9	2855.2	710.1
32068.1	2748.9	1251.7	1131.9	3017.3	740.5
32611.3	2897.1	1336.3	1207.2	3180.2	771.0

Table 5.7: Birch coefficients of rhenium at various densities: PAW method.

ρ (Kg/m^3)	B_{11} (GPa)	B_{12} (GPa)	B_{13} (GPa)	B_{33} (GPa)	B_{44} (GPa)
21314.2	657.5	285.7	232.6	717.4	174.9
22773.6	839.7	398.6	317.1	914.6	214.1
23994.4	1005.5	502.4	397.4	1099.9	247.9
25063.5	1163.8	597.7	475.8	1270.0	278.6
26025.6	1318.7	688.4	552.5	1427.3	308.4
26907.1	1465.1	780.7	626.6	1577.9	336.0
27724.6	1608.6	871.0	698.3	1728.8	362.2
28490.1	1745.6	959.1	767.3	1885.5	387.1
29211.7	1886.1	1040.2	836.1	2044.1	413.0
29895.5	2029.8	1114.8	903.7	2209.2	440.7
30547.0	2173.7	1193.5	968.6	2370.7	469.2
31168.2	2321.2	1264.1	1035.5	2536.9	497.3
31763.7	2470.4	1338.7	1098.6	2700.6	531.4

Table 5.8: Birch coefficients of rhenium at various densities: Pseudo-potential method.

ρ (Kg/m^3)	B_{11} (GPa)	B_{12} (GPa)	B_{13} (GPa)	B_{33} (GPa)	B_{44} (GPa)
21008.2	612.8	269.2	223.6	667.2	162.3
22526.8	793.4	379.9	309.0	865.1	200.0
23791.0	955.1	482.6	388.1	1041.3	232.7
24897.9	1107.3	576.3	464.0	1201.2	261.8
25896.0	1251.5	662.6	538.6	1348.5	288.3
26813.0	1389.8	746.4	609.5	1488.1	312.8
27667.0	1521.8	829.3	676.7	1627.3	335.7
28469.8	1650.6	909.9	740.2	1769.2	358.0
29230.1	1774.3	990.0	802.3	1912.9	380.6
29953.8	1906.6	1058.4	863.7	2056.4	404.5
30645.0	2038.1	1123.4	924.6	2203.6	430.3
31309.0	2172.2	1187.5	983.0	2351.6	457.6
31947.1	2307.7	1247.3	1040.8	2496.2	485.5

Table 5.9: Birch coefficients of magnetic nickel at various densities: PAW and pseudo-potential methods.

PAW				Pseudopotential			
ρ (Kg/m^3)	B_{11} (GPa)	B_{12} (GPa)	B_{44} (GPa)	ρ (Kg/m^3)	B_{11} (GPa)	B_{12} (GPa)	B_{44} (GPa)
9345.6	327.8	185.8	156.0	8915.1	266.7	152.2	126.3
10337.7	495.3	309.2	221.1	10034.2	432.6	271.5	189.6
11081.2	647.4	424.6	279.0	10849.7	574.0	385.3	244.1
11693.3	790.2	535.3	332.4	11513.6	735.6	480.2	296.8
12222.9	926.4	643.3	382.8	12084.1	848.7	592.5	344.9
12693.6	1055.6	749.6	430.2	12590.5	971.5	695.9	391.0
13120.7	1181.2	854.1	475.3	13046.9	1103.1	792.8	438.1
13513.5	1301.7	958.2	518.5	13466.2	1228.5	890.1	481.6
13878.5	1419.2	1060.8	559.7	13854.9	1338.8	992.5	522.2
14220.4	1533.4	1162.9	598.8	14223.5	1456.7	1092.0	566.8
14542.8	1645.6	1264.2	636.7	14559.8	1576.8	1183.6	606.6
14848.5	1754.1	1365.4	672.5	14884.0	1675.4	1288.9	644.1
15139.5	1861.4	1465.6	706.1	15190.8	1780.9	1387.0	680.7

Table 5.10: Birch coefficients of palladium at various densities: PAW and pseudo-potential methods.

PAW				Pseudopotential			
ρ (Kg/m^3)	B_{11} (GPa)	B_{12} (GPa)	B_{44} (GPa)	ρ (Kg/m^3)	B_{11} (GPa)	B_{12} (GPa)	B_{44} (GPa)
12073.7	246.7	183.6	81.6	12412.9	273.7	206.8	86.1
13461.4	418.9	326.6	133.3	13716.1	443.6	350.5	136.5
14449.9	573.6	456.0	178.4	14666.7	603.3	479.6	181.4
15247.5	717.9	579.0	219.5	15439.0	750.3	602.9	223.5
15929.4	856.5	697.6	258.2	16102.4	892.5	723.2	263.3
16530.0	990.4	812.5	296.1	16688.2	1031.4	837.8	302.0
17072.2	1120.0	925.3	332.5	17217.2	1160.0	951.8	338.3
17568.1	1246.4	1036.0	367.8	17702.7	1293.6	1060.5	374.3
18027.6	1371.4	1144.9	402.5	18152.6	1419.8	1170.8	408.7
18456.8	1493.5	1252.5	436.5	18573.2	1542.5	1278.9	442.8
18859.7	1613.3	1358.6	469.5	18979.5	1669.7	1387.1	477.6
19252.1	1735.5	1466.2	503.9	19343.7	1787.3	1491.2	509.5
19603.9	1848.4	1568.0	534.1	19699.8	1904.4	1598.2	540.4

Table 5.11: Birch coefficients of iridium at various densities: PAW and pseudopotential methods.

PAW				Pseudopotential			
ρ (Kg/m^3)	B_{11} (GPa)	B_{12} (GPa)	B_{44} (GPa)	ρ (Kg/m^3)	B_{11} (GPa)	B_{12} (GPa)	B_{44} (GPa)
22492.8	645.9	261.6	281.2	22896.9	682.4	272.0	295.5
24008.0	843.6	382.6	360.0	24378.9	878.6	390.1	376.1
25234.3	1023.1	497.2	431.0	25593.6	1059.3	501.8	449.9
26285.2	1191.7	607.3	496.7	26634.8	1227.6	610.2	517.6
27214.0	1352.8	713.9	559.1	27567.7	1390.6	715.2	583.5
28053.7	1507.1	818.1	618.5	28400.1	1543.2	817.2	644.2
28824.9	1657.6	920.2	675.8	29172.8	1691.8	918.7	703.4
29540.9	1804.4	1020.3	731.3	29900.8	1841.6	1018.4	762.4
30210.8	1947.3	1119.0	784.8	30578.4	1979.8	1120.2	818.9
30842.1	2087.6	1216.2	837.3	31201.1	2118.7	1214.9	871.4
31440.7	2225.0	1312.5	888.0	31808.2	2255.1	1313.0	925.0
32010.4	2360.3	1407.7	937.9	32392.6	2390.3	1411.0	977.8
32556.0	2493.1	1502.8	986.8	32923.9	2515.8	1503.9	1025.3

Table 5.12: Birch coefficients of copper at various densities: PAW and pseudopotential methods.

PAW				Pseudopotential			
ρ (Kg/m^3)	B_{11} (GPa)	B_{12} (GPa)	B_{44} (GPa)	ρ (Kg/m^3)	B_{11} (GPa)	B_{12} (GPa)	B_{44} (GPa)
8627.9	171.1	117.6	80.2	8821.7	176.9	122.6	82.0
10031.4	330.4	248.3	141.2	10222.1	331.6	251.3	139.5
10967.1	474.8	367.4	191.1	11173.1	472.6	367.9	186.5
11703.8	610.1	482.3	236.1	11926.0	607.0	479.0	230.0
12322.3	743.1	594.7	280.8	12562.0	736.0	586.9	271.8
12860.9	874.6	702.7	323.1	13118.6	860.2	692.3	312.4
13346.7	1003.8	808.6	364.1	13618.9	981.5	797.0	352.4
13781.2	1121.1	917.5	404.1	14074.6	1101.6	899.4	391.6
14184.2	1249.2	1021.2	444.7	14494.5	1216.5	1002.1	430.0
14558.2	1386.4	1120.2	486.0	14890.8	1332.4	1104.7	468.6
14906.2	1492.3	1232.9	529.1	15253.4	1442.8	1204.8	505.0
15237.7	1620.4	1333.4	565.1	15600.0	1553.9	1305.3	541.3
15548.8	1748.0	1430.5	602.6	15928.7	1664.0	1405.1	577.1

Table 5.13: Birch coefficients of platinum at various densities: PAW method.

ρ (Kg/m^3)	B_{11} (GPa)	B_{12} (GPa)	B_{44} (GPa)
21245.6	355.5	253.3	80.9
23089.9	538.2	394.1	131.8
24486.6	703.3	524.5	178.8
25645.0	858.7	648.8	223.5
26647.0	1006.7	768.7	266.3
27538.0	1149.4	885.1	307.6
28351.7	1289.0	999.5	348.2
29098.4	1424.8	1111.8	387.7
29797.0	1559.0	1222.9	426.8
30441.3	1688.4	1331.4	464.1
31052.5	1816.6	1439.1	501.2
31632.6	1943.3	1545.8	537.8
32184.6	2067.9	1651.7	573.8

Table 5.14: Birch coefficients of rhodium at various densities: PAW method.

ρ (Kg/m^3)	B_{11} (GPa)	B_{12} (GPa)	B_{44} (GPa)
12492.7	468.7	207.7	211.4
13565.5	660.8	331.1	289.1
14394.0	833.9	446.1	357.6
15087.9	995.9	556.4	420.8
15692.8	1150.2	663.3	480.4
16235.2	1299.2	767.7	537.4
16728.0	1442.9	870.0	592.0
17183.3	1583.4	970.7	645.0
17607.7	1720.7	1070.2	696.4
18005.7	1855.2	1168.4	746.3
18390.0	1990.8	1267.3	797.1
18744.7	2119.7	1363.5	844.2
19079.3	2244.2	1458.5	889.4

Table 5.15: Birch coefficients of molybdenum at various densities: PAW method.

ρ (Kg/m^3)	B_{11} (GPa)	B_{12} (GPa)	B_{44} (GPa)
10278.2	490.5	175.7	106.4
11231.4	659.3	272.0	145.1
11997.0	811.7	363.1	181.4
12652.1	953.9	450.4	213.9
13234.3	1081.0	535.3	243.2
13764.7	1199.1	618.9	274.2
14253.9	1323.1	702.7	313.3
14707.4	1440.0	792.3	350.4
15131.0	1562.6	875.6	393.4
15530.3	1662.3	967.2	422.1
15909.4	1764.6	1055.6	446.0
16270.0	1867.0	1144.7	468.6
16615.3	1958.5	1231.7	487.1

Once the single crystal elastic constants are known we calculate the direction-averaged value of the longitudinal acoustic wave speed as well as the polycrystalline aggregate elastic constants (bulk modulus and shear modulus) using the methods described in section 2.3. The computed value of the P-wave speed depends on the averaging scheme employed to calculate the elastic moduli of the aggregate. For hcp materials the Voigt and Reuss schemes provide the two limits [43] of the elastic moduli. For the cubic materials the bounds suggested by Hashin and Shtrikman [44] are used. The two speeds calculated using these two limits are taken as the two limits of the region of uncertainty for V_P. Half of the width of this region of uncertainty can be thought of as the (definitional) error bar in the calculation of the P-wave speed. However, these error bars are too small to be shown directly in any graph where the elastic wave speed (alone or multiplied by some factor) is one of the two variables plotted.

We now proceed to the comparison of the hypotheses H1 and H2 in the light the data just presented. In some of the cases (palladium, platinum, rhodium, nickel, iridium and hcp-iron), data for which are presented in figures 5.1 through 5.12 (only for V_P, not for $< V_{LA} >$), even visually it is clear that the modified

Birch's law works better. For each of these elements we present the plot of the P-wave speed (V_P) vs. the density (ρ). The best linear fit is also shown as a continuous line. The dashed line in each case is the best quadratic fit and passes essentially through every data point. Visual comparison of this with the best fit straight line shows emphatically that the best linear fit is actually not so good. The plots of $V_P\rho^{1/3}$ vs. ρ , on the other hand, show that the best fit straight line passes through the data points. For each case comparison of the two plots makes it evident that the product $V_P\rho^{1/3}$ gives a better linear fit than V_P alone.

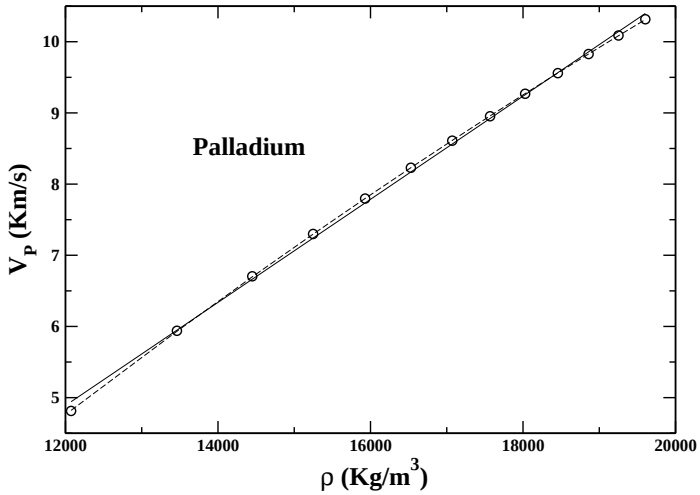

Figure 5.1: P-wave speed V_P against density (ρ) for palladium (PAW method).

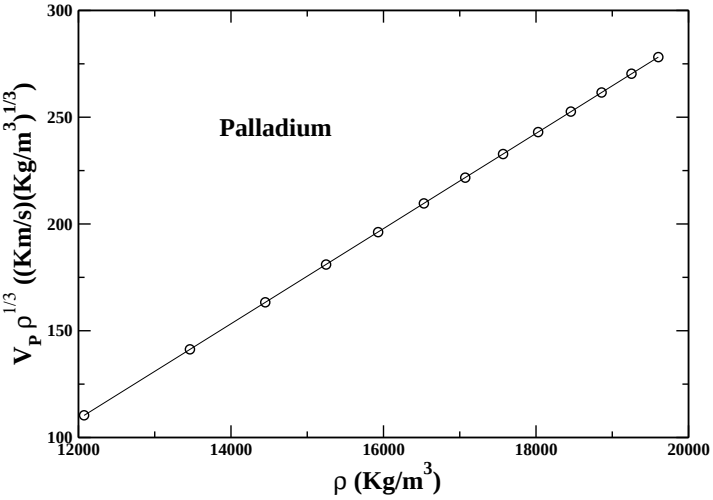

Figure 5.2: $V_P \rho^{1/3}$ against density (ρ) for palladium (PAW method).

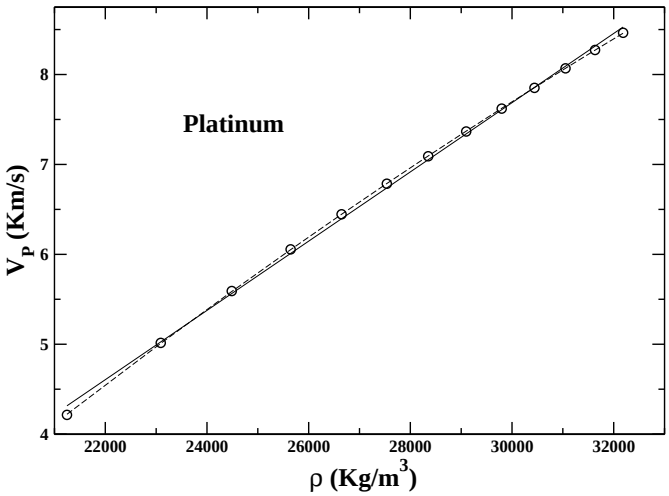

Figure 5.3: P-wave speed V_P against density (ρ) for platinum (PAW method).

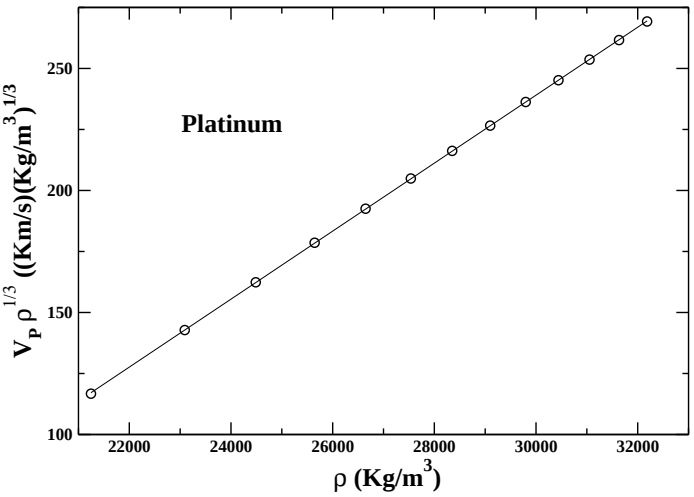

Figure 5.4: $V_P\rho^{1/3}$ against density (ρ) for platinum (PAW method).

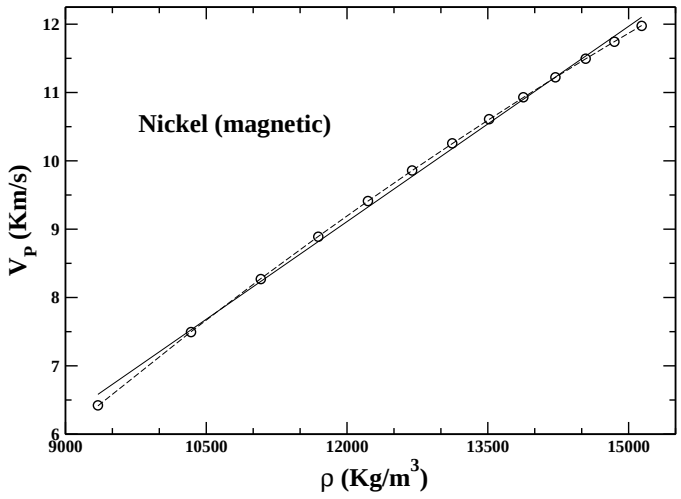

Figure 5.5: P-wave speed V_P against density (ρ) for nickel (PAW method).

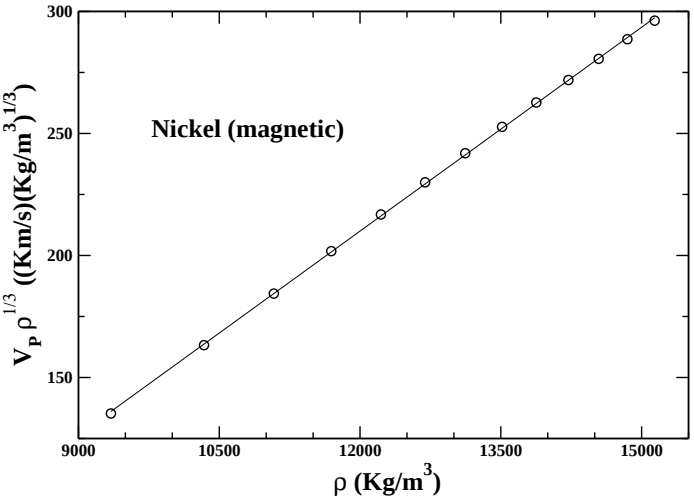

Figure 5.6: $V_P\rho^{1/3}$ against density (ρ) for nickel (PAW method).

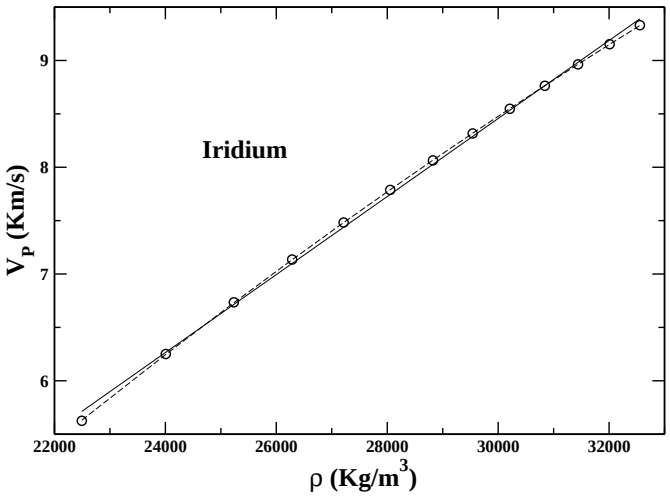

Figure 5.7: P-wave speed V_P against density (ρ) for iridium (PAW method).

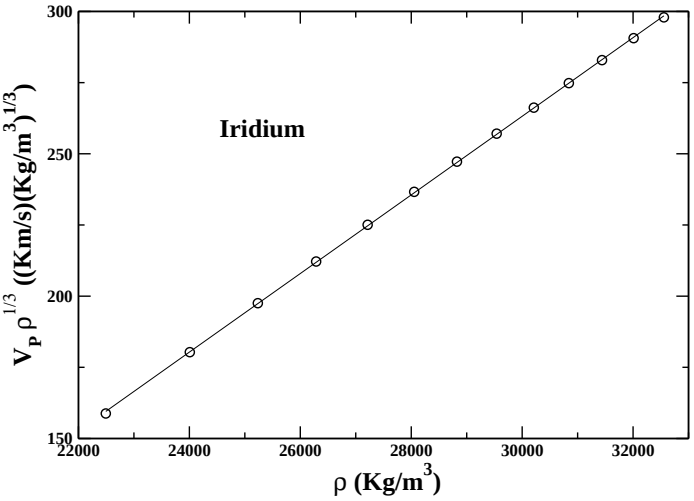

Figure 5.8: $V_P\rho^{1/3}$ against density (ρ) for iridium (PAW method).

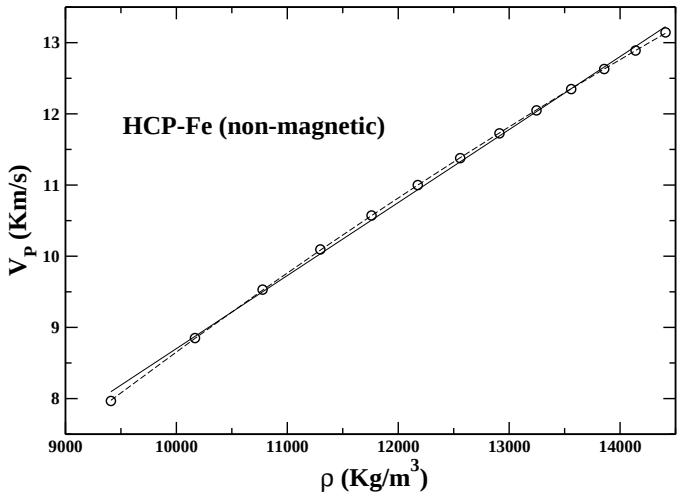

Figure 5.9: P-wave speed V_P against density (ρ) for hcp-iron (PAW method).

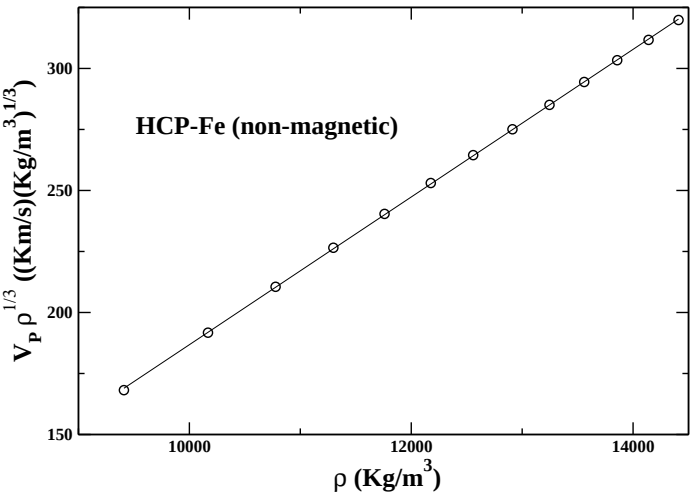

Figure 5.10: $V_P\rho^{1/3}$ against density (ρ) for hcp-iron (PAW method).

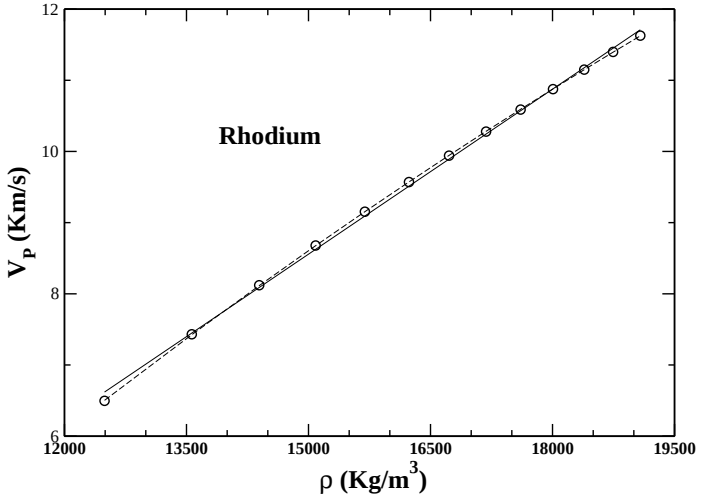

Figure 5.11: P-wave speed V_P against density (ρ) for rhodium (PAW method).

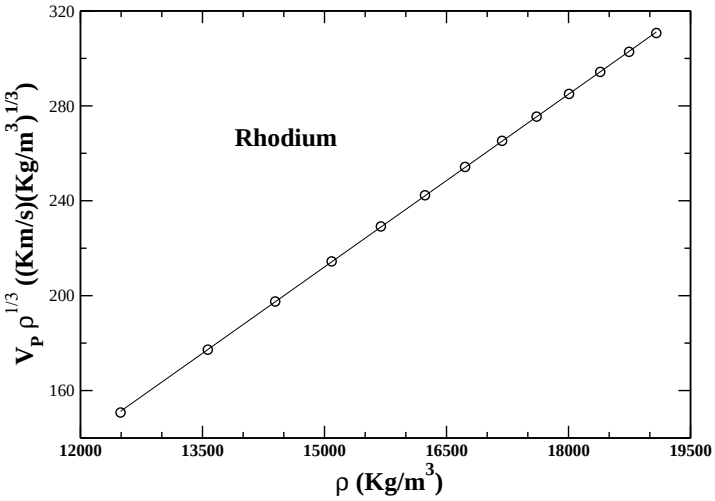

Figure 5.12: $V_P\rho^{1/3}$ against density (ρ) for rhodium (PAW method).

The values of our chosen metrics for goodness of linear fit are shown in tables 5.16 and 5.17 [Note: In every case the lowest density data point corresponds to zero pressure and this is excluded from the calculation of the metrics f_{max} and f_{mean}]. For both $< V_{LA} >$ and V_P, it can be seen that the metric for the modified Birch's law is smaller than that for the original version by a factor that ranges between 2 and (about) 20 [Note: The only exception is the PAW calculation for copper]. And hence the modified version clearly works better.

Table 5.16: Data for maximum fractional deviation

System	Method	Maximum fractional deviation				Maximum fractional uncertainty for V_P
		$< V_{LA} >$		V_P		
		$V-\rho$	$V\rho^{1/3}-\rho$	$V-\rho$	$V\rho^{1/3}-\rho$	
Ni	PP	1.8×10^{-2}	5.0×10^{-3}	2.0×10^{-2}	9.3×10^{-3}	5.9×10^{-3}
	PAW	2.2×10^{-2}	5.2×10^{-3}	2.5×10^{-2}	7.4×10^{-3}	6.3×10^{-3}
Ir	PP	2.0×10^{-2}	5.3×10^{-3}	2.0×10^{-2}	5.8×10^{-3}	1.5×10^{-3}
	PAW	1.8×10^{-2}	3.9×10^{-3}	1.8×10^{-2}	3.8×10^{-3}	1.4×10^{-3}
Pd	PP	1.7×10^{-2}	9.6×10^{-4}	1.8×10^{-2}	1.8×10^{-3}	4.9×10^{-3}
	PAW	2.2×10^{-2}	1.0×10^{-3}	1.7×10^{-2}	5.0×10^{-4}	5.7×10^{-3}
Pt	PP[73]	1.7×10^{-2}	3.5×10^{-3}	1.8×10^{-2}	4.0×10^{-3}	3.2×10^{-3}
	PAW	1.7×10^{-2}	9.7×10^{-4}	1.7×10^{-2}	1.6×10^{-3}	2.8×10^{-3}
Rh	PAW	1.8×10^{-2}	2.2×10^{-3}	1.8×10^{-2}	2.3×10^{-3}	2.2×10^{-3}
Cu	PP	1.1×10^{-2}	7.0×10^{-3}	1.4×10^{-2}	4.7×10^{-3}	8.5×10^{-3}
	PAW	2.6×10^{-3}	1.4×10^{-2}	5.3×10^{-3}	1.4×10^{-2}	7.5×10^{-3}
Mo	PAW	2.9×10^{-2}	1.4×10^{-2}	3.2×10^{-2}	1.6×10^{-2}	1.0×10^{-4}
Hcp-Fe	PP	1.8×10^{-2}	1.9×10^{-3}	1.7×10^{-2}	1.4×10^{-3}	1.3×10^{-3}
	PAW	2.0×10^{-2}	4.5×10^{-3}	2.0×10^{-2}	3.9×10^{-3}	1.5×10^{-3}
Re	PP	3.1×10^{-2}	1.3×10^{-2}	3.0×10^{-2}	1.2×10^{-2}	1.9×10^{-3}
	PAW	1.4×10^{-2}	9.7×10^{-3}	1.4×10^{-2}	1.0×10^{-2}	2.0×10^{-3}
Os	PP	2.4×10^{-2}	8.8×10^{-3}	2.3×10^{-2}	8.6×10^{-3}	7.7×10^{-4}
	PAW	2.5×10^{-2}	9.6×10^{-3}	2.5×10^{-2}	9.4×10^{-3}	8.8×10^{-4}

Table 5.17: Data for mean fractional deviation

System	Method	$< V_{LA} >$		V_P	
		$V-\rho$	$V\rho^{1/3}-\rho$	$V-\rho$	$V\rho^{1/3}-\rho$
Ni	PP	7.9×10^{-3}	1.7×10^{-3}	1.0×10^{-2}	3.3×10^{-3}
	PAW	1.0×10^{-2}	2.5×10^{-3}	1.1×10^{-2}	3.6×10^{-3}
Ir	PP	8.4×10^{-3}	2.2×10^{-3}	8.8×10^{-3}	2.6×10^{-3}
	PAW	7.8×10^{-3}	1.7×10^{-3}	7.8×10^{-3}	1.7×10^{-3}
Pd	PP	7.1×10^{-3}	3.5×10^{-4}	7.5×10^{-3}	7.0×10^{-4}
	PAW	8.1×10^{-3}	4.6×10^{-4}	6.8×10^{-3}	2.6×10^{-4}
Pt	PP[73]	9.9×10^{-3}	2.0×10^{-3}	1.0×10^{-2}	2.2×10^{-3}
	PAW	6.9×10^{-3}	3.4×10^{-4}	7.2×10^{-3}	6.3×10^{-4}
Rh	PAW	7.4×10^{-3}	8.6×10^{-4}	7.5×10^{-3}	9.8×10^{-4}
Cu	PP	4.5×10^{-3}	2.8×10^{-3}	6.2×10^{-3}	1.6×10^{-3}
	PAW	1.3×10^{-3}	6.4×10^{-3}	2.1×10^{-3}	6.7×10^{-3}
Mo	PAW	1.2×10^{-2}	5.0×10^{-3}	1.3×10^{-2}	5.7×10^{-3}
Hcp-Fe	PP	7.3×10^{-3}	7.4×10^{-4}	6.9×10^{-3}	4.6×10^{-4}
	PAW	8.3×10^{-3}	1.8×10^{-3}	7.9×10^{-3}	1.4×10^{-3}
Re	PP	1.1×10^{-2}	4.5×10^{-3}	1.1×10^{-2}	4.6×10^{-3}
	PAW	5.3×10^{-3}	3.8×10^{-3}	5.3×10^{-3}	3.8×10^{-3}
Os	PP	1.0×10^{-2}	3.8×10^{-3}	9.9×10^{-3}	3.6×10^{-3}
	PAW	1.1×10^{-2}	4.5×10^{-3}	1.1×10^{-2}	4.4×10^{-3}

While comparing the metrics in tables 5.16 and 5.17 it should be kept in mind that the value of V_P has some definitional uncertainty. And, while these definitional errors may be too small to be meaningfully shown in the figures directly, their values must be kept in mind while coming to any conclusion regarding the relative merits of the two competing hypotheses – so as to have a proper perspective of how seriously should the metrics be taken. It is due to this reason that we have also shown the values of these definitional error bars in the last column of table 5.16 (these error bars are explained in section 2.3). Each row shows the *maximum* value of the error bar across all pressures for that particular element and for that particular method of calculation (PP or PAW). The *typical* value of the error bar would be considerably less. It can be seen that these error bars are never so high as to bring into question the validity of our analysis and the conclusions drawn therefrom.

Chapter 6

Ab initio calculations at finite temperature

6.1 Introduction

In this chapter we continue our tests of Birch's law but now at finite temperatures. In chapter 5 we carried out the tests at zero temperature and found that the modified version of the Birch's law consistently gives a better agreement with data than the original version. But few experiments are done at temperatures close to zero. Due to the very difficult challenges involved in ultra-high pressure experiments vast majority of the experiments are done at the room temperature. A relatively small number of experiments have been performed at elevated temperatures. For hcp-iron the highest temperature at which this type of experiment has been performed is around 3000 K – according to our survey of the literature. So we need to ask the question: does the modified Birch's law, which seems to give superior agreement with high precision data computed at $T = 0$, continue to be equally accurate at higher temperatures? While the ultimate test of the relative superiority of the two versions of the Birch's law would be in the realm of data from laboratory experiments, at the present time such data are not available at a level of precision that is required to discriminate between the two hypotheses (In fact, except for iron, we are not aware of any system for which elastic wave speed data is available as a function of density at multiple values of the temperature). The next best option is to continue the *ab initio* calculations based on the density

functional theory into the domain of finite temperatures. Finite value of the temperature immediately makes the calculations a lot more resource intensive. This is partially due to the fact that now phonons also contribute to the free energy and hence the phonon spectrum also has to be calculated. Thus the number of systems we have studied at finite temperatures is less than that in the case of zero temperature. Choice of systems was dictated by the criterion of phase stability upto pressures exceeding 360 GPa and, whenever available, by the existence of some previous work that can serve benchmarking purposes [107-120]. Study of hexagonal-close-packed systems is a lot more (computationally) demanding than it is for cubic systems. Hence we have studied only hcp-iron from this family. This is due to the obvious geophysical interest in it. The remaining elements studied are all of the cubic type. These elements are: platinum, molybdenum, palladium and rhodium.

6.2 Methodology

The methodology used in these finite temperature calculations has already been described fairly comprehensively in chapter 2. Here we just summarize some of the key points. For the zero temperature calculations of chapter 5 we pre-selected a set of values for the applied *pressure*. But now our goal is to calculate the elastic speed at a pre-selected set of *densities* at each temperature chosen. First we have to calculate the reference state around which the elastic wave propagates. Since the cubic crystals have only one lattice parameter the selected value of the density immediately fixes the value of this lattice constant. For the hcp-case the density merely fixes the product a^2c – not a and c individually. What we do to fix the value of a (or c) is to choose the combination of a and c that minimizes the Helmhotz free energy per unit cell – given a particular value of the product a^2c. It turns out that the stress tensor is almost hydrostatic even in the case of hcp-iron – and increasingly so at higher densities. To calculate the isothermal elastic constants we apply specific types of distortions of varying amplitude. In each case, for the given unit cell, the electronic ground state energy as well as the full electronic excitation spectrum is calculated by using the Quantum Espresso (QE) software package. In addition the phonon spectrum is also calculated. We adjust

the resolution of the **k**-grid and the **q**-grid (the latter defines the phonon wave vectors for which the phonon frequencies are calculated by using the density-functional-perturbation theory – as implemented in the QE software package) so as to achieve a convergence level of 1 meV in the calculation of the free energy per unit cell [The most important parameters of the DFT calculations are summarized in the table 6.1].

Table 6.1: DFT-parameters for the calculation of the elastic constants with the PAW method.

System	Energy cut-off (Ry)	**k**-mesh	**q**-mesh	PAW dataset	Library
Pd	80	24×24×24	4×4×4	Pd.pbesol-n-kjpaw_*psl*.0.2.2.UPF	Quantum Espresso
Pt	80	28×28×28	6×6×6	Pt.pbesol-n-kjpaw_*psl*.0.1.UPF	
Rh	130	24×24×24	4×4×4	Rh.pbesol-spn-kjpaw_*psl*.0.2.3.UPF	
Mo	80	24×24×24	6×6×6	Mo.pbesol-spn-kjpaw_*psl*.0.2.UPF	
Hcp-Fe	140	18×18×12	6×6×4	Fe.pbesol-spn-kjpaw_*psl*.0.2.1.UPF	

After this the calculation of the isothermal elastic constants follows the same procedure as in the case of zero temperature. To get the adiabatic elastic constants, which are in general different from the isothermal ones, we need the temperature derivatives of the stress tensor. The procedure used to calculate these is described in the section 2.2.6. It should be kept in mind that our calculation of the free energy makes use of the quasi-harmonic approximation. This means that the amplitudes of vibration of the nuclei in the solid are assumed to be small enough to permit a quantum statistical description of the vibration in terms of a gas of phonons. At higher densities even higher temperatures may reasonably be treated by this approximation. But keeping in mind our ultimate goal of testing

the Birch's law we have limited the value of temperature at all densities to 1500K. This is to ensure that an uniform level of accuracy and physical justifiability may be maintained for the entire range of densities. A final note: Calculations in this chapter use only the Projector-Augmented-Wave (PAW) method since it is generally believed to be the method of choice when high energy densities are involved.

6.3 Results

As before, for a given elemental solid at a given density and temperature, certain types of distortions are applied with varying amplitude. The free energy is calculated for each such distorted configuration. Finally, from an analysis of the dependence of the free energy on the amplitude of distortion the isothermal elastic constants are extracted. Before presenting the values of the isothermal elastic constants we show some illustrative examples of the plot of free energy versus the amplitude of distortion. Figures 6.1, 6.2 and 6.3 show examples of such plots for the three types of distortion in the cubic case (see table 2.1 for a description of these distortions). Similarly, figures 6.4, 6.5, 6.6, 6.7 and 6.8 are for the five types of distortion relevant to the hcp case (see table 2.3 for a description of these distortions).

In each of the eight graphs shown the best fit cubic polynomial is used to calculate the first and second derivatives at $\eta = 0$. For the cubic case the first derivative for two of the distortion types will involve the pressure P and the ratio of these two derivatives should be 3/2 (see table 2.2). This can be tested against the computed data. This provides extremely valuable checks on the consistency and accuracy of our calculations. Similarly (see table 2.4), in the hcp case, there are five first derivatives involving only two unknowns T^{xy} and T^{z}. This redundancy again makes it possible to perform critical quality checks on our computed data. In the tables 6.2 through 6.15 we present the computed values of the isothermal elastic constants as well as all other pieces of information required to calculate the adiabatic elastic constants from these isothermal ones. It may be noted that the temperatures at which the calculations have been done are: 300K, 900K and 1500K for the cubic materials and at 300K and 1500K for hcp-iron.

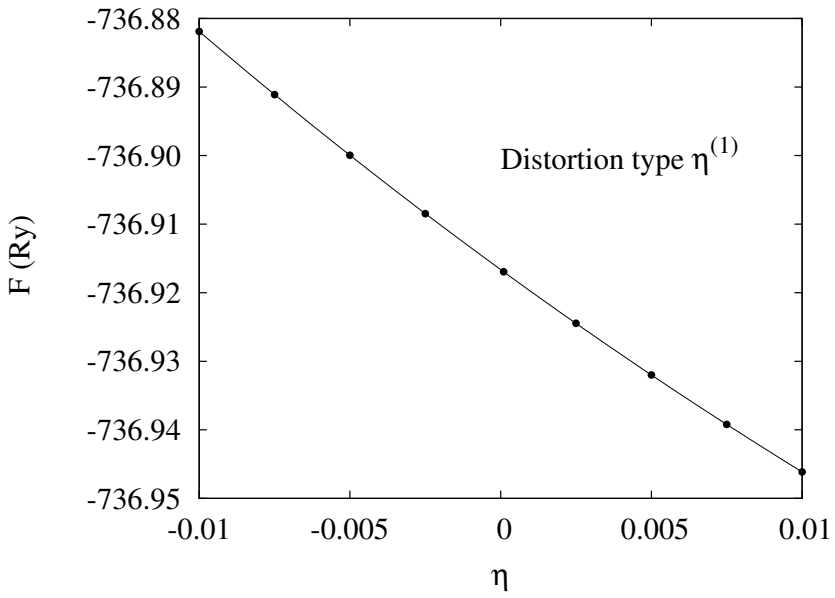

Figure 6.1: Free energy (F) is plotted as a function of the amplitude (η) of distortion for platinum at 300 K (density = $29000Kg/m^3$) – along with the best fit cubic polynomial.

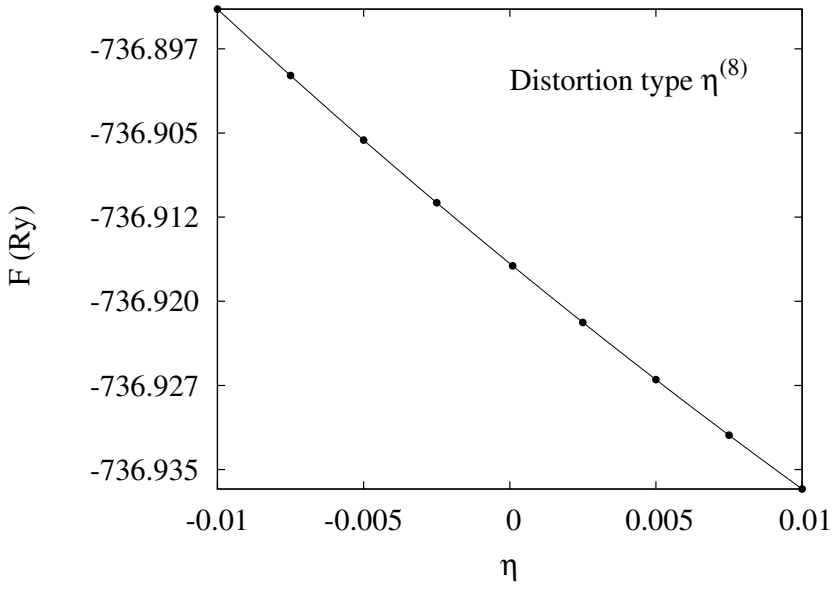

Figure 6.2: Free energy (F) is plotted as a function of the amplitude (η) of distortion for platinum at 300 K (density = $29000Kg/m^3$) – along with the best fit cubic polynomial.

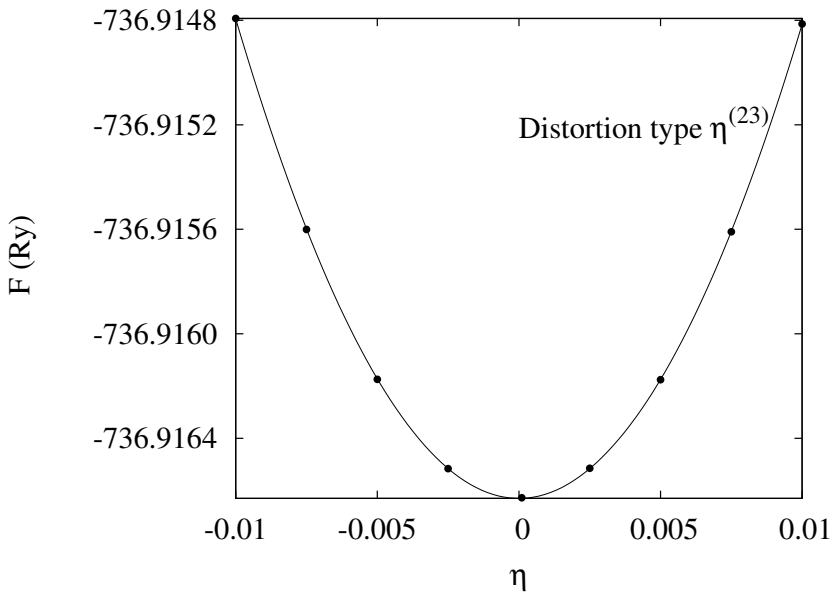

Figure 6.3: Free energy (F) is plotted as a function of the amplitude (η) of distortion for platinum at 300 K (density = $29000Kg/m^3$) – along with the best fit cubic polynomial.

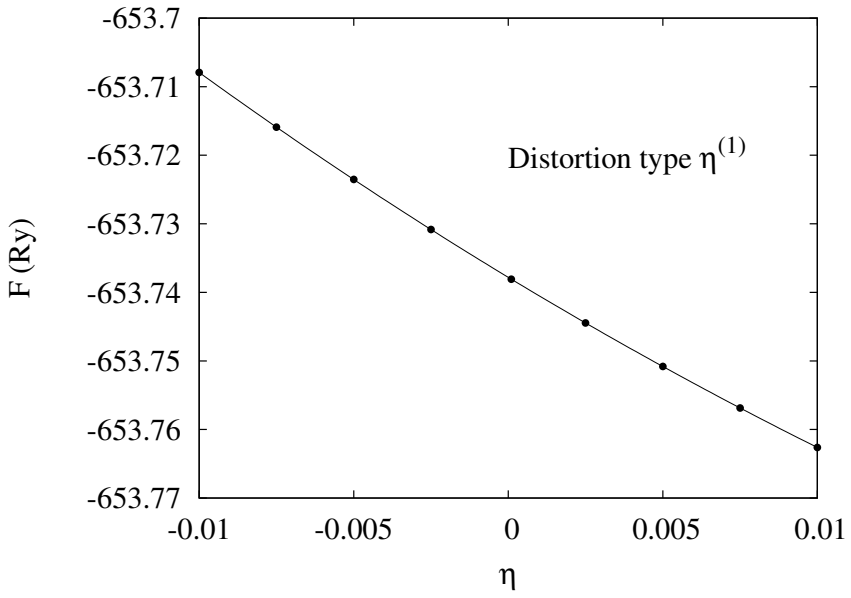

Figure 6.4: Free energy (F) is plotted as a function of the amplitude (η) of distortion for hcp-iron at 300 K (density = $11800Kg/m^3$) – along with the best fit cubic polynomial.

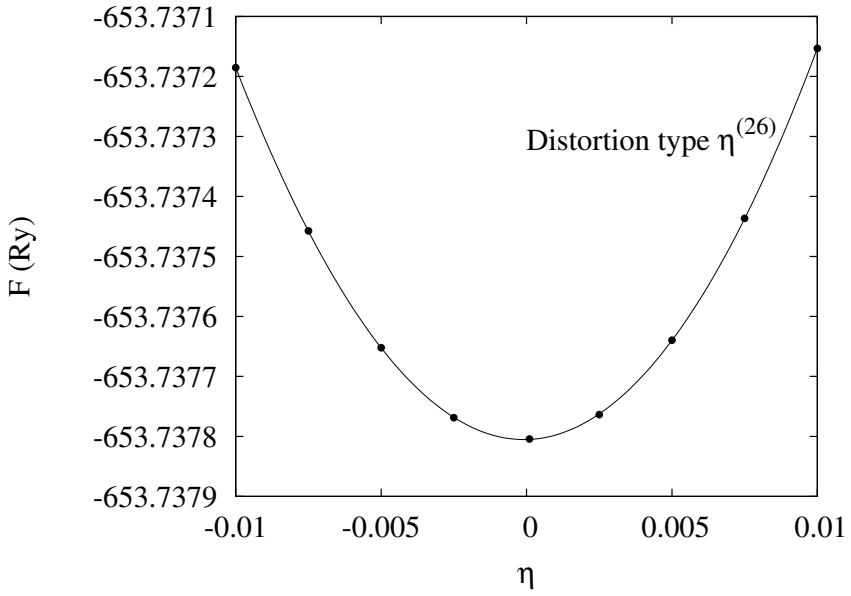

Figure 6.5: Free energy (F) is plotted as a function of the amplitude (η) of distortion for hcp-iron at 300 K (density = $11800Kg/m^3$) – along with the best fit cubic polynomial.

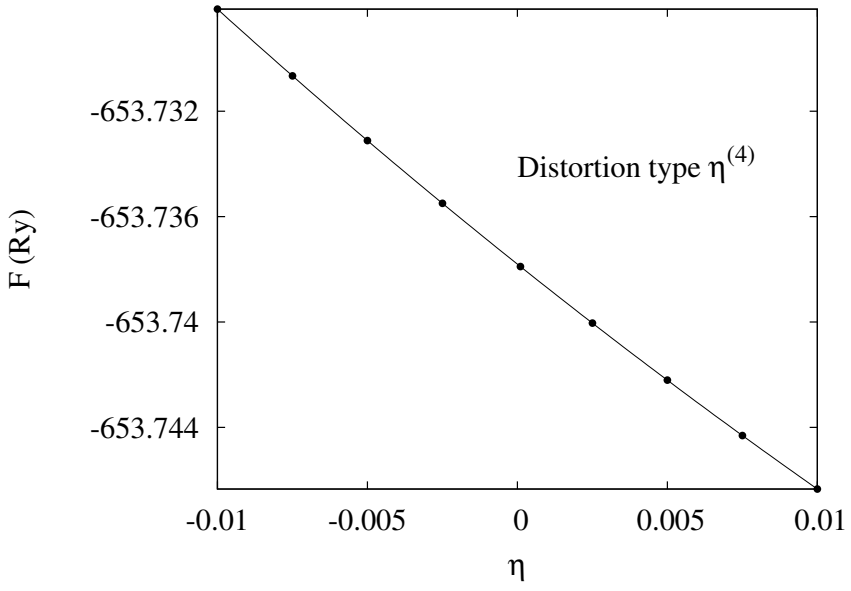

Figure 6.6: Free energy (F) is plotted as a function of the amplitude (η) of distortion for hcp-iron at 300 K (density = $11800Kg/m^3$) – along with the best fit cubic polynomial.

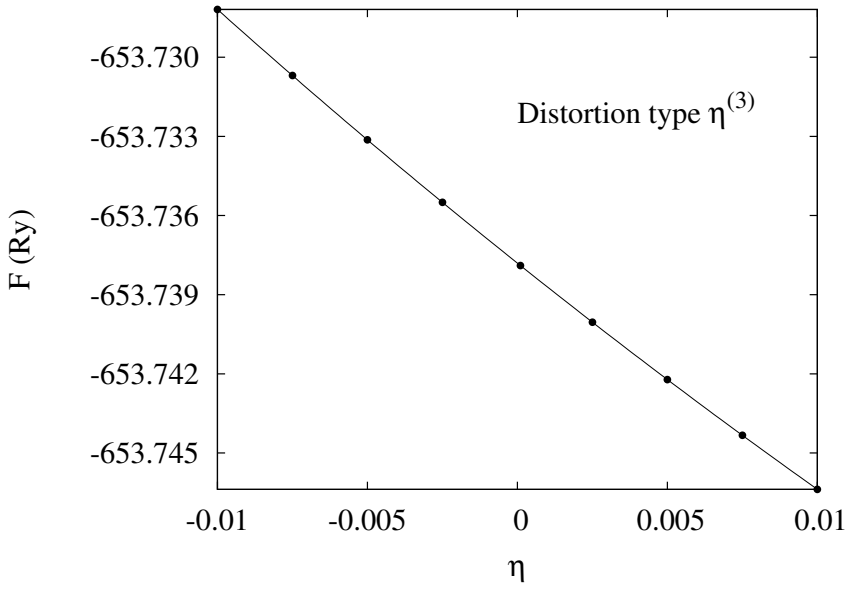

Figure 6.7: Free energy (F) is plotted as a function of the amplitude (η) of distortion for hcp-iron at 300 K (density = $11800Kg/m^3$) – along with the best fit cubic polynomial.

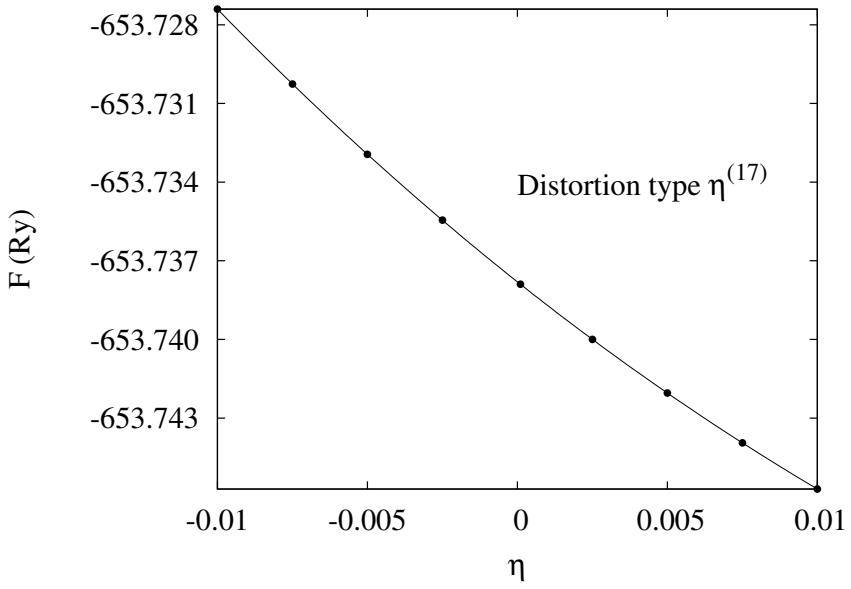

Figure 6.8: Free energy (F) is plotted as a function of the amplitude (η) of distortion for hcp-iron at 300 K (density = $11800Kg/m^3$) – along with the best fit cubic polynomial.

Table 6.2: Isothermal elastic constants and other useful information for palladium at T = 300K.

ρ (Kg/m^3)	C_{11} (GPa)	C_{12} (GPa)	C_{44} (GPa)	P (GPa)	$\frac{dP}{dT} \times 10^3$ $(\frac{GPa}{K})$	$C_v \times 10^4$ $(\frac{eV}{K})$
12600	313.86	223.23	112.06	12.009	6.6053	2.6020
13600	469.59	311.92	175.84	35.949	6.3562	2.5318
14600	664.35	414.44	254.80	67.487	6.1715	2.4573
15600	896.27	534.78	349.06	107.315	6.0233	2.3790
16600	1162.07	675.21	460.10	156.122	5.9043	2.2979
17600	1470.71	833.62	588.75	214.531	5.7824	2.2147
18600	1824.31	1010.04	736.35	283.129	5.6712	2.1301
19600	2211.42	1211.1	902.71	362.444	5.5529	2.0451

Table 6.3: Isothermal elastic constants and other useful information for palladium at T = 900K.

ρ (Kg/m^3)	C_{11} (GPa)	C_{12} (GPa)	C_{44} (GPa)	P (GPa)	$\frac{dP}{dT} \times 10^3$ $(\frac{GPa}{K})$	$C_v \times 10^4$ $(\frac{eV}{K})$
12600	309.15	221.05	121.59	16.228	7.222	2.8857
13600	466.0	310.73	185.45	40.083	7.1319	2.8653
14600	662.55	412.53	265.26	71.575	7.1063	2.8423
15600	894.29	533.66	360.05	111.39	7.1363	2.8176
16600	1163.41	672.63	471.54	160.198	7.1944	2.7918
17600	1473.27	830.62	600.45	218.617	7.2718	2.7655
18600	1828.57	1006.25	747.88	287.228	7.3538	2.7388
19600	2216.05	1207.28	914.11	366.557	7.4405	2.7120

Table 6.4: Isothermal elastic constants and other useful information for palladium at T = 1500K.

ρ (Kg/m^3)	C_{11} (GPa)	C_{12} (GPa)	C_{44} (GPa)	P (GPa)	$\frac{dP}{dT} \times 10^3$ $(\frac{GPa}{K})$	$C_v \times 10^4$ $(\frac{eV}{K})$
12600	307.27	218.19	129.51	20.597	7.3152	2.9472
13600	465.54	308.95	194.08	44.414	7.268	2.9379
14600	662.84	410.38	275.62	75.905	7.284	2.9271
15600	893.14	533.21	371.81	115.752	7.3576	2.9142
16600	1165.45	670.79	484.57	164.612	7.4647	2.8995
17600	1475.5	828.96	614.53	223.093	7.5866	2.8834
18600	1831.84	1004.23	762.49	291.769	7.714	2.8663
19600	2218.35	1206.08	929.33	371.165	7.8466	2.8485

Table 6.5: Isothermal elastic constants and other useful information for rhodium at T = 300K.

ρ (Kg/m^3)	C_{11} (GPa)	C_{12} (GPa)	C_{44} (GPa)	P (GPa)	$\frac{dP}{dT} \times 10^3$ $(\frac{GPa}{K})$	$C_v \times 10^4$ $(\frac{eV}{K})$
13500	670.60	297.31	306.92	30.21	6.4262	2.4408
14300	865.18	379.32	400.74	58.611	6.1727	2.3763
15100	1084.48	472.65	507.82	92.953	5.9716	2.3091
15900	1334.46	575.16	628.19	133.569	5.8147	2.2397
16700	1610.36	690.48	762.08	180.763	5.6741	2.1686
17500	1913.65	818.37	909.87	234.84	5.5292	2.0962
18300	2248.82	957.44	1071.17	296.069	5.3812	2.0231
19100	2612.91	1108.85	1246.36	364.736	5.2631	1.9501

Table 6.6: Isothermal elastic constants and other useful information for rhodium at T = 900K.

ρ (Kg/m^3)	C_{11} (GPa)	C_{12} (GPa)	C_{44} (GPa)	P (GPa)	$\frac{dP}{dT} \times 10^3$ $(\frac{GPa}{K})$	$C_v \times 10^4$ $(\frac{eV}{K})$
13500	656.58	298.77	294.71	34.432	7.3816	2.8253
14300	851.77	382.16	388.83	62.731	7.2357	2.7905
15100	1070.86	476.34	496.56	97.003	7.137	2.7593
15900	1322.21	578.30	617.12	137.585	7.1081	2.7313
16700	1598.97	693.64	751.19	184.758	7.1093	2.7056
17500	1902.01	821.70	898.88	238.808	7.1008	2.6815
18300	2237.0	960.87	1059.76	300.026	7.1235	2.6588
19100	2601.7	1111.84	1234.82	368.688	7.1628	2.6371

Table 6.7: Isothermal elastic constants and other useful information for rhodium at T = 1500K.

ρ (Kg/m^3)	C_{11} (GPa)	C_{12} (GPa)	C_{44} (GPa)	P (GPa)	$\frac{dP}{dT} \times 10^3$ $(\frac{GPa}{K})$	$C_v \times 10^4$ $(\frac{eV}{K})$
13500	641.48	300.94	281.46	39.006	7.8437	3.0372
14300	836.86	385.89	375.68	67.219	7.7003	2.9917
15100	1055.99	480.84	483.96	101.43	7.5981	2.9508
15900	1308.33	582.65	604.61	141.993	7.5639	2.9143
16700	1586.61	697.88	738.94	189.169	7.5652	2.8818
17500	1889.38	826.21	886.58	243.214	7.5518	2.8527
18300	2224.4	965.49	1047.18	304.447	7.5795	2.8266
19100	2590.09	1116.0	1222.23	373.138	7.6242	2.8031

Table 6.8: Isothermal elastic constants and other useful information for platinum at T = 300K.

ρ (Kg/m^3)	C_{11} (GPa)	C_{12} (GPa)	C_{44} (GPa)	P (GPa)	$\frac{dP}{dT} \times 10^3$ $(\frac{GPa}{K})$	$C_v \times 10^4$ $(\frac{eV}{K})$
23000	551.97	359.2	161.1	30.593	6.9682	2.5911
25000	839.09	507.06	275.05	74.961	6.6031	2.5243
27000	1188.54	685.59	418.54	133.726	6.3683	2.4529
29000	1609.69	894.79	593.78	208.244	6.1895	2.3777
31000	2102.4	1136.52	801.73	299.755	6.0427	2.2988
32000	2374.62	1270.99	918.29	352.253	5.9684	2.2585

Table 6.9: Isothermal elastic constants and other useful information for platinum at T = 900K.

ρ (Kg/m^3)	C_{11} (GPa)	C_{12} (GPa)	C_{44} (GPa)	P (GPa)	$\frac{dP}{dT} \times 10^3$ $(\frac{GPa}{K})$	$C_v \times 10^4$ $(\frac{eV}{K})$
23000	550.29	353.46	171.18	35.013	7.5794	2.8621
25000	834.35	505.3	284.98	79.214	7.3372	2.831
27000	1185.87	683.82	428.11	137.896	7.2386	2.8006
29000	1605.6	894.03	602.59	212.369	7.2023	2.7714
31000	2099.95	1135.05	809.55	303.867	7.2318	2.7428
32000	2372.3	1270.03	925.81	356.361	7.249	2.729

Table 6.10: Isothermal elastic constants and other useful information for platinum at T = 1500K.

ρ (Kg/m^3)	C_{11} (GPa)	C_{12} (GPa)	C_{44} (GPa)	P (GPa)	$\frac{dP}{dT} \times 10^3$ $(\frac{GPa}{K})$	$C_v \times 10^4$ $(\frac{eV}{K})$
23000	548.23	348.22	181.08	39.626	7.7646	2.9588
25000	827.14	505.36	295.62	83.692	7.5587	2.9349
27000	1181.76	683.49	439.34	142.325	7.4923	2.9102
29000	1600.51	894.42	613.81	216.787	7.4873	2.8857
31000	2098.85	1133.39	820.32	308.315	7.5502	2.8613
32000	2372.13	1268.78	936.57	360.823	7.5806	2.8495

Table 6.11: Isothermal elastic constants and other useful information for molybdenum at T = 300K.

ρ (Kg/m^3)	C_{11} (GPa)	C_{12} (GPa)	C_{44} (GPa)	P (GPa)	$\frac{dP}{dT} \times 10^3$ $(\frac{GPa}{K})$	$C_v \times 10^4$ $(\frac{eV}{K})$
11001.15	634.79	228.0	164.24	23.572	3.86	2.3943
12251.28	915.83	333.02	267.2	72.745	3.3468	2.3151
13501.41	1245.95	460.24	393.52	136.268	3.051	2.2397
14751.54	1621.13	614.51	536.87	215.152	2.5901	2.1687
16001.67	2011.22	782.83	701.68	308.865	2.1529	2.1074

Table 6.12: Isothermal elastic constants and other useful information for molybdenum at T = 900K.

ρ (Kg/m^3)	C_{11} (GPa)	C_{12} (GPa)	C_{44} (GPa)	P (GPa)	$\frac{dP}{dT} \times 10^3$ $(\frac{GPa}{K})$	$C_v \times 10^4$ $(\frac{eV}{K})$
11001.15	611.38	234.66	165.68	26.065	4.2694	2.6924
12251.28	902.53	334.7	268.95	74.961	3.8234	2.6757
13501.41	1229.97	465.82	396.23	138.341	3.5886	2.6631
14751.54	1598.81	616.2	542.32	216.973	3.1997	2.6525
16001.67	2003.56	787.51	713.93	310.455	2.8279	2.6429

Table 6.13: Isothermal elastic constants and other useful information for molybdenum at T = 1500K.

ρ (Kg/m^3)	C_{11} (GPa)	C_{12} (GPa)	C_{44} (GPa)	P (GPa)	$\frac{dP}{dT} \times 10^3$ $(\frac{GPa}{K})$	$C_v \times 10^4$ $(\frac{eV}{K})$
11001.15	583.97	243.47	166.87	28.658	4.3683	2.8116
12251.28	889.28	335.94	270.38	77.284	3.9123	2.7921
13501.41	1212.01	472.63	398.97	140.512	3.644	2.7801
14751.54	1575.73	618.35	548.48	218.923	3.2831	2.7723
16001.67	1995.71	793.13	727.75	312.174	2.8812	2.7685

Table 6.14: Isothermal elastic constants and other useful information for hcp-iron at T = 300K.

ρ (Kg/m^3)	C_{11} (GPa)	C_{12} (GPa)	C_{13} (GPa)	C_{33} (GPa)	C_{44} (GPa)	T^{xy} (GPa)	T^z (GPa)	$\frac{dT^{xy}}{dT} \times 10^3$ $(\frac{GPa}{K})$	$\frac{dT^z}{dT} \times 10^3$ $(\frac{GPa}{K})$	$C_v \times 10^4$ $(\frac{eV}{K})$
10900	1083.47	365.24	294.26	1189.7	346.8	-69.654	-69.772	-6.0836	-6.7882	4.3034
11800	1441.95	493.75	391.54	1586.08	470.02	-125.962	-126.072	-5.9632	-6.3453	4.0531
12700	1865.37	620.55	506.59	2045.34	615.1	-195.116	-195.052	-5.7321	-5.859	3.8048
13600	2347.31	788.65	623.22	2583.75	780.18	-277.561	-277.849	-5.7147	-5.339	3.5609

Table 6.15: Isothermal elastic constants and other useful information for hcp-iron at T = 1500K.

ρ (Kg/m^3)	C_{11} (GPa)	C_{12} (GPa)	C_{13} (GPa)	C_{33} (GPa)	C_{44} (GPa)	T^{xy} (GPa)	T^z (GPa)	$\frac{dT^{xy}}{dT} \times 10^3$ $(\frac{GPa}{K})$	$\frac{dT^z}{dT} \times 10^3$ $(\frac{GPa}{K})$	$C_v \times 10^4$ $(\frac{eV}{K})$
10900	1082.3	353.18	297.61	1165.48	300.52	-79.202	-79.12	-7.9929	-9.8951	5.9019
11800	1422.48	486.44	410.01	1557.23	427.58	-135.661	-135.66	-8.3039	-9.8175	5.7971
12700	1881.83	597.36	515.97	2006.52	577.08	-204.703	-204.707	-8.4608	-9.558	5.7109
13600	2366.7	744.96	641.34	2549.69	740.97	-287.36	-287.357	-8.8158	-9.2634	5.6368

Using the information given in the tables 6.2 through 6.15 the adiabatic elastic moduli and elastic wave speed of any desired type can be calculated (see sections 2.2.7 and 2.3). We show the plots of the direction-averaged longitudinal acoustic wave speed and the P-wave speed in the figures 6.9 through 6.18. As far as we are aware these are the first full calculations of how the dependence of elastic wave speed on density evolves with temperature. In the figures for the cubic materials we have omitted the data for 900K for the sake of visual clarity. The first point to note is that, for a given density, the elastic wave speed decreases with increasing temperature for some materials whereas it is the opposite for others. In particular we notice that for iron it decreases with temperature. This is qualitatively consistent with the known experimental and computational results regarding hcp-iron – although we find that the decrease of speed is somewhat less than what is seen in laboratory experiments. Among the other four materials studied speed goes up with rising temperature for platinum and palladium whereas it goes down for rhodium in the same situation. For molybdenum it is found that there exists a critical density below which the speed decreases with rising temperature and above which the variation with temperature is of the opposite type.

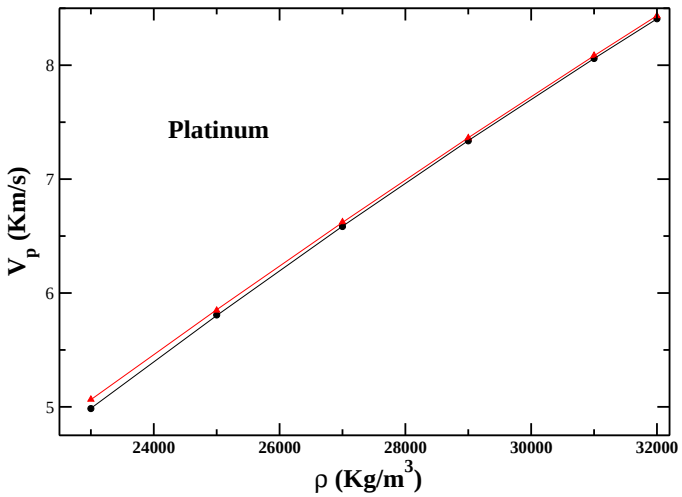

Figure 6.9: P-wave speed (V_P) is plotted as a function density (ρ) at the temperatures of 300K (black) and 1500K (red).

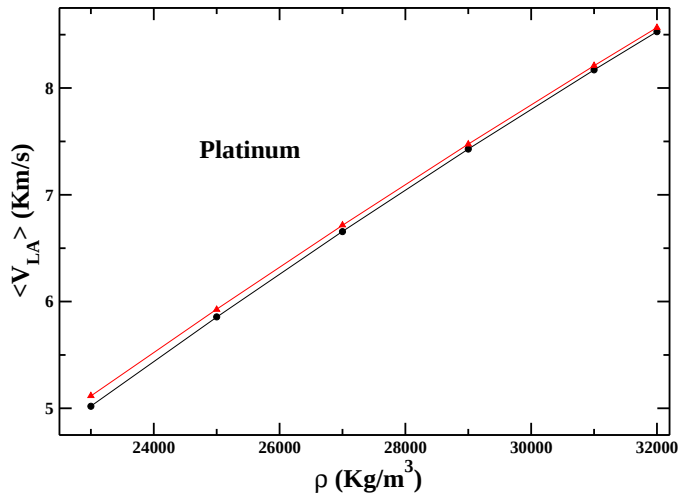

Figure 6.10: Direction-averaged longitudinal acoustic wave speed ($< V_{LA} >$) is plotted as function of density (ρ) at the temperatures of 300K (black) and 1500K (red).

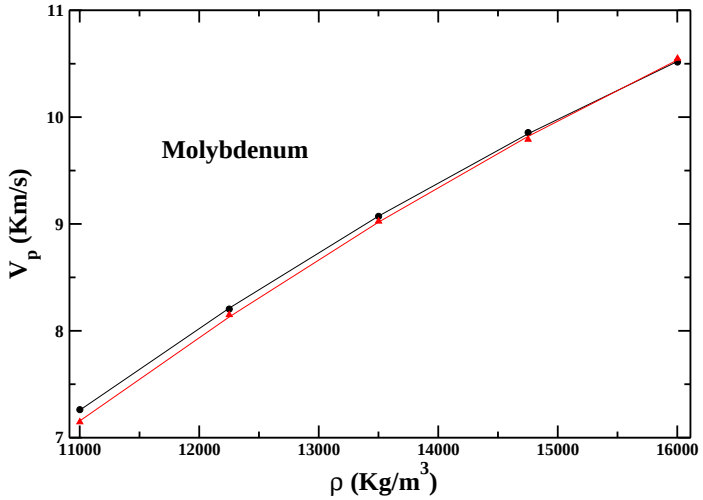

Figure 6.11: P-wave speed (V_P) is plotted as a function density (ρ) at the temperatures of 300K (black) and 1500K (red).

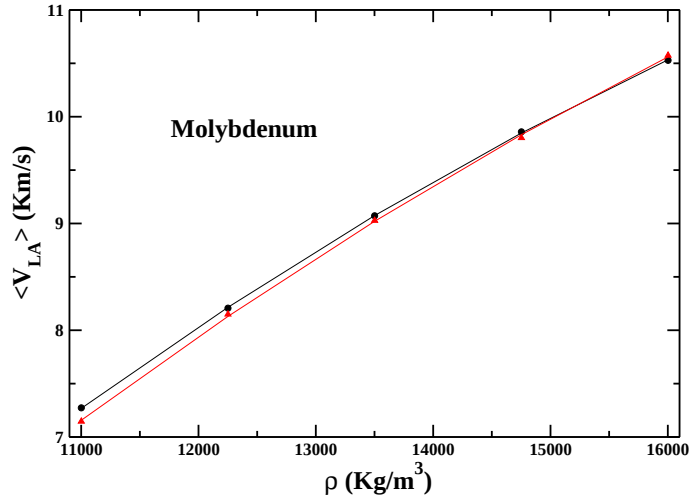

Figure 6.12: Direction-averaged longitudinal acoustic wave speed ($< V_{LA} >$) is plotted as function of density (ρ) at the temperatures of 300K (black) and 1500K (red).

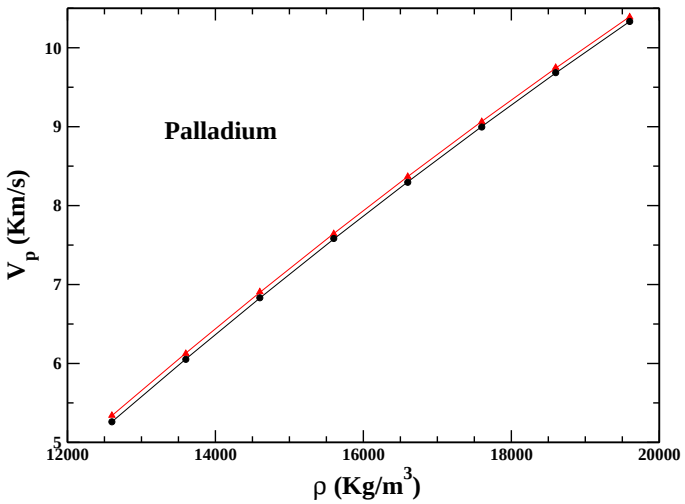

Figure 6.13: P-wave speed (V_P) is plotted as a function density (ρ) at the temperatures of 300K (black) and 1500K (red).

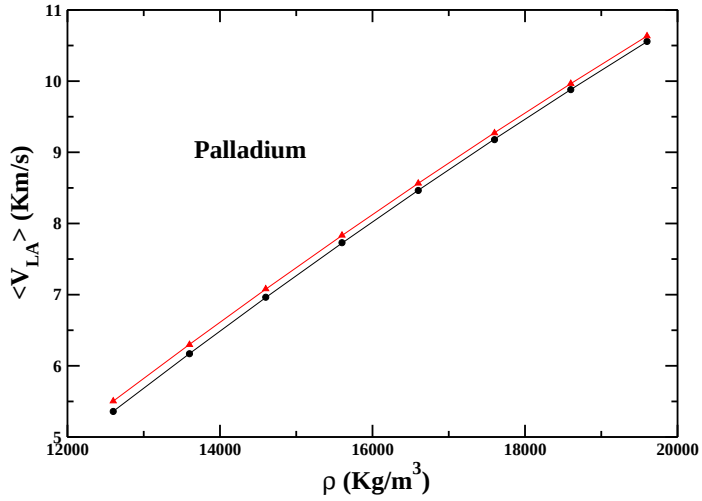

Figure 6.14: Direction-averaged longitudinal acoustic wave speed ($< V_{LA} >$) is plotted as function of density (ρ) at the temperatures of 300K (black) and 1500K (red).

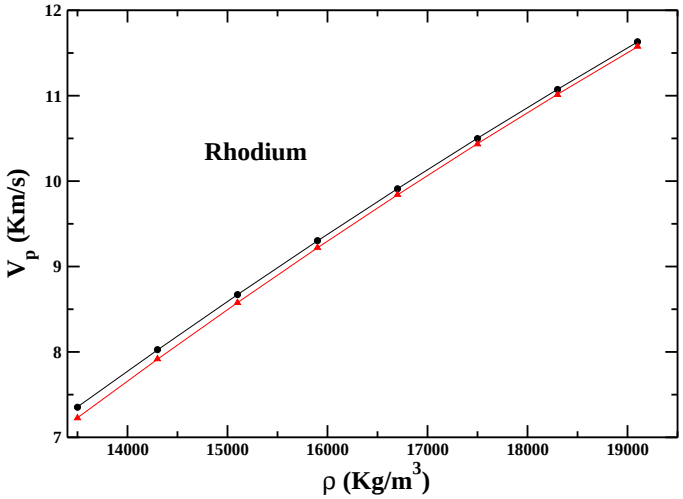

Figure 6.15: P-wave speed (V_P) is plotted as a function density (ρ) at the temperatures of 300K (black) and 1500K (red).

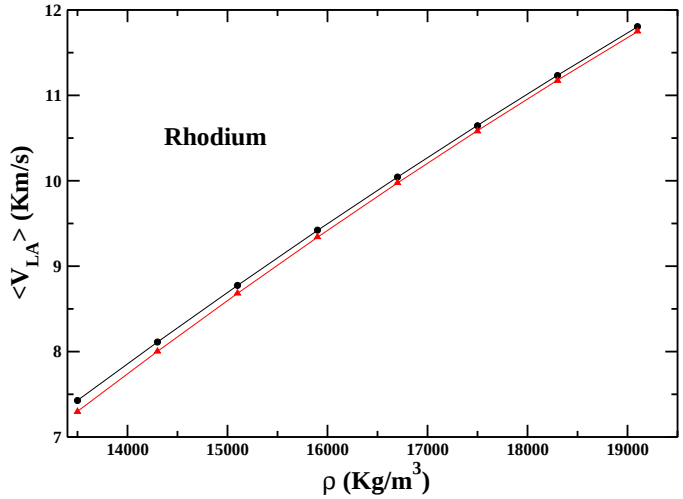

Figure 6.16: Direction-averaged longitudinal acoustic wave speed ($< V_{LA} >$) is plotted as function of density (ρ) at the temperatures of 300K (black) and 1500K (red).

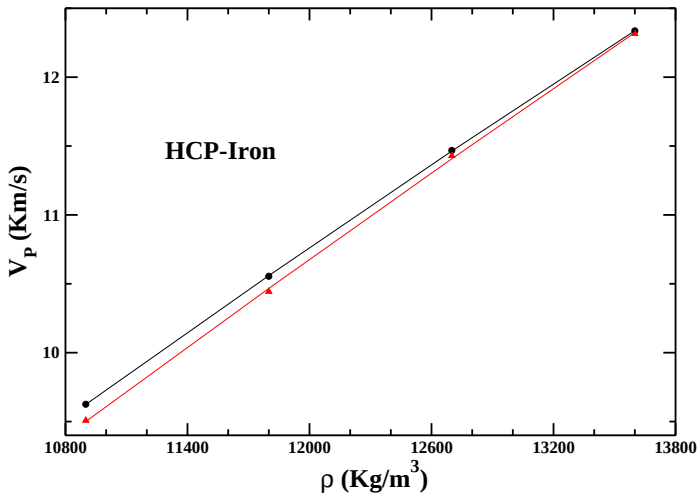

Figure 6.17: P-wave speed (V_P) is plotted as a function density (ρ) at the temperatures of 300K (black) and 1500K (red).

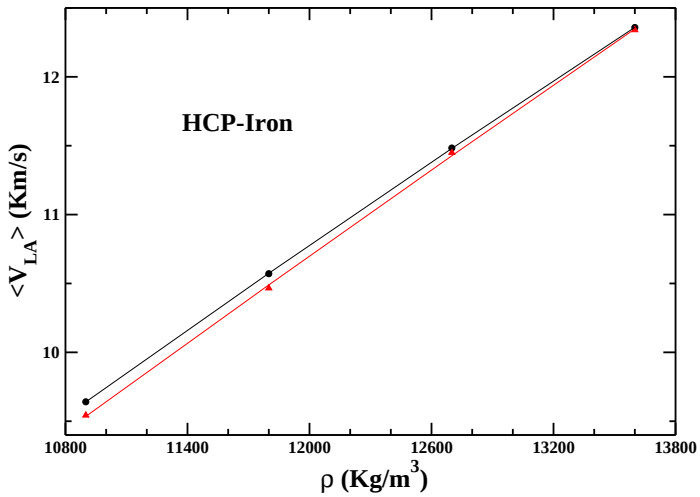

Figure 6.18: Direction-averaged longitudinal acoustic wave speed ($< V_{LA} >$) is plotted as function of density (ρ) at temperatures of 300K (black) and 1500K (red).

This critical density is just below the highest density we have studied. It may be noted that the phase stability of molybdenum at the highest densities we have studied is a matter of some controversy [108,118]. We have not attempted to investigate this aspect in our work. If we leave out molybdenum the extent of the effect of temperature on the variation of speed with density is physically sensible. In each case we find that a specified change of temperature causes a steadily decreasing change of elastic wave speed as the density increases. This is how it should be since increasing density corresponds to increasing pressure – which in turn suppresses atomic vibration. This latter fact leads to steadily decreasing impact of a given change of temperature. Our calculations regarding the impact of changing temperature on the elastic wave speeds are predictions that can be experimentally verified. For the cubic materials we are not aware of any experimental work analogous to our computational studies.

Table 6.16: Data for maximum fractional deviation

System	T (K)	Maximum fractional deviation				Maximum fractional uncertainty for V_P
		$< V_{LA} >$		V_P		
		$V-\rho$	$V\rho^{1/3}-\rho$	$V-\rho$	$V\rho^{1/3}-\rho$	
Pt	300	1.2×10^{-2}	6.9×10^{-4}	1.3×10^{-2}	8.7×10^{-4}	3.0×10^{-3}
	900	1.1×10^{-2}	6.8×10^{-4}	1.1×10^{-2}	5.4×10^{-4}	3.3×10^{-3}
	1500	9.8×10^{-3}	1.6×10^{-3}	9.7×10^{-3}	2.6×10^{-3}	3.3×10^{-3}
Mo	300	2.8×10^{-2}	1.4×10^{-2}	3.6×10^{-2}	1.5×10^{-2}	5.3×10^{-5}
	900	2.6×10^{-2}	1.2×10^{-2}	2.8×10^{-2}	1.3×10^{-2}	9.4×10^{-5}
	1500	2.7×10^{-2}	1.2×10^{-2}	2.8×10^{-2}	1.3×10^{-2}	1.6×10^{-4}
Pd	300	1.6×10^{-2}	1.1×10^{-3}	1.6×10^{-2}	1.3×10^{-3}	6.0×10^{-3}
	900	1.5×10^{-2}	1.8×10^{-3}	1.7×10^{-2}	1.6×10^{-3}	6.5×10^{-3}
	1500	1.4×10^{-2}	2.0×10^{-3}	1.7×10^{-2}	1.9×10^{-3}	8.8×10^{-3}
Rh	300	1.6×10^{-2}	2.3×10^{-3}	1.6×10^{-2}	2.6×10^{-3}	2.2×10^{-3}
	900	1.7×10^{-2}	3.2×10^{-3}	1.7×10^{-2}	3.4×10^{-3}	2.2×10^{-3}
	1500	1.8×10^{-2}	4.0×10^{-3}	1.8×10^{-2}	3.9×10^{-3}	2.3×10^{-3}
Hcp-Fe	300	6.1×10^{-3}	1.6×10^{-3}	7.3×10^{-3}	1.5×10^{-3}	1.4×10^{-3}
	1500	1.1×10^{-2}	8.8×10^{-3}	1.2×10^{-2}	7.5×10^{-3}	2.8×10^{-3}

Table 6.17: Data for mean fractional deviation

System	T (K)	Mean fractional deviation			
		V_{LA}		V_P	
		$V-\rho$	$V\rho^{1/3}-\rho$	$V-\rho$	$V\rho^{1/3}-\rho$
Pt	300	8.0×10^{-3}	3.8×10^{-4}	8.4×10^{-3}	5.7×10^{-4}
	900	7.3×10^{-3}	4.1×10^{-4}	7.3×10^{-3}	3.6×10^{-4}
	1500	6.6×10^{-3}	8.9×10^{-4}	5.9×10^{-3}	1.5×10^{-3}
Mo	300	2.1×10^{-2}	9.9×10^{-3}	2.3×10^{-2}	1.1×10^{-2}
	900	2.0×10^{-2}	8.7×10^{-3}	2.1×10^{-2}	9.6×10^{-3}
	1500	1.9×10^{-2}	8.0×10^{-3}	2.0×10^{-2}	8.6×10^{-3}
Pd	300	8.8×10^{-3}	5.8×10^{-4}	9.3×10^{-3}	7.4×10^{-4}
	900	8.6×10^{-3}	7.8×10^{-4}	9.3×10^{-3}	7.3×10^{-4}
	1500	8.5×10^{-3}	8.3×10^{-4}	9.3×10^{-3}	9.4×10^{-4}
Rh	300	8.8×10^{-3}	1.4×10^{-3}	8.7×10^{-3}	1.4×10^{-3}
	900	9.5×10^{-3}	1.9×10^{-3}	9.3×10^{-3}	1.8×10^{-3}
	1500	1.0×10^{-2}	2.4×10^{-3}	9.8×10^{-3}	2.2×10^{-3}
Hcp-Fe	300	5.0×10^{-3}	8.0×10^{-4}	5.7×10^{-3}	9.7×10^{-4}
	1500	5.6×10^{-3}	4.4×10^{-3}	6.2×10^{-3}	4.3×10^{-3}

In order to test the compliance of our elastic wave speed data at elevated temperatures with the Birch's law, we compute (as in chapters 4 and 5) the relevant metrics for both $< V_{LA} >$ and V_P. These values are listed in table 6.16 and 6.17. As in chapter 5 our conclusion is again that, at least up to the temperatures studied, the modified Birch's law conforms more accurately to a straight line fit than does the original version. However, the data also suggests that the degree of superiority is decreasing with rising temperature. The possible causes of this degradation are: (i) increasing error bar of the calculation itself at higher temperatures – may be due to inadequate convergence in the calculation of free energy; (ii) error in the calculation of the optimal lattice parameter(s) at a given temperature in the case of systems with more than one lattice parameter (actually this is also affected by the first cause); and of course (iii) a genuine failure of the modified Birch's law at elevated temperatures.

To check the first possibility we have carried out an analysis along the following lines: Suppose, in a plot of the free energy versus the amplitude of distortion,

we calculate the root-mean-square deviation (σ) of the data points around the best fit cubic polynomial. Since even the maximum value of the amplitude of distortion is very small, the most likely cause of a larger value of this number is inadequate convergence in the calculation of free energy. The basis of this conclusion is that inadequate (but not grossly inadequate) convergence usually manifests itself as a pseudo-random noise. The scale with which to compare this root-mean-square deviation is the range of variation (R) of the free energy across the entire range of distortions of that particular type. We present the data for the ratio σ/R in the tables 6.18 through 6.31.

Table 6.18: Values of σ/R for palladium: Temperature = 300K

$\rho(Kg/m^3)$	Distortion $\eta^{(1)}$	Distortion $\eta^{(8)}$	Distortion $\eta^{(23)}$
12600	1.0×10^{-4}	1.0×10^{-4}	1.8×10^{-3}
13600	4.3×10^{-5}	5.7×10^{-5}	1.1×10^{-3}
14600	3.3×10^{-5}	3.7×10^{-5}	8.7×10^{-4}
15600	9.6×10^{-6}	1.7×10^{-5}	5.0×10^{-4}
16600	1.7×10^{-5}	2.1×10^{-5}	5.1×10^{-4}
17600	1.1×10^{-5}	1.4×10^{-5}	5.2×10^{-4}
18600	1.2×10^{-5}	8.1×10^{-6}	5.0×10^{-4}
19600	1.4×10^{-5}	8.9×10^{-6}	5.1×10^{-4}

Table 6.19: Values of σ/R for palladium: Temperature = 900K

$\rho(Kg/m^3)$	Distortion $\eta^{(1)}$	Distortion $\eta^{(8)}$	Distortion $\eta^{(23)}$
12600	1.1×10^{-4}	1.7×10^{-4}	4.0×10^{-3}
13600	7.1×10^{-5}	8.1×10^{-5}	2.4×10^{-3}
14600	4.8×10^{-5}	9.6×10^{-5}	1.8×10^{-3}
15600	3.0×10^{-5}	1.5×10^{-5}	1.1×10^{-3}
16600	2.1×10^{-5}	2.3×10^{-5}	8.3×10^{-4}
17600	1.4×10^{-5}	1.4×10^{-5}	8.0×10^{-4}
18600	1.4×10^{-5}	7.4×10^{-6}	5.0×10^{-4}
19600	1.4×10^{-5}	7.5×10^{-6}	4.4×10^{-4}

It can be seen that this ratio increases with decreasing density. It is also substantially higher for the distortion $\eta^{(23)}$ for the cubic cases and for the distortion $\eta^{(26)}$ for the hcp case. These two observations are explained by the fact that the change of the free energy due to a given amplitude of distortion is dominated by

Table 6.20: Values of σ/R for palladium: Temperature = 1500K

$\rho(Kg/m^3)$	Distortion $\eta^{(1)}$	Distortion $\eta^{(8)}$	Distortion $\eta^{(23)}$
12600	2.1×10^{-4}	2.9×10^{-4}	5.8×10^{-3}
13600	1.8×10^{-4}	1.3×10^{-4}	3.6×10^{-3}
14600	8.6×10^{-5}	1.8×10^{-4}	2.7×10^{-3}
15600	6.6×10^{-5}	2.1×10^{-5}	1.9×10^{-3}
16600	2.9×10^{-5}	3.0×10^{-5}	1.4×10^{-3}
17600	1.9×10^{-5}	2.1×10^{-5}	1.3×10^{-3}
18600	1.8×10^{-5}	9.0×10^{-6}	9.0×10^{-4}
19600	1.5×10^{-5}	8.7×10^{-6}	8.1×10^{-4}

Table 6.21: Values of σ/R for platinum: Temperature = 300K

$\rho(Kg/m^3)$	Distortion $\eta^{(1)}$	Distortion $\eta^{(8)}$	Distortion $\eta^{(23)}$
23000	4.8×10^{-5}	5.6×10^{-5}	1.1×10^{-3}
25000	3.3×10^{-5}	3.3×10^{-5}	9.3×10^{-4}
27000	1.2×10^{-5}	1.8×10^{-5}	7.9×10^{-4}
29000	1.8×10^{-5}	1.2×10^{-5}	8.2×10^{-4}
31000	1.6×10^{-5}	6.6×10^{-6}	6.4×10^{-4}
32000	7.9×10^{-6}	1.1×10^{-5}	6.3×10^{-4}

Table 6.22: Values of σ/R for platinum: Temperature = 900K

$\rho(Kg/m^3)$	Distortion $\eta^{(1)}$	Distortion $\eta^{(8)}$	Distortion $\eta^{(23)}$
23000	9.5×10^{-5}	6.3×10^{-5}	1.3×10^{-3}
25000	7.3×10^{-5}	2.7×10^{-5}	1.0×10^{-3}
27000	1.7×10^{-5}	1.3×10^{-5}	8.0×10^{-4}
29000	2.0×10^{-5}	2.2×10^{-5}	7.2×10^{-4}
31000	1.8×10^{-5}	1.2×10^{-5}	6.6×10^{-4}
32000	6.2×10^{-6}	1.4×10^{-5}	5.7×10^{-4}

Table 6.23: Values of σ/R for platinum: Temperature = 1500K

$\rho(Kg/m^3)$	Distortion $\eta^{(1)}$	Distortion $\eta^{(8)}$	Distortion $\eta^{(23)}$
23000	1.5×10^{-4}	1.3×10^{-4}	2.6×10^{-3}
25000	1.4×10^{-4}	2.3×10^{-5}	2.0×10^{-3}
27000	3.6×10^{-5}	1.6×10^{-5}	1.2×10^{-3}
29000	3.2×10^{-5}	4.2×10^{-5}	1.0×10^{-3}
31000	2.2×10^{-5}	2.1×10^{-5}	8.2×10^{-4}
32000	6.5×10^{-6}	2.0×10^{-5}	6.1×10^{-4}

Table 6.24: Values of σ/R for molybdenum: Temperature = 300K

$\rho(Kg/m^3)$	Distortion $\eta^{(1)}$	Distortion $\eta^{(8)}$	Distortion $\eta^{(23)}$
11001.15	1.8×10^{-5}	2.9×10^{-5}	4.1×10^{-4}
12251.28	1.5×10^{-5}	1.3×10^{-5}	3.0×10^{-4}
13501.41	1.5×10^{-5}	9.3×10^{-6}	4.6×10^{-4}
14751.54	1.8×10^{-5}	1.8×10^{-5}	9.7×10^{-4}
16001.67	1.0×10^{-5}	8.3×10^{-6}	4.4×10^{-4}

Table 6.25: Values of σ/R for molybdenum: Temperature = 900K

$\rho(Kg/m^3)$	Distortion $\eta^{(1)}$	Distortion $\eta^{(8)}$	Distortion $\eta^{(23)}$
11001.15	2.7×10^{-4}	1.5×10^{-4}	6.8×10^{-4}
12251.28	5.1×10^{-5}	3.8×10^{-5}	6.3×10^{-4}
13501.41	4.1×10^{-5}	2.2×10^{-5}	8.5×10^{-4}
14751.54	1.8×10^{-5}	2.5×10^{-5}	1.1×10^{-3}
16001.67	1.7×10^{-5}	6.1×10^{-5}	9.0×10^{-4}

Table 6.26: Values of σ/R for molybdenum: Temperature = 1500K

$\rho(Kg/m^3)$	Distortion $\eta^{(1)}$	Distortion $\eta^{(8)}$	Distortion $\eta^{(23)}$
11001.15	6.1×10^{-4}	3.4×10^{-4}	1.6×10^{-3}
12251.28	1.2×10^{-4}	8.7×10^{-5}	1.2×10^{-3}
13501.41	1.1×10^{-4}	4.3×10^{-5}	1.7×10^{-3}
14751.54	2.9×10^{-5}	3.7×10^{-5}	1.3×10^{-3}
16001.67	2.7×10^{-5}	1.2×10^{-5}	1.3×10^{-3}

Table 6.27: Values of σ/R for rhodium: Temperature = 300K

$\rho(Kg/m^3)$	Distortion $\eta^{(1)}$	Distortion $\eta^{(8)}$	Distortion $\eta^{(23)}$
13500	8.6×10^{-5}	3.2×10^{-5}	3.1×10^{-4}
14300	2.5×10^{-5}	1.8×10^{-5}	7.2×10^{-5}
15100	1.3×10^{-5}	1.1×10^{-5}	1.2×10^{-4}
15900	1.4×10^{-5}	9.7×10^{-6}	1.4×10^{-4}
16700	1.2×10^{-5}	7.9×10^{-6}	1.7×10^{-4}
17500	1.2×10^{-5}	1.0×10^{-5}	1.6×10^{-4}
18300	8.2×10^{-6}	1.3×10^{-5}	1.4×10^{-4}
19100	1.1×10^{-5}	1.1×10^{-5}	2.1×10^{-4}

Table 6.28: Values of σ/R for rhodium: Temperature = 900K

$\rho(Kg/m^3)$	Distortion $\eta^{(1)}$	Distortion $\eta^{(8)}$	Distortion $\eta^{(23)}$
13500	9.9×10^{-5}	8.9×10^{-5}	1.3×10^{-3}
14300	4.3×10^{-5}	2.9×10^{-5}	2.6×10^{-4}
15100	2.4×10^{-5}	2.1×10^{-5}	1.5×10^{-4}
15900	1.7×10^{-5}	2.5×10^{-5}	1.6×10^{-4}
16700	1.4×10^{-5}	1.8×10^{-5}	1.8×10^{-4}
17500	9.2×10^{-6}	1.5×10^{-5}	1.4×10^{-4}
18300	9.4×10^{-6}	8.7×10^{-6}	2.2×10^{-4}
19100	1.3×10^{-5}	1.3×10^{-5}	1.9×10^{-4}

Table 6.29: Values of σ/R for rhodium: Temperature = 1500K

$\rho(Kg/m^3)$	Distortion $\eta^{(1)}$	Distortion $\eta^{(8)}$	Distortion $\eta^{(23)}$
13500	1.9×10^{-4}	2.1×10^{-4}	2.8×10^{-3}
14300	8.9×10^{-5}	7.2×10^{-5}	6.8×10^{-4}
15100	4.4×10^{-5}	5.3×10^{-5}	3.5×10^{-4}
15900	2.9×10^{-5}	6.0×10^{-5}	3.7×10^{-4}
16700	2.1×10^{-5}	3.9×10^{-5}	2.2×10^{-4}
17500	1.1×10^{-5}	2.8×10^{-5}	1.5×10^{-4}
18300	1.3×10^{-5}	9.6×10^{-6}	3.9×10^{-4}
19100	1.6×10^{-5}	2.2×10^{-5}	1.6×10^{-4}

Table 6.30: Values of σ/R for hcp-iron: Temperature = 300K

$\rho(Kg/m^3)$	Distortion $\eta^{(1)}$	Distortion $\eta^{(26)}$	Distortion $\eta^{(4)}$	Distortion $\eta^{(3)}$	Distortion $\eta^{(17)}$
10900	3.5×10^{-5}	1.5×10^{-3}	5.6×10^{-5}	1.0×10^{-4}	1.0×10^{-4}
11800	1.6×10^{-5}	8.4×10^{-4}	4.4×10^{-5}	7.4×10^{-5}	4.2×10^{-5}
12700	2.8×10^{-5}	6.1×10^{-4}	2.2×10^{-5}	6.2×10^{-5}	1.5×10^{-4}
13600	1.2×10^{-5}	5.1×10^{-4}	1.7×10^{-5}	2.1×10^{-5}	4.1×10^{-5}

Table 6.31: Values of σ/R for hcp-iron: Temperature = 1500K

$\rho(Kg/m^3)$	Distortion $\eta^{(1)}$	Distortion $\eta^{(26)}$	Distortion $\eta^{(4)}$	Distortion $\eta^{(3)}$	Distortion $\eta^{(17)}$
10900	1.1×10^{-4}	2.2×10^{-3}	4.7×10^{-4}	5.7×10^{-4}	3.4×10^{-4}
11800	9.6×10^{-5}	2.5×10^{-3}	2.0×10^{-4}	2.4×10^{-4}	1.1×10^{-4}
12700	5.9×10^{-5}	2.8×10^{-3}	9.9×10^{-5}	2.2×10^{-4}	3.8×10^{-4}
13600	5.5×10^{-5}	9.9×10^{-4}	5.4×10^{-5}	5.1×10^{-5}	1.1×10^{-4}

the linear term when it is present. However, for the distortion type $\eta^{(23)}$ for the cubic cases this linear term is entirely absent. For the distortion type $\eta^{(26)}$ for the hcp case, this is proportional to the difference $(T^{xy} - T^{z})$. Now, for hcp-iron the values of T^{xy} and T^{z} are almost identical (see tables 6.14 and 6.15) (i.e. *de facto* the situation is almost like that of hydrostatic pressure). As a result the coefficient of the linear term is almost zero. Thus the range of variation (R) of the free energy is relatively small for these two types of distortion. Also a smaller value of density means lower stress and a smaller value of the coefficient of the linear term – when it is present. Thus, generally speaking, smaller densities are more challenging computationally.

The two factors just discussed have to do with the denominator R. The numerator, on the other hand, has to do with the level of convergence of free energy. Comparison across tables for different temperatures clearly shows that indeed the noise level is increasing with rising temperature – consistently and for all materials. Thus the level of convergence is indeed an issue. But we believe that the issue of convergence has caused visibly significant problem mostly for hcp-iron at 1500K due to its impact on locating the value of the lattice parameter – especially at lower densities. It so happens that the graph of the Helmhotz free energy versus a (or c) is rather flat near the minimum at the lower densities. This already makes it difficult to determine the location of the minimum of the free energy (and thus the optimal value of the lattice constant). This is compounded further by convergence issues. Thus it is quite difficult to reliably calculate the weakly temperature dependent lattice constant for the hcp-case. In contrast no separate calculations are needed to determine the lattice parameter for cubic materials . Due to this reason we believe that the calculations for the cubic materials are much less susceptible to convergence issues and are quite reliable as they stand. The steady but not-so-radical degradation in the superiority of the modified Birch's law seems to be the residual effect of the convergence issues becoming gradually worse with increasing temperature.

For hcp-iron the effect, through the error in the determination of the optimal value of the lattice constant, seems to be significantly worse. It seems likely that possibly an order of magnitude higher level of convergence in the calculation of free energy will be required to decisively settle the issue of whether the apparent

loss of superiority of the modified Birch's law in the case of hcp-iron at 1500K is caused only by limited convergence or it is due to a genuine failure of the modified Birch's law itself.

Finally, we touch upon an aspect of a recent work on hcp-iron [2] in which it was assumed that that V_P is a linear function of temperature at a given value of the density. This is a *de facto* extension of the Birch's law. We have carried out a test of this idea for the cubic materials but only at the highest densities and up to 3300K. The reason for using only the highest densities is that it is only when the stress is sufficiently high that the quasi-harmonic approximation is likely to hold at such high temperatures. In figures 6.19 through 6.26 we show the results of this calculation.

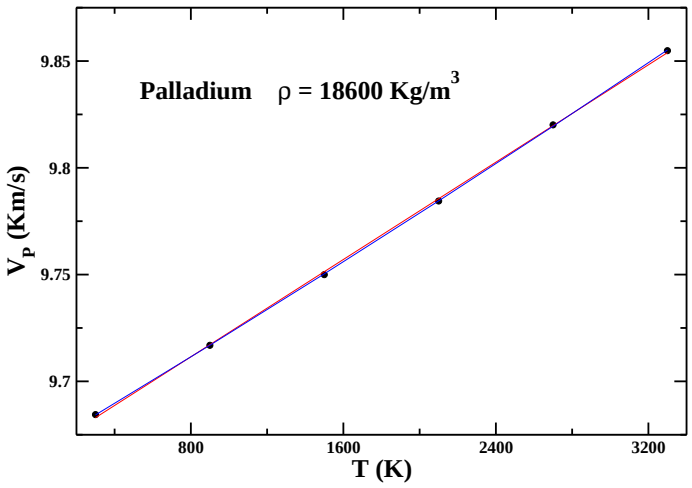

Figure 6.19: P-wave speed (V_P) is plotted as a function of temperature (T). The best linear fit (red) and quadratic fit (blue) are also shown.

Each graph shows the P-wave speed V_P plotted as a function of temperature – as well as the best linear and quadratic fits to this data. We find that while the assumption of linearity works very well for palladium its applicability in other cases is variable. As has been noted earlier, for molybdenum the elastic wave speed can increase with temperature or decrease with temperature. It depends

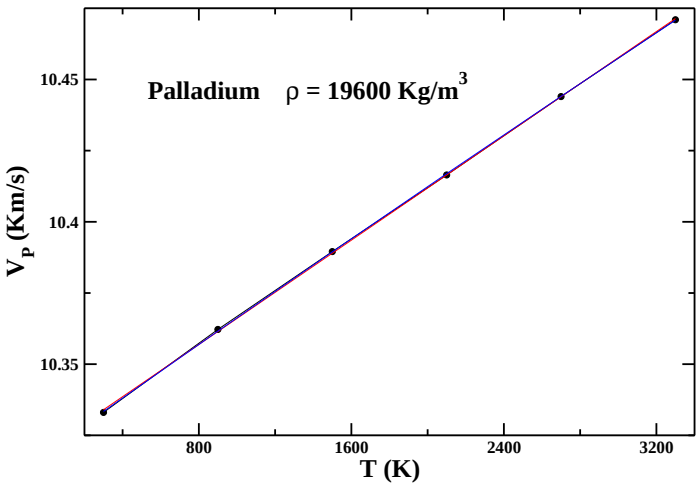

Figure 6.20: P-wave speed (V_P) is plotted as a function of temperature (T). The best linear fit (red) and quadratic fit (blue) are also shown.

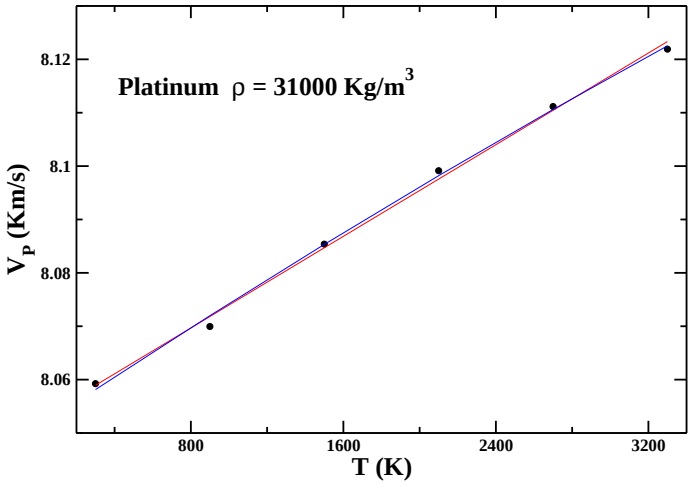

Figure 6.21: P-wave speed (V_P) is plotted as a function of temperature (T). The best linear fit (red) and quadratic fit (blue) are also shown.

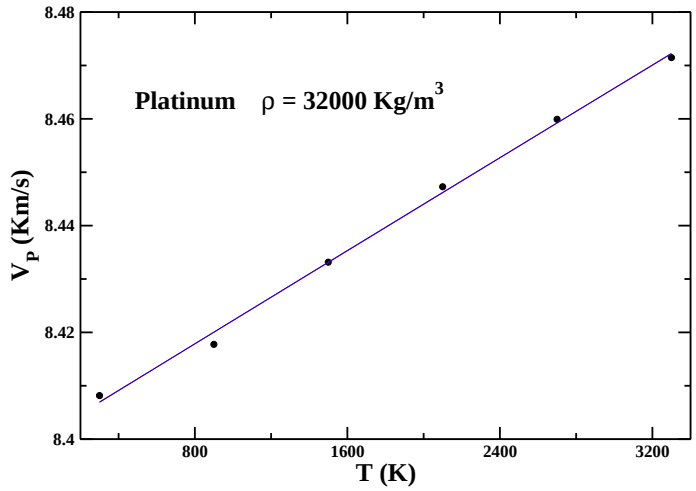

Figure 6.22: P-wave speed (V_P) is plotted as a function of temperature (T). The best linear fit (red) and quadratic fit (blue) are also shown. The two best fit curves are almost indistinguishable in this case since the coefficient of the quadratic term is extremely small.

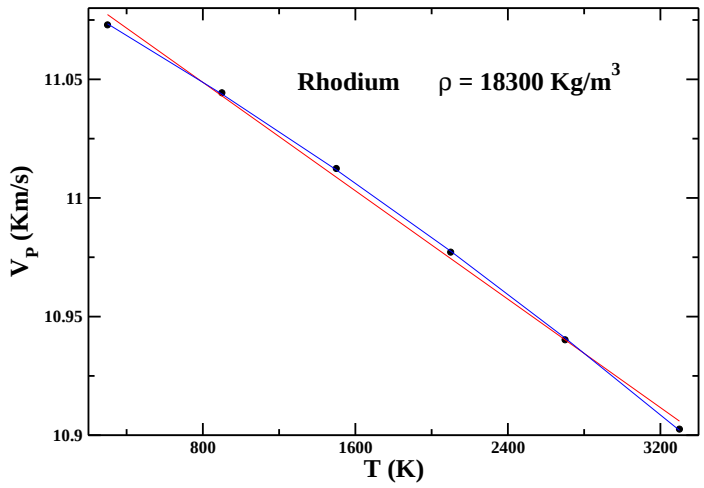

Figure 6.23: P-wave speed (V_P) is plotted as a function of temperature (T). The best linear fit (red) and quadratic fit (blue) are also shown.

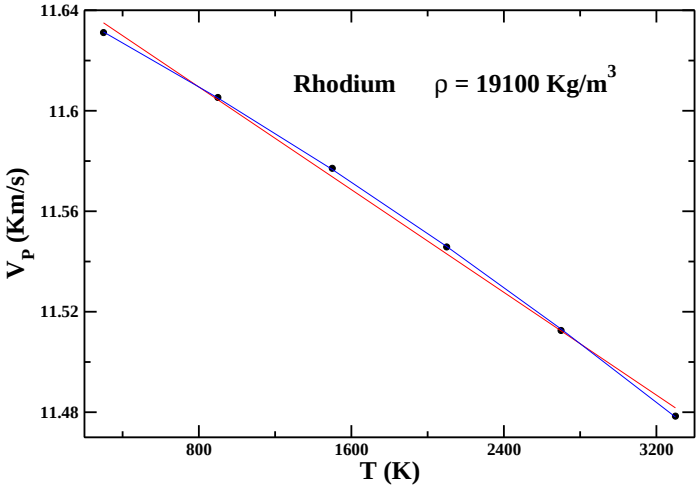

Figure 6.24: P-wave speed (V_P) is plotted as a function of temperature (T). The best linear fit (red) and quadratic fit (blue) are also shown.

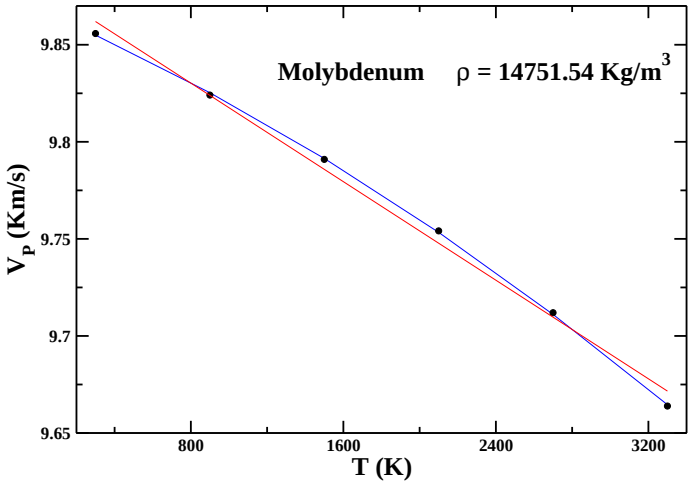

Figure 6.25: P-wave speed (V_P) is plotted as a function of temperature (T). The best linear fit (red) and quadratic fit (blue) are also shown.

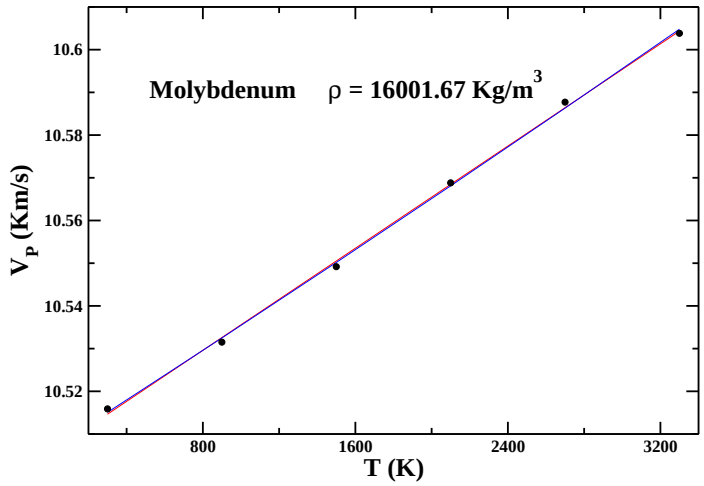

Figure 6.26: P-wave speed (V_P) is plotted as a function of temperature (T). The best linear fit (red) and quadratic fit (blue) are also shown.

on the density. In general a quadratic fit to the V_P versus temperature data is more accurate and can perhaps be used to extrapolate the speed data obtained at high densities, but not so high temperatures (if such data is available from experiments), to the high temperatures often of interest in terrestrial geophysics.

Chapter 7

Summary and conclusion

7.1 Summary and conclusion

In this thesis we have introduced a modified version of the Birch's law. We then examined a large array of experimental and computational data to compare the relative accuracies of the two versions. Much of the high precision computational data was generated by us by using the density functional theory of electronic structure calculation. We found that almost universally the modified version agrees more closely with the observed data – although the degree of superiority is not uniform.

In order to compare the two versions we introduced a metric that can give a quantitative measure of the deviation from the best linear fit. It is in terms of this metric that we performed the comparison between the two choices. However, in a large number of cases the superiority of the modified version of the Birch's law was evident even visually from the two plots: one of P-wave speed V_P vs. density (ρ) and the other of $V_P\rho^{1/3}$ vs. ρ. These plots also make it evident why the modified form seems to work better much of the time: The plot of speed versus density has an upward curvature ($\frac{d^2V_P}{d\rho^2} < 0$) i.e. the deviation from linearity is in the form of a systematic curvature of a fixed sign. It is this curvature that is almost entirely cancelled upon multiplication of the dependent variable by the monotonically increasing extra factor of density raised to the power of one-third. But this also means that our metric of deviation from linear behaviour does not properly capture the damaging effect of this non-linear behaviour on

the process of extrapolation from low density data i.e. the metric may project a seriously undervalued representation of the mismatch between the extrapolated value at high densities and the actual data in case there is a systematic curvature. For example, in the V_P - ρ plots in the chapter 5, if we use only the three lowest density data points (excluding the one at $P = 0$) to perform the linear extrapolation we would have an overestimation by around three percent – which is significantly higher than what might be suggested by the values of the mean fractional deviation quantifying the goodness of linear fit.

We noted in the Introduction that a credible theory of the composition of the inner core would require both an accurate extrapolation formula and also sufficiently accurate data at the lower densities. The latter is presently difficult to attain in the laboratory set up. In this thesis we fulfilled our limited goals by generating high precision data with the help of density-functional-theory-based calculations. But all present DFT calculations have inherent uncontrolled approximations whose impact on the end results of the calculation are hard to assess (This is why we often need to validate the outcomes of these DFT-based calculations with the help of experimental results). Hence, in the long run, there is no alternative to experiments with adequate precision.

References

[1] H. Terasaki and R. A. Fischer (eds.) *Deep Earth: Physics and Chemistry of the Lower Mantle and Core* Wiley (Hoboken,2016).

[2] T. Sakamaki et al., Sci. Adv. **2**, e1500802 (2016).

[3] Y. Li, L. Vocadlo, and J. P. Brodholt, Earth and Planetary Sciences Letters **493**, 118 (2018).

[4] A. M. Dziewonski and D. L. Anderson, Phys. Earth Planet Inter. **25**, 297 (1981).

[5] R. Boehler, Nature **363**, 534 (1993).

[6] S. Anzellini, A. Dewaele, M. Mezouar, P. Loubeyre, and G. Morard, Science **340**, 464 (2013).

[7] D. Zhang et al, Earth Planet. Science Lett. **447**, 72 (2016).

[8] Y. Fei et. al., Geophys. Res. Lett., **43**, 6837 2016.

[9] F. Birch, J. Geophys. Res. **65**, 1083 (1960).

[10] F. Birch, J. Geophys. Res. **66**, 2199 (1961).

[11] F. Birch, Geophys. J. R. Astron. Soc. **4**, 295 (1961).

[12] D. H. Chung, Science **177**, 261 (1972).

[13] A. J. Campbell and D. L. Heinz, Science **257**, 66 (1992).

[14] G. Fiquet, J. Badro, F. Guyot, H. Requardt, and M. Krisch, Science **291**, 468 (2001).

[15] D. Antonangeli, F. Occelli, H. Requardt, J. Badro, G. Fiquet, and M. Krisch, Earth Planet. Sci. Lett. **225**, 243 (2004).

[16] D. Antonangeli, G. Morard, L. Paolasini, G. Garbarino, C. A. Murphy, E. Edmund, F. Decremps, G. Fiquet, A. Bosak, M. Mezouar and Y. Fei, Earth. Planet. Sci. Lett. **482**, 446 (2018).

[17] J. C. Crowhurst, A. F. Goncharov, and J. M. Zaug, J. Phys.: Condens. Matter **16**, S1137 (2004).

[18] J.-F. Lin, W. Sturhahn, J. Zhao, G. Shen, H.-K. Mao, and R. J. Hemley, Science **308**, 1892 (2005).

[19] D. Antonangeli, T. Komabayashi, F. Occelli, E. Borissenko, A. C. Walters, G. Fiquet, and Y. Fei, Earth Planet. Sci. Lett. **331**, 210 (2012).

[20] Z. Mao, J.-F. Lin, J. Liu, A. Alatas, L. Gao, J. Zhao, and H.-K. Mao, Proc. Natl. Acad. Sci. **109**, 10239 (2012).

[21] J. Liu et. al., J. Geophys. Res. Solid Earth, **121**, 610 (2016).

[22] E. Edmund et. al., J. Geophys. Res. Solid Earth **124**, https://doi.org/10.1029/2018JB016904.

[23] E. Ohtani, Y. Shibazaki, T. Sakai, K. Mibe, H. Fukui, S. Kamada, T. Sakamaki, Y. Seto, S. Tsutsui, and A. Q. R. Baron, Geophys. Res. Lett. **40** 5089 (2013).

[24] A. E. Gleason, W. L. Mao, and J. Y. Zhao, Geophys. Res. Lett. **40**, 2983 (2013).

[25] F. Decremps, D. Antonangeli, M. Gauthier, S. Ayrinhac, M. Morand, G. Le Marchand, F. Bergame, and J. Phillippe, Geophys. Res. Lett. **41**, 1459 (2014).

[26] D. Antonangeli and E. Ohtani, Prog. Earth Planet. Sci. **2**, 3 (2015).

[27] C. A. Murphy, J. M. Jackson, and W. Sturhahn, J. Geophys. Res. **118**, 1 (2013).

[28] G. Fiquet, J. Badro, E. Gregoryanz, Y. Fei, and F. Occelli, Phys. Earth Planet. Inter. **172**, 125 (2009).

[29] A. Kantor et al., Phys. Earth Planet. Inter. **164**, 83 (2007).

[30] L. Vočadlo, Earth Planet. Sci. Lett. **254**, 227 (2007).

[31] G. Lili et al., Geophys. Res. Lett. **35**, L17306 (2008).

[32] T. J. Shankland, J. Geophys. Res. **77**, 3750 (1972).

[33] O. L. Anderson, J. Geophys. Res. **78**, 4901 (1973).

[34] L. Vočadlo, D. P. Dobson, and I. G. Wood, Earth Planet. Sci. Lett. **288**, 534 (2009).

[35] X. Sha and R. E. Cohen, Geophys. Res. Lett. **37**, L10302 (2010).

[36] Y. Wang, J. J. Wang, H. Zhang, V. R. Manga, S. L. Shang, L-Q Chen and Z-K. Liu, J. Phys.: Condens. Matter **22**, 225404 (2010).

[37] J. K. Dewhurst, R. Ahuja, S. Li and B. Johansson, Phys. Rev. Lett. **88**, 075504 (2002).

[38] G. Stienle-Neumann, L. Stixrude, and R. E. Cohen, Phys. Rev. B **60**, 791 (1999).

[39] D. Antonangeli, M. Krisch, G. Fiquet, D. L. Farber, C. M. Aracne, J. Badro, F. Occelli, and H. Requardt, Phys. Rev. Lett. **93**, 215505 (2004).

[40] F. Birch, Phys. Rev. **71**, 809 (1947).

[41] D. C. Wallace, Phys. Rev. **162**, 776 (1967).

[42] L. D. Landau and E. M. Lifshitz, *Theory of Elasticity (2nd Edition)*, Pergamon Press (New York, 1984).

[43] R. Hill, J. Mech. Phys. Solids **13**, 213 (1965).

[44] Z. Hashin and S. Shtrikman, J. Mech. Phys. Solids **11**, 127 (1963).

[45] P. Gianozzi et al., J. Phys.: Condens. Matter **21**, 395502 (2009).

[46] R. Golesorkhtabar, P. Pavone, J. Spitaler, P. Puschnig, and C. Draxl, Comput. Phys. Commun. **184**, 1861 (2013).

[47] W. Kohn Rev. Mod. Phys **71**, 1253 (1999).

[48] P. Hohenberg and W. Kohn, Phys. Rev **136**, B864 (1964).

[49] W. Kohn and L. J. Sham, Phys. Rev **140**, A1133 (1965).

[50] M. C. Payne, M. P. Teter, D. c. Allan, T. A,. Arias and J. D. Joannopoulos, Rev. Mod. Phys **64**, 1045, (1992).

[51] S. Baroni, S. de Gironcoli, A. Dal Corso and P. Gianozzi, Rev. mod. Phys **73**, 515 (2001).

[52] D. Srivastava, U. V. Waghmare, and S. K. Sarkar, J. Chem. Phys. **141**, 044714 (2014).

[53] D. Srivastava, and S. K. Sarkar, Phys. Rev. B **85**, 024206 (2012).

[54] U. C. Roy and S. K. Sarkar, J. Appl. Phys. **121**, 225901 (2017).

[55] C. A. Murphy, J. M. Jackson, W. Sturhahn, and B. Chen, Geophysical Research Letters **38**, L24306 (2011).

[56] R. Lübbers, H. F. Grünsteudel, A. I. Chumakov and G. Wortmann, Science. **287**, 1250 (2008).

[57] S. Klotz and M. Braden, Phys. Rev. Lett. **85**, 3209 (2000).

[58] G. Shen et.al., Phys. Chem. Minerals **31**, 353 (2004).

[59] H. K. Mao et. al., Science **292**, (2001).

[60] H. Giefers et. al., Phys. Rev. Lett. **98** 245502 (2007).

[61] B. B. Karki, L. Stixrude, and R. M. Wentzcovich, Rev. Geophys. **39**, 507 (2001).

[62] T. Iitaka and T. Ebisuzaki, Phys. Rev. B **65**, 012103 (2001).

[63] H. Shimizu, H. Tashiro, T. Kume, and S. Sasaki, Phys. Rev. Lett. **86**, 4568 (2001).

[64] D. Antonangeli et al., Phys. Rev. B **72**, 134303 (2005).

[65] A. F Goncharov, J. Crowhurst and J. M. Zuag, Phys. Rev. Lett. **92**, 115502 (2004).

[66] A. V. Lugovsky, M. P. Belov, O. M. Krasilnikov, and Y. K. Vekilov, J. Appl. Phys. **116**, 103507 (2014).

[67] C. S. Zha, H. K. Mao, and R. J. Hemley, Phys. Rev. B **70**, 174107 (2004).

[68] L. Vočadlo, D. Alfè, M. J. Gillan, and G. D. Price, Earth Planet. Inter. **140**, 101 (2003).

[69] A. Polian and J. M. Besson, Phys. Rev. B **39**, 1332 (1989).

[70] T. Tsuchiya and M. Fujibuchi, Phys. Earth Planet. Inter. **174**, 212 (2009).

[71] A. Bosak, M. Krisch, I. Fischer, S. Huotari, and G. Monaco, Phys. Rev. B **75**, 064106 (2007).

[72] G. P. Francis and M. C. Payne, J. Phys.: Condens. Matter **2**, 4395 (1990).

[73] E. Menédez-Proupin and A. K. Singh, Phys. Rev. B **76**, 054117 (2007).

[74] H. K. Mao, J. Shu, R. J. Hemley, B. Li, and A. K. Singh, Nature **396**, 741 (1998) [Correction **399**, 80 (1999)].

[75] B. Martorell, J. Brodholt, I. G. Wood, and L. Vočadlo, Earth Planet. Sci. Lett. **365**, 143 (2013).

[76] H. Fang et al., Phys. B **405**, 732 (2010).

[77] L. Bo et al., Chin. Phys. B **19**, 026301 (2010).

[78] T. Tsuchiya and K. Kawamura, J. Chem. Phys. **117**, 5859 (2002).

[79] X. H. Deng, W. Lu, Y. M. Hu, and H. S. Gu, Phys. B **404**, 1218 (2009).

[80] C. Asker, L. Vitos, and I. A. Abrikosov, Phys. Rev. B **79**, 214112 (2009).

[81] C. Pantea et al., Phys. Rev. B **80**, 024112 (2009).

[82] C. Wang, J. Gu, X. Kuang, and X. Yang, Chin. Phys. B **24**, 086201 (2015).

[83] H. K. Mao, P. M. Bell, J. W. Shaner, and D. J. Steinberg, J. Appl. Phys. **49**, 3276 (1978).

[84] R. Jeanloz, B. K. Godwal, and C. Meade, Nature **349**, 687 (1991).

[85] H. Cynn, J. E. Klepeis, C. Yoo, and D. A. Young, Phys. Rev. Lett. **88**, 135701 (2002).

[86] A. Dewaele, M. Torrent, P. Loubeyre, and M. Mezouar, Phys. Rev. B **78**, 104102 (2008).

[87] S. Anzellini et al., J. Appl. Phys. **115**, 043511 (2014).

[88] L. Dubrovinsky et al., Nature **525**, 226 (2015).

[89] X. Huang et al., Sci. Rep. **6**, 19923 (2016).

[90] Y. Cerenius, J. Alloys Compd. **306**, 26 (2000).

[91] P. Söderlind, J. A. Moriarty, and J. M. Wills, Phys. Rev. B **53**, 14063 (1996).

[92] W. Mao et al., J. Geophys. Res. **113**, B09213 (2008).

[93] X. Sha and R. E. Cohen, Phys. Rev. B **81**, 094105 (2010).

[94] J. R. Neighbours, F. W. Bratten, and C. S. Smith, J. Appl. Phys. **23**, 389 (1952).

[95] M. Lv et al., Phys. B **407**, 778 (2012).

[96] L. Fast, J. M. Wills, B. Johansson, and O. Eriksson, Phys. Rev. B **51**, 17431 (1995).

[97] F. Peng, D. Chen, H. Fu, and X. Yang, Philos. Mag. Lett. **91**, 43 (2011).

[98] G. Pan et al., J. Mater. Res. **29**, 1334 (2014).

[99] J. A. Rayne, Phys. Rev. **118**, 1545 (1960).

[100] A. Dewaele, P. Loubeyre, and M. Mezouar, Phys. Rev. B **70**, 094112 (2004).

[101] B. Gabrowski, T. Hickel, and J. Neugebauer, Phys. Rev. B **76**, 024309 (2007).

[102] C. Bercegeay and S. Bernard, Phys. Rev. B **72**, 214101 (2005).

[103] J. Xie, S. P. Chen, H. V. Brand, and R. L. Rabie, J. Phys.: Condens. Matter **12**, 8953 (2000).

[104] V. Iota, J. P. Klepeis, C. Yoo, J. Lang, D. Haskel, and G. Srajer, Appl. Phys. Lett. **90**, 042505 (2007).

[105] G. Steinle-Neumann, L. Stixrude, and R. E. Cohen, Proc. Natl. Acad. Sci. **101**, 33 (2004).

[106] P. I. Dorogokupets, A. M. Dymshits, K. D. Litasov, and T. S. Sokolov, Scientific Reports, 7:41863 (2017). doi: 10.1038/srep41863.

[107] A. Dewaele, P. Loubeyre, F. Occelli, M. Mezouar, P. I. Dorogokupets and M. Torrent, Phys. Rev. Lett. **97**, 215504 (2006).

[108] J. H. Nguyen, M. C. Akin, R. Chau, D. E. Fratanduono, W. P. Ambrose, O. V. Fat'yanov, P. D. Asimow and N. C. Holmes, Phys. Rev. B **89**, 174109 (2014).

[109] X. Sha and R. E. Cohen, Phys. Rev. B **74**, 064103 (2006).

[110] D. Orlikowski, P. Söderlind and J. A. Moriarty, Phys. Rev. B **74**, 054109 (2006).

[111] Y. Zhao, A. C. Lawson, J. Zhang, B. I. Bennett and R. B. Von Dreele, Phys. Rev. B **62**, 8766 (2000).

[112] A. Eichler, K. -P. Bohnen, W. Reichardt and J. Hafner, Phys. Rev. B **57**, 324 (1997).

[113] F. H. Featherston and J. R. Neighbours, Phys. Rev **130**, 1324 (1963).

[114] W. Liu, Q. Liu, M. L. Whitaker, Y. Zhao and B. Li, J. Appl. Phys. **106**, 043506 (2009).

[115] Z-Yi. Zeng, C-E. Hu, L-Cang. Cai, X-Rong. Chen and F-Qian. Jing, J. Phys. Chem. **114**, 298 (2010).

[116] N. C. Holmes, J. A. Moriarty, G. R. Gathers and W. J. Nellis, J. Appl. Phys. **66**, 2962 (1989).

[117] J. M. Dickinson and P. E. Armstrong, J. Appl. Phys. **38**, 602 (1967).

[118] X. Zhang, Z. Liu, K. Jin, F. Xi, Y. Yu, T. Tan and C. Dai, J. Appl. Phys. **117**, 054302 (2015).

[119] Z-Li. Liu, J-Hui. Yang, L-Cang. Cai, F-Qian. Jing and D. Alfé, Phys. Rev. B**83**, 144113 (2011).

[120] J. H. Nguyen et al, Phys. Rev. B **89**, 174109 (2014).